A STUDY OF ENTRAINMENT IN TWO-PHASE UPWARD COCURRENT ANNULAR FLOW IN A VERTICAL TUBE

A Thesis
Submitted to the
College of Graduate Studies and Research
in Partial Fulfilment of the Requirements for the
Degree of Doctor of Philosophy

in the
Department of Mechanical Engineering
at the
University of Saskatchewan

By
Huawei Han

PERMISSION TO USE

In presenting this thesis in partial fulfillment of the requirements for a post-graduate degree from the University of Saskatchewan, I agree that the Libraries of this University may make it freely available for inspection. I further agree that permission for copying of this thesis in any manner, in whole or in part, for scholarly purposes may be granted by Dr. K. S. Gabriel or, in his absence, by the Head of the Department of Mechanical Engineering or the Dean of the College of Engineering of the University of Saskatchewan. It is understood that any copying or publication or use of this thesis or parts thereof for financial gain shall not be allowed without my written permission. It is also understood that due recognition shall be given to me and to the University of Saskatchewan in any use which may be made of any material in this thesis.

Requests for permission to copy or to make other use of the material in this thesis in whole or in part should be addressed to:

Huawei Han
huh498@mail.usask.ca

or

Head of the Department of Mechanical Engineering
University of Saskatchewan
57 Campus Drive
Saskatoon, Saskatchewan
S7N 5A9

ABSTRACT

The main purpose of this research is to investigate liquid entrainment mechanisms of annular flow by computational fluid dynamics (CFD) techniques. A numerical model is developed. The model is based on the physics of an upward annular flow. In the modeling, a transient renormalization group (RNG) k-ε model in conjunction with enhanced wall treatment method was employed. In order to reconstruct the two-phase interface, the geometric reconstruction scheme of volume of fluid (VOF) model was adopted. Fluent® 6.18 was used as the solution tool. Simulation results indicated that disturbance waves were generated first on the two-phase interface and their evolution eventually resulted in the liquid entrainment phenomena. The most significant accomplishment of this work is that details of the entrainment mechanisms are well described by the numerical simulation work. In addition, two new entrainment mechanisms are presented. One entrainment mechanism demonstrates that the evolution of individual waves causes the onset of liquid entrainment; the other mechanism shows that the coalescence of two adjacent waves (during the course of their evolution) plays an important role in the progression of liquid entrainment. The newly developed entrainment mechanisms are based on conservation laws.

In order to explore the flow physics of the targeted annular flow, the law of the wall, in conjunction with an analytical model based on a force balance, was applied to previously collected experimental data. Results indicated that the film flow had strong features of near-wall flow. In addition, based on prior experimental work and a newly developed physical wave model by researchers in the Microgravity Research Group,

University of Saskatchewan, a steady RNG k-ε model, in conjunction with the enhanced wall treatment method, was applied to the gas core. The simulation results showed turbulent flow features in the gas core and strong effects of the interfacial waves on the simulation results. The above information forms the physical foundation for the simulation work on the entrainment mechanism.

One significant contribution to the author's research group is the liquid entrainment fraction data. A new method was introduced to make the measurements. The method combined a chemically-based titration method with a newly-designed instrument, a separator, to effectively measure the entrainment fraction. Experiments were conducted at low system pressure (~ 1 atm) and relatively low gas and liquid superficial velocities (V_{sg} = 25.8 m/s to 45.5 m/s, and V_{sl} = 0.15 m/s to 0.30 m/s, respectively). The entrainment fraction was found to be under 7 %, with a maximum uncertainty of 0.26 % for all the experimental set points. Repeatability test results and comparisons with previous entrainment data indicated that the new technique can perform as well as other measurement techniques.

ACKNOWLEDGMENTS

I would like to thank my supervisor Prof. Kamiel Gabriel for his guidance, support, and allowing me to follow my aspirations. Thanks to my advisory committee members, Prof. Jim Bugg, Prof. David Sumner, and Prof. Todd Pugsley, for their invaluable support and advice.

I would also like to acknowledge the sound instruction I received in the graduate courses taught by Prof. Kamiel Gabriel, Prof. Jim Bugg, Prof. Robert Besant, Prof. David Sumner, Prof. David Torvi, and Prof. Donald Bergstrom.

Sincere thanks are extended to Mr. David Deutscher and Mr. Darren Braun of Thermo Lab, Mr. Bryan Wilson of Analytical Chemistry Lab, and Mr. Zhaolin Wang and Mr. Ryan MacGillivray of the former Microgravity Research Group for their help or assistance throughout this project.

Financial support for this research from the Department of Mechanical Engineering and the University of Saskatchewan is highly appreciated.

Special thanks to those who helped me in so many ways with love and words of encouragement, especially Dad, Mom, and my dear brother. They were a great source of my strength, wisdom, and hope.

DEDICATION

I dedicate this thesis to my lovely wife, Jin Sun, and my lovely son, Winston.

Thank you very much for your love and support throughout my Ph.D. studies.

TABLE OF CONTENTS

LIST OF TABLES

LIST OF FIGURES

NOMENCLATURE

English Symbols

A	tube cross-sectional area [m^2]
a_{nb}	discrete equation coefficients at other points
a_p	discrete equation coefficient at central point
B	systematic uncertainty
B_{Ei}	systematic uncertainty of Ei
B_i	systematic uncertainty of i
b	coefficient of uncertainty analysis
C	coefficient of uncertainty analysis
$C_{1\varepsilon}$	constants of RNG turbulence model
$C_{2\varepsilon}$	constants of RNG turbulence model
$C_{3\varepsilon}$	constants of RNG turbulence model
C_{CD}	concentration of titrated $CaCl_2$ in the collected droplets sample solution [M]
C_{CDS}	total concentration of calcium/magnesium in the collected droplets sample solution [M]
C_{CL}	concentration of titrated $CaCl_2$ in the collected liquid film sample solution [M]
C_{CLS}	total concentration of calcium/magnesium in the collected liquid film sample solution [M]
C_{CW}	concentration of original calcium/magnesium in water [M]
C_v	constants of RNG turbulence model
D	tube diameter [m]
D_A	diameter of liquid film collecting tube [m]
D_B	diameter of gas core collecting tube [m]
D_D	diameter of inner cylinder of separator [m]
E	entrainment fraction [%]
E_{CaCl2}	mass fraction of $CaCl_2$ in droplets [%]
E_D	entrainment fraction due to flow entrainment mechanism [%]
E_L	liquid potion in the gas core [%]
E_S	entrainment fraction due to separator [%]
F_g	gravitational force [N]
f	volume fraction
f_A	friction factor of liquid collecting tube A
f_B	friction factor of gas collecting tube B
f_i	volume fraction of fluid i
f_q	volume fraction of fluid q
G_b	generation term of k due to buoyancy [kg/ms^3]
G_g	mass flux of gas phase [kg/m^2s]
G_g	mass flux of liquid phase [kg/m^2s]
G_k	production term of turbulent kinetic energy [kg/ms^3]

g	acceleration of gravity [m/s^2]
H	average film thickness [m]
H^+	dimensionless average film thickness
I	turbulence intensity of two phases [m^2/s^2]
I_{gas}	turbulence intensity of gas phases [m^2/s^2]
I_{liquid}	turbulence intensity of liquid phases [m^2/s^2]
k	kinetic energy of turbulent fluctuations per unit mass [m^2/s^2]
L_A	length of liquid collecting tube A [m]
L_B	length of liquid collecting tube B [m]
m	coefficient of uncertainty analysis
$\dot{m}_g$	gas mass flow rate of the annular flow [kg/s]
$\dot{m}_L$	liquid film mass flow rate of the annular flow [kg/s]
$\dot{m}_l$	liquid mass flow rate of the annular flow [kg/s]
$\dot{m}_{TD}$	droplet mass flow rate of the annular flow [kg/s]
$\dot{m}_w$	total liquid mass flow rate of the annular flow [kg/s]
m_1	mass of droplets solution with container 1 [kg]
m_{1s}	mass of container 1 [kg]
m_2	mass of film solution with container 2 [kg]
m_{2s}	mass of container 2 [kg]
m_{CD}	mass of $CaCl_2$ in the droplets sample solution [kg]
m_{CL}	mass of $CaCl_2$ in the liquid film sample solution [kg]
m_D	mass of entrained liquid droplets [kg]
m_L	mass of liquid film sample solution of the annular flow [kg]
m_S	mass of part of liquid film physically shared into the gas core by separator [kg]
m_{TD}	mass of droplets sample solution of the annular flow [kg]
N_1	EDTA titrant volume titrated into droplets sample solution [L]
N_2	EDTA titrant volume titrated into film sample solution [L]
N_w	EDTA titrant volume titrated into water sample solution [L]
P	pressure [Pa]
P_A	pressure at the end of liquid film collecting tube [Pa]
P_B	pressure at the end of gas core collecting tube [Pa]
P_C	pressure on the side of liquid film at blade tip of separator [Pa]
P_D	pressure on the side of gas core at blade tip of separator [Pa]
P_i	precision uncertainty of i
Pr_t	turbulent Prandtl number
Q	gas mass flow rate [kg/s]
Q_1	gas mass flow rate at the end of liquid film collecting tube [kg/s]
Q_2	gas mass flow rate at the end of gas core collecting tube [kg/s]
R	normalized residual
R	tube radius [m]
R_ε	additional term of RNG model [kg/ms^4]
$\vec{r}_1$	position vector of “1” [m]
$\vec{r}_2$	position vector of “2” [m]

Δr_{max}	maximum mesh size in radial direction [m]
Δr_{min}	minimum mesh size in radial direction [m]
See	precision uncertainty
S	modulus of strain rate tensor
S_k	user defined source term for k equation [kg/ms^3]
S_ε	user defined source term for ε equation [kg/ms^4]
T	temperature [K]
t	function of freedom of uncertainty analysis
t	time [s]
Δt	sample collecting time [s]
Δt	time step [s]
U_i	mean velocity in tensor notation [m/s]
U_i	uncertainty
U_j	mean velocity in tensor notation [m/s]
u	velocity [m/s]
u^*	friction velocity [m/s]
u^+	dimensionless velocity
u_i`	fluctuating velocity in tensor notation [m/s]
u_j	fluctuating velocity in tensor notation [m/s]
V	velocity [m/s]
$\vec{V}$	velocity in vector notation [m/s]
V_g	actual velocity of gas phase [m/s]
V_g	actual velocity of gas phase [m/s]
V_l	actual velocity of liquid phase [m/s]
$V_{max,\ fluid}$	maximum fluid velocity [m/s]
V_{sg}	superficial gas velocity, velocity of gas flowing alone in the tube [m/s]
V_{sl}	superficial liquid velocity, velocity of liquid flowing alone in the tube [m/s]
V_{TD}	entrained liquid velocity [m/s]
W_e	Weber number
W_{eg}	Weber number of gas phase
X	coordinate [m]
X_1	X coordinate at position “1” [m]
X_2	X coordinate at position “2” [m]
X_3	X coordinate at position “3” [m]
X_4	X coordinate at position “4” [m]
x_i	position vector in tensor notation [m]
x_j	position vector in tensor notation [m]
Δx	grid length [m]
$\Delta x_{min,\ cell}$	least grid length of the cell [m]
Y_M	dilatation dissipation term [kg/ms^3]
y	distance from wall [m]
y+	dimensionless distance from wall
Z	coordinate [m]

Greek Symbols

α	void fraction
α_k	inverse effective Prandtl number for k
α_o	constant
α_ε	inverse effective Prandtl number for ε
β	constants of RNG model
δ_{ij}	Kronecker delta or identity tensor
ε	dissipation rate per unit mass [m^2/s^3]
ϕ	tube diameter [m]
ϕ	variable
ϕ_1	variable value of control volume 1
ϕ_2	variable value of control volume 2
ϕ_f	variable value on face f
$\phi_{f,up}$	variable upwind value on face f
η_o	constants of RNG model
μ	dynamic viscosity [Ns/m^2]
μ_{eff}	effective dynamic viscosity [Ns/m^2]
μ_g	gas dynamic viscosity [Ns/m^2]
μ_h	homogeneous mixture dynamic viscosity [Ns/m^2]
μ_l	liquid dynamic viscosity [Ns/m^2]
μ_t	turbulent dynamic viscosity [Ns/m^2]
ν	kinematic viscosity [m^2/s]
$\nu`$	turbulent kinematic viscosity [m^2/s]
ρ	density [kg/m^3]
ρ_g	gas density [kg/m^3]
ρ_h	homogeneous mixture density [kg/m^3]
ρ_l	liquid density [kg/m^3]
σ	air-water surface tension [N/m]
τ	interfacial shear stress [kg/s^2m]
τ_w	wall shear stress [kg/s^2 m]

LIST OF ABBREVIATIONS

2 - D	Two-Dimensional
B.C.	Boundary Condition
C.V.S	Control Volumes
CFD	Computational Fluid Dynamics
CPU	Central Processing Unit
CSF	Continuum Surface Force
EDTA	Ethylenediaminetetraacetic
ESA	European Space Agency
ID	Inner Diameter
LDCP	Liquid Droplets Cloudy Phenomenon
N – S	Navier-Stokes
PISO	Pressure-Implicit with Splitting of Operaters
PLIC	Piecewise Linear Interface Calculation
QUICK	Quadratic Upstream Interpolation for Convective Kinetics
RANS	Reynolds Averaged Navier-Stokes
RNG	ReNormalization Group
SIMPLE	Semi-Implicit Method for Pressure-Linked Equations
SIMPLEC	SIMPLE-Consistent
SLIC	Simple Line Interface Calculation
VOF	Volume of Fluid

CHAPTER 1

INTRODUCTION

1.1 Motivation

Gas-liquid annular flow is an important two-phase flow regime. It frequently occurs in thermal management and thermal control systems in terrestrial and non-terrestrial energy transport systems such as nuclear reactors, power plants, boilers, heat exchangers, and space stations. In annular flow, excessive liquid entrainment could lead to catastrophic events caused by “dry out” conditions in which the liquid film is completely removed from contact with the channel’s walls. It is very important to be able to predict such conditions to avoid its actual occurrence, particularly in situations where the effects could be quite disastrous such as the breakdown of the Chernobyl nuclear reactor. However, the onset of the entrainment process and its progress through the formation of what is known as “disturbance waves” is poorly understood. This study is aimed at an improved understanding of this process using a combination of experimental and numerical investigations.

1.2 Background

1.2.1 Annular Flow

In vertical upward gas-liquid two-phase flow, with increasing the gas flow rate, the flow usually changes from bubbly flow to slug flow (or plug flow) to churn flow and finally to annular flow. Annular two-phase flow is the focus of this research. It is characterized by a gas core flowing in the centre of the tube, a liquid film flowing on the inner tube wall, and a gas-liquid interface covered with waves. The gas core also carries entrained liquid droplets. The droplets are believed to be transported into the gas core as crests of the waves are sheared off by the gas stream. Figure 1.1 is a schematic of a typical two-phase annular flow regime.

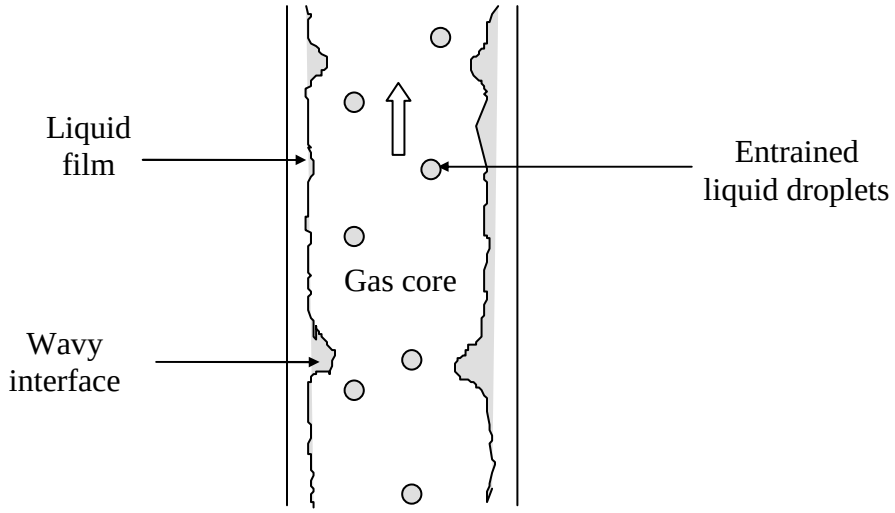

Figure 1.1 Schematic of two-phase annular flow.

1.2.2 Interfacial Waves

A significant feature of annular flow is the presence of waves with various scales on the two-phase interface. While the two-phase flow literature contains many types and names for interfacial waves, there is agreement that two types are typically

present. They are called “ripple waves” and “disturbance waves”. Ripple waves have small amplitudes compared with the liquid film thickness. Their wavelengths are usually measured in several millimeters (Hewitt and Govan, 1990). Their life time is short and they usually do not occupy the whole tube circumference. Disturbance waves are sometimes called “roll waves” (Hanratty and Hershman, 1961). They have a longer lifespan, and their amplitudes are usually several times the liquid film thickness. Their wavelengths are several tube diameters for flow in a small-diameter tube (Asali and Hanratty, 1993). In addition, for annular flow in a small-diameter tube (Tube ID < 58 mm, Pols et al., 1998), the liquid film is uniformly distributed around the tube circumference (Asali et al., 1985), and disturbance waves appear circumferentially coherent (Hall-Taylor et al., 1963; Hewitt and Lovegrove, 1969; Asali and Hanratty, 1993), two-dimensional (Zhu, 2004), and circumferentially symmetrical (Hewitt and Hall-Taylor, 1970; Ohba and Nagae, 1993). The observations by Martin (1983) indicated that waves were highly regular in tubes with an inside diameter of 10 mm, which corresponds to the present study. These characteristics of disturbance waves are obviously important in modeling of waves and the flow phenomena associated with them. They indicate that a two-dimensional model is sufficient for CFD modeling of annular flow in a small-diameter tube. A disturbance wave has a steep front and a long region of relatively quiet fluid between crests (Wallis, 1969a). Several investigations on the disturbance wave configurations were performed in the past. Sekoguchi et al. (1985) presented images of disturbance waves, which were directly based on their measurements in vertical annular flow in a 25.8-mm tube using needle conductance probes. Figure 1.2 gives the wave profile. Zhu’s (2004) physical wave model provides

similar wave profiles based on the measurement data of MacGillivray (2004) in vertical annular flow in a 9.525-mm tube using film thickness probes. Figure 1.3 shows the configuration of a disturbance wave as developed by Zhu (2004).

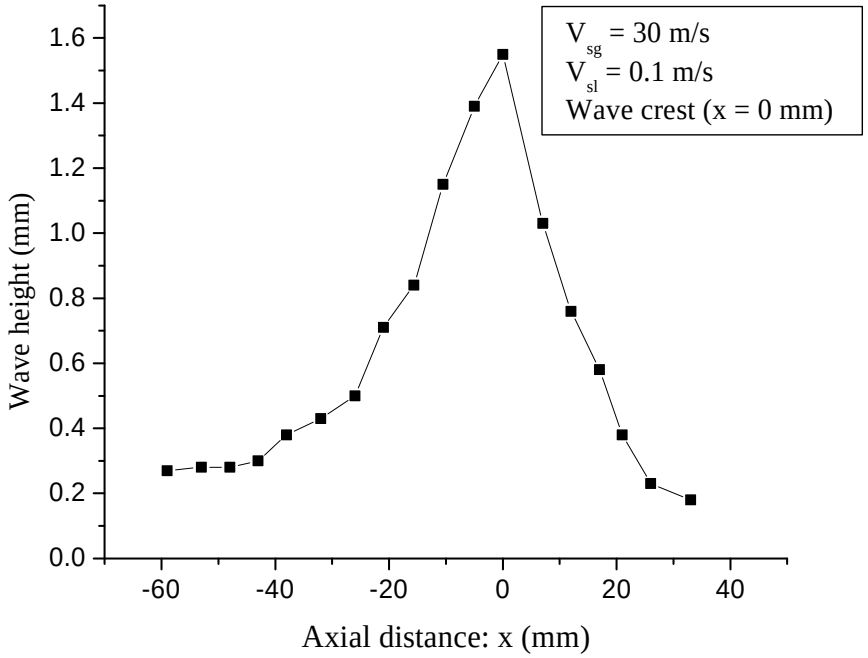

Figure 1.2 Disturbance wave model proposed by Sekoguchi et al. (1985).

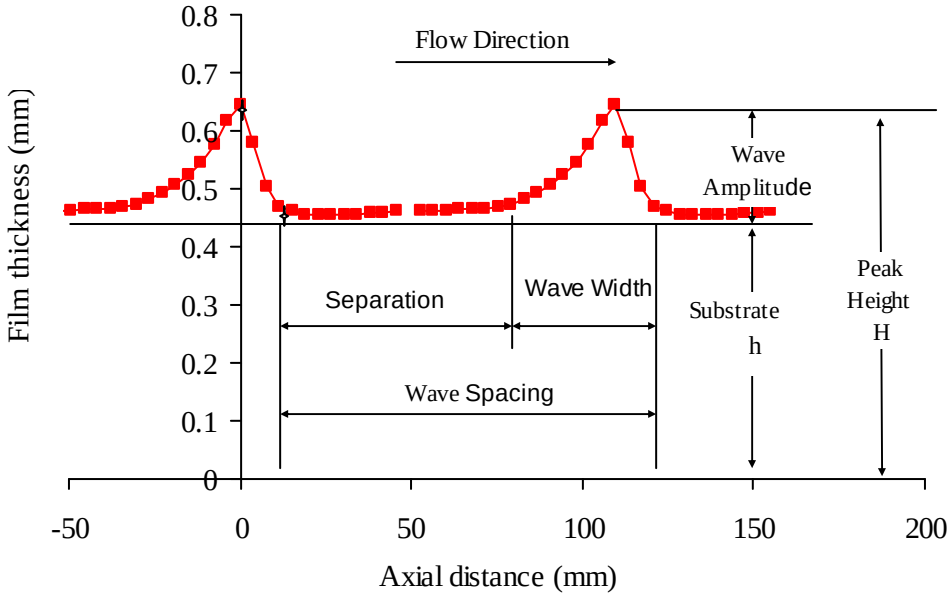

Figure 1.3 Disturbance wave model developed by Zhu (2004).

At very low liquid flow rates the ripple waves dominate the two-phase interface. The surface looks smooth and appears to be laminar between waves. Above a critical liquid flow rate, disturbance waves appear in the flow (Andreussi et al., 1985; Schadel, 1988) and exert strong influence on the flow due to their significant dimensions and dynamic properties. Unlike disturbance waves, ripple waves exist over the full range of annular flow. For all the annular flow experimental data that were analyzed during the course of this research, disturbance waves dominate the two-phase interfaces. Due to their minor role, ripple waves are usually not considered.

Waves play crucial roles in the transport processes in annular flow such as mass transfer, momentum transfer, and heat transfer between the phases. However, this is not the focus of the present study. Waves are mentioned here because they significantly contribute to the liquid entrainment phenomena and mechanisms in annular flows.

1.2.3 Liquid Entrainment Phenomena and Mechanisms

In annular flow, part of the liquid flows in the form of a film on the tube wall while the other part flows as entrained liquid droplets in the gas core. The process is dynamic with continuous exchange of mass, momentum, and energy between the liquid film and the droplets in the gas core. The liquid in the film continuously enters the gas core in the form of droplets in a process called liquid entrainment, and the droplets in the gas core continuously deposit on the film in a process called droplet deposition. When the two processes reach a balance, a fully developed annular flow is obtained and the mass flow rate of liquid droplets remains constant in the gas core. The ratio of the mass flow rate of the liquid phase, in the form of droplets in the gas core, to the total mass flow rate of the liquid phase is defined as liquid entrainment fraction (also called

liquid entrained fraction). It is noted that in the literature the term liquid entrainment, sometimes called atomization (Hanratty and coworkers: Dallman et al., 1984; Dykhno and Hanratty, 1996; Pan and Hanratty, 2002), also has the same meaning as entrainment fraction. In this study, liquid entrainment only refers to the process where part of the liquid phase is entrained into the gas core as a result of incoming gas flow "shearing-off" the wave crests and carrying them in the form of droplets.

Generally, there are three well-known mechanisms by which the liquid film is entrained into the gas core in vertical upward annular flow: these are (a) wave entrainment, (b) entrainment by bubble burst, and (c) entrainment by Droplet impingement. It is widely accepted that after disturbance waves are generated in the flow, wave entrainment is the most dominant liquid entrainment mechanism, while the other two types of mechanisms are generally neglected. This in fact is supported by the findings of Van Rossum (1959), Hall-Taylor et al. (1963), Woodmansee and Hanratty (1969), and Schadel and Hanratty (1989). Their research work showed that liquid entrainment fraction cannot be measured until after disturbance waves appear in the annular flow. Conventionally speaking, when the liquid entrainment mechanism is mentioned in annular flow, it usually refers to the wave entrainment mechanism. This thesis follows the same convention in the following chapters. This section gives a general description of all three entrainment mechanisms. The research activities on the wave-induced entrainment mechanism will be addressed separately in the next section.

It has long been known that some gas bubbles are entrained or produced in the liquid film and their rising and bursting in the liquid film could lead to liquid droplets being entrained into the gas core. Garner et al. (1954), Newitt et al. (1954), and Hewitt

et al. (1990) all conducted studies on this mechanism. Figure 1.4 schematically shows this entrainment mechanism. In the gas core of annular flow, some liquid droplets will re-deposit back onto the liquid film. Their direct impaction on the film may cause some other small size liquid droplets to be entrained into the gas core. Figure 1.5 schematically demonstrates this process.

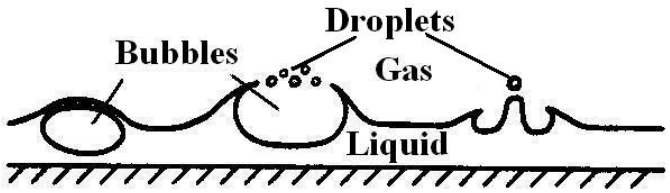

Figure 1.4 Bubble burst entrainment mechanism (Ishii and Grolmes, 1975).

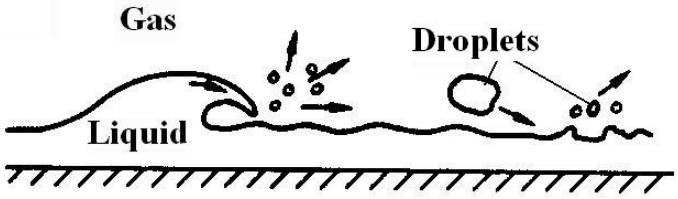

Figure 1.5 Droplet impingement entrainment mechanism (Ishii and Grolmes, 1975).

As mentioned earlier, when disturbance waves appear at the liquid-gas interface, the wave entrainment mechanism is the dominant one that shears-off droplets into the gas core. The relation between the disturbance waves and droplet entrainment has been clearly established since the 1960s by photographic and visual studies (Cooper et al., 1964; Jacowitz and Brodkey, 1964; Arnold and Hewitt, 1967; Woodmansee and Hanratty, 1969). However, the exact mechanism for how the liquid droplets are generated out of a disturbance wave is still controversial. The fundamental recognition

is that liquid entrainment is due to the disturbance wave crest being sheared-off into the gas core. Several wave entrainment mechanisms were proposed to interpret this shearing-off process based on various studies, which include: wave undercut, wave rolling, ripple wave shearing-off, and wave coalescence. So far, there is no solid and direct evidence to favor any particular one.

Hewitt and Hall-Taylor (1970) and Whalley (1987a) were the first to introduce the wave undercut entrainment mechanism as shown in Figure 1.6. In this mechanism, part of the liquid in the disturbance wave peak region is “stretched” and sheared off by the incoming high speed gas flow in the core. The sheared-off liquid eventually breaks up into droplets of various sizes. The wave undercut entrainment mechanism was enlightened from the droplet breakup mechanism. The fundamental work of this entrainment mechanism can be traced back to Lane (1951).

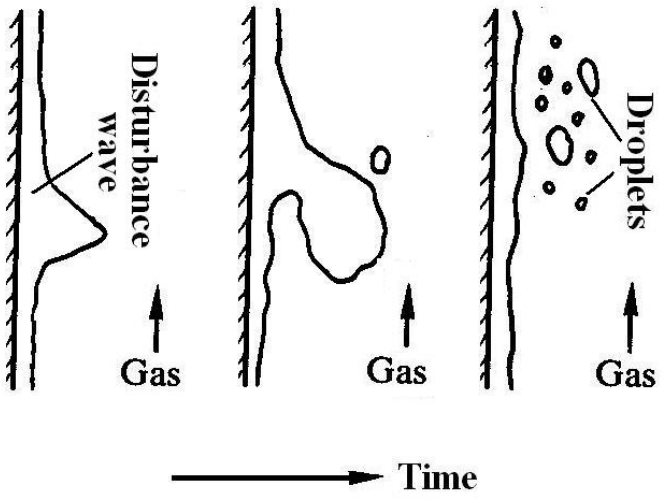

Figure 1.6 Wave undercut entrainment mechanism (Whalley, 1987a).

The wave rolling entrainment mechanism has been described in a way similar to the breakup of beach waves in high winds, and was initially introduced by Hewitt and Hall-Taylor (1970). Under the action of high speed gas, the tips of disturbance waves would be steepened, roll forward, and subsequently break up into liquid droplets. The process is schematically shown in Figure 1.7. This mechanism was developed from the breakup mechanism of liquid jets and sheets. However, just as the authors questioned, it is doubtful if the conclusions on the work of liquid jets and sheets could be directly applied to disturbance waves in annular flow since the latter case is far more complicated than the former.

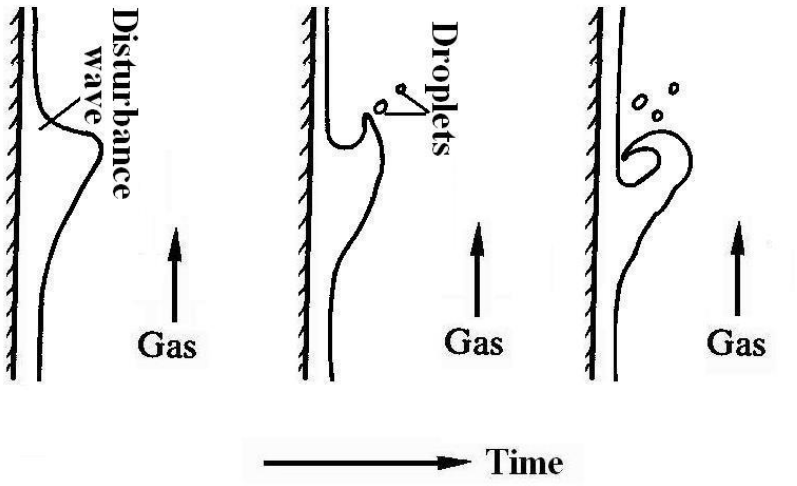

Figure 1.7 Wave rolling entrainment mechanism (Hewitt and Hall-Taylor, 1970).

Hall-Taylor et al. (1963) made the observation from their experiments that when two disturbance waves collided and joined together, a burst of liquid entrainment was induced. This, in effect, describes the wave coalescence entrainment mechanism as illustrated in Figure 1.8 below.

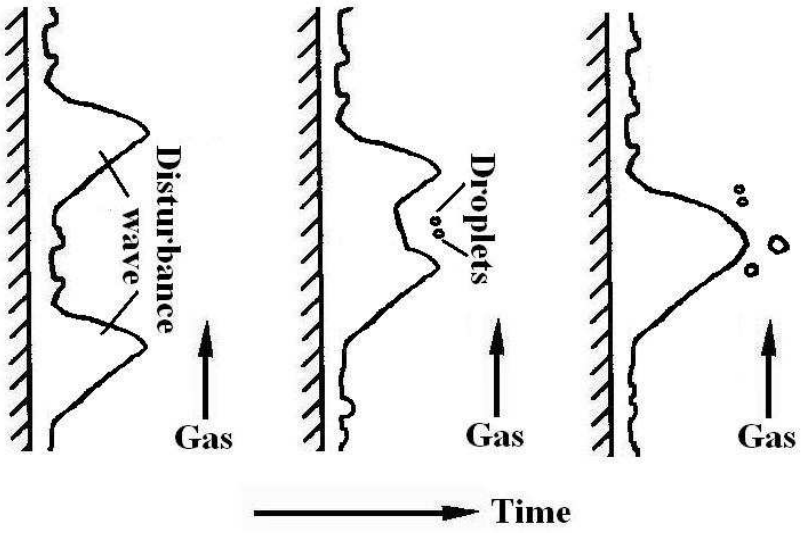

Figure 1.8 Wave coalescence entrainment mechanism.

Woodmansee and Hanratty (1969), based on high-speed photographic studies, proposed that ripples riding on top of the disturbance waves are removed by the incoming gas stream causing entrainment. The process is shown schematically in Figure 1.9. It is noted that the importance of disturbance waves in this type of mechanism is to provide a platform from which liquid entrainment is triggered. This is different from all the previously discussed types of wave entrainment mechanisms in which the liquid carried by the disturbance waves provide the entrained liquid droplets.

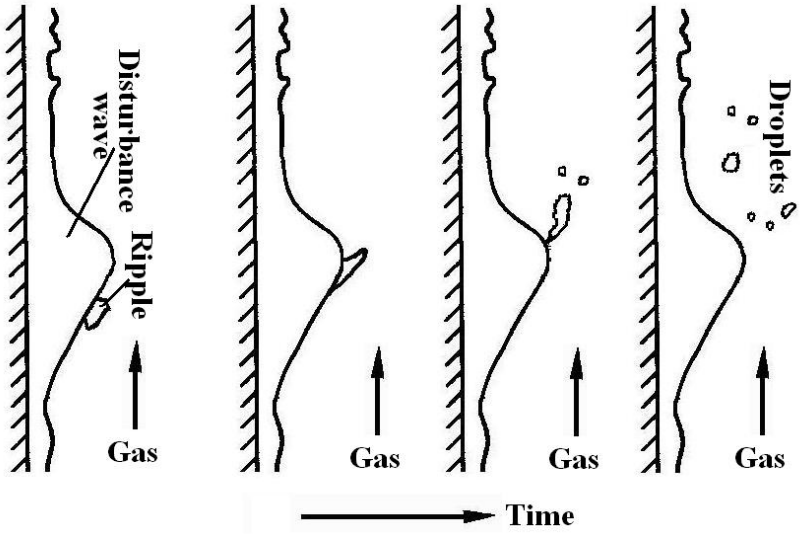

Figure 1.9 Ripple shearing-off entrainment mechanism.

1.3 Scope and Outline

The primary objective of this research is to explore the entrainment mechanisms using well-established CFD techniques. This is assisted by flow physics studies and entrainment fraction measurements. The flow physics studies form the foundation for the modeling of the entrainment mechanisms. In addition, previously collected flow images are used to further explain the entrainment phenomena. The entrainment fraction measurements are used for comparison with prior entrainment studies and to provide a more quantitative benchmark for such comparisons. The scope of this research work does not include the development of new numerical codes but rather to use existing, suitable CFD software packages (Fluent® 6.18 in this case) to perform extensive simulations.

Chapter 2 includes a literature review of entrainment fraction measurements and studies of the wave entrainment mechanisms. The literature review summarizes prior experimental research work in this area. The methods employed for numerical simulations are also presented. The RNG k-ε turbulence model, in conjunction with the enhanced wall treatment method, and geometric reconstruction VOF scheme are introduced in some detail. In Chapter 3, the law of the wall is combined with an analytical model based on a force balance in annular flow to analyze the flow features of the liquid film. Also, flow images that were previously collected by other graduate students are presented and discussed. Chapter 4 presents a two-dimensional and steady-state numerical model in the gas core (Simulation I). The modeling adopts the RNG k-ε turbulence model and the enhanced wall treatment method. Thus, the flow features of the gas core are disclosed in detail. Furthermore, the force mechanism that triggers the

liquid entrainment is also introduced based on the simulation results. Chapter 5 introduces the experimental set-up and the data from a new experimental method for the measurement of the entrainment fraction. The method is characterized by a newly-designed separator and a chemically-based titration method. Chapter 6 establishes a two-dimensional and transient numerical model to further explore the entrainment mechanism (Simulation II). As in Simulation I, this method adopts the RNG k-ε turbulence model and the enhanced wall treatment method. In addition, a geometric reconstruction VOF scheme is adopted. The mesh-independence calculations and sensitivity calculations are performed and the simulation process is introduced. Chapter 7 presents the liquid entrainment mechanisms based on results from these simulations. Their features are discussed and compared with those found in the open literature. Finally, Chapter 8 summarizes the findings from this work and presents recommendations for future work.

CHAPTER 2

LITERATURE REVIEW

2.1 Experimental Studies

2.1.1 Entrainment Fraction Measurement

It is fair to say that most of the experimental studies have focused on the measurement of the liquid film attached to the wall or the entrained liquid droplets dispersed in the gas core in order to obtain an entrainment fraction. In general, the most common methods reported in the literature for entrainment fraction measurements can be categorized into two main groups: (a) the sampling probe method, and (b) the liquid film removal method. The former method is used to sample the entrained liquid droplets in the gas core while the latter is used to collect the liquid film flowing on the inner tube wall. In addition, a tracer measurement method was also reported. This method will be introduced later.

The sampling probe method, also called the isokinetic probe method, involves droplet flux measurements at different positions across the diameter of the tube. The average is obtained from the integral of the droplet flux over the tube cross section. As shown in Figure 2.1, the sampling probe intrudes into the gas core and the gas velocity in the probe is controlled so as to match that of the gas core. As a result, droplets in the gas stream impacting the probe's mouth will flow unobstructed into the probe. This

controlled condition of the flow is called the isokinetic condition, which is the reason why the sampling probe method is also called “isokinetic probe method”. The liquid droplets flowing into the probe are collected downstream and measured. In this way, the droplets flux and the gas velocity at the location of the probe mouth are known, and the total liquid entrainment can be determined from the integration of the droplets flux over the cross-sectional area of the tube. Wallis (1962) and Gill et al. (1963 and 1964), among others, have developed this method and contributed much to its progress from an early, unsophisticated technique. Later, many investigators adopted this method in their research; e.g., Andreussi and Zanelli (1978), Asali (1984), Paras and Karabelas (1991), and Barbosa, Jr. et al. (2002). One of the limitations of this method is its inability to take measurements near the interface due to the sampling of part of the liquid in the waves. In small-diameter tubes, this method severely disturbs the flow and as such it is not feasible.

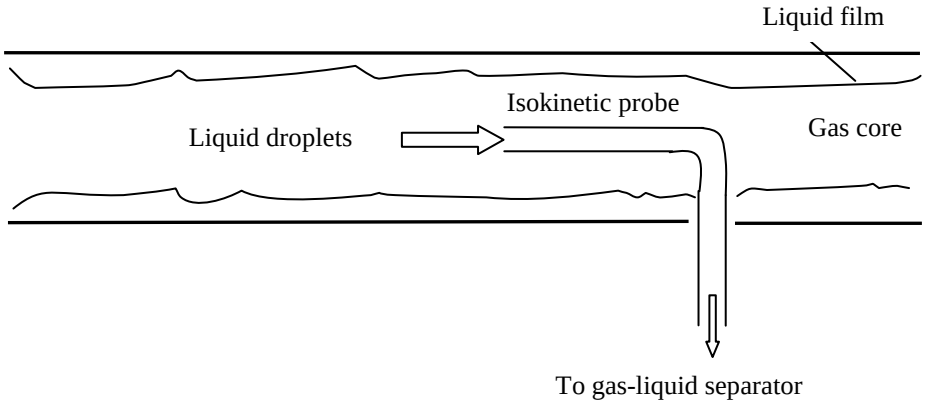

Figure 2.1 Droplet sampling technique by an isokinetic probe.

The liquid film removal (also known as “liquid film withdrawal” or “liquid film extraction”) method involves techniques for liquid film extraction through a porous wall

or a small opening on the tube wall, shown in Figure 2.2. Its early users included Cousins and Hewitt (1968), Keeys et al. (1970), Webb (1970), and Whalley et al. (1973). Recent users included Fore and Dukler (1995), Lopez de Bertodano et al. (1997), and Assad et al. (1998). The advantage of this method is that the liquid entrainment fraction can be directly measured by collecting the liquid droplets after the gas-droplets separator. As well, the entrainment fraction can be also calculated from the difference between the total liquid flow rate and the liquid film flow rate which is measured by collecting the liquid film through the porous wall. The disadvantage of this technique is that the film flow rate will be very close to the total flow rate if the liquid entrainment is low enough, thus it is difficult to calculate the entrainment fraction from the difference of total liquid and film flow rates because of the practical measurement error. Furthermore, it is also difficult to completely separate the droplets from the gas stream if the entrainment is low. The application of this method relies heavily on unaided eye observations to judge the point of complete removal of the liquid film. This

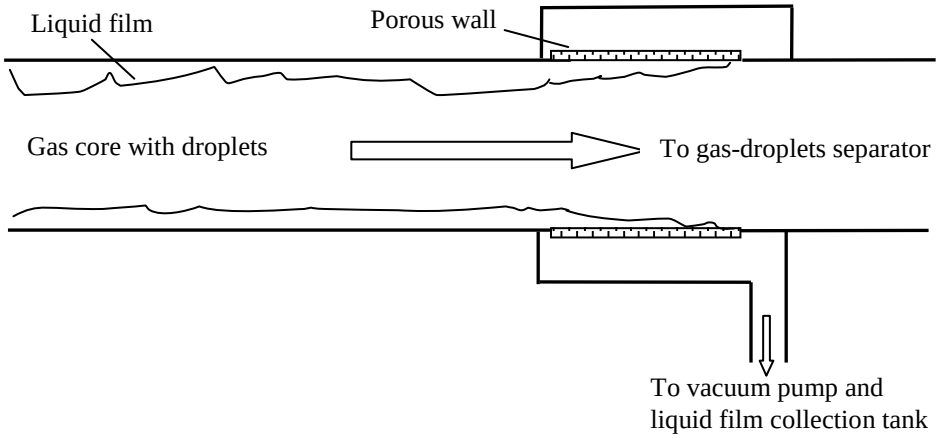

Figure 2.2 Film removal technique by porous wall.

is very subjective and often results in large errors in the measurements. Another contributor to the uncertainty of this method, which is commonly neglected by authors, arises during the removal of the liquid film (especially near the end points). The equilibrium of entrainment and deposition of droplets will be altered as deposition will be quickened. The removal of part of the gas along with the liquid through the porous wall also causes an additional uncertainty. Moreover, if the visibility of flow is poor due to, for example, high turbulence near the wall, this method produces significant errors.

The tracer measurement method, in its simplest form, is to inject a tracer into the liquid film and measure its concentration at different locations downstream. The tracer could be a dye or some other solution. Quandt (1965) first presented this method. Schadel et al. (1990) later adopted this method to determine the rates of atomization and deposition and the entrainment fraction for vertical annular flow in various diameter tubes. It is rarely reported in the literature at the present time due to the cumbersome procedure associated with it and the lack of accuracy in using it.

Among the three methods discussed above, the former two are widely used. It is usually believed that the film extraction technique produces more accurate results. With the added complexity of flow in small-diameter tubes, this method is perhaps one of the few techniques available to obtain acceptable results. Table 2.1 summarizes the entrainment experiments in air-water annular flow in small-diameter tubes similar to the one used in the present study. All the measurements in those experiments adopted a liquid film removal method.

Table 2.1 Summary of entrainment experiments in air-water annular flow in small-diameter tubes

Investigators	Year	Fluids	Tube diameter (mm)	Method
Assad et al.	1998	Air-water	9.5	Liquid film removal method
Jepson et al.	1989		10.3	
Willetts	1987		10.0	
Cousins and Hewitt	1968		9.5	
Hinkle	1967		12.7	
Cousins et al.	1965		9.5	

2.1.2 Study of the Wave Entrainment Mechanism

As mentioned earlier, four types of wave entrainment mechanisms have been proposed so far in the open literature: wave undercut, wave rolling, ripple wave shearing-off, and wave coalescence. This section gives some details of experimental studies concerning these mechanisms.

The wave undercut entrainment mechanism in annular flow was suggested based on the analogy of the mechanisms of droplet breakup in the gas stream from which the entrainment mechanism details could be deduced. Lane (1951), using an electronic photographic technique, observed the shatter of droplets in a fast air blast. Lane described the whole breakup process as “it (the droplet) is deformed in the opposite direction (of the air blast) and presents a convex surface to the flow of air. The edges of the saucer shape are drawn out into a thin sheet and then into fine filaments which in turn break up into droplets”. Azzopardi and Hutchinson (1983) also observed a similar process using high speed cine films. In addition, their cine films recorded another observed droplet-breakup process in which the droplets were “blown inside out” and

thus smaller droplets were generated. Azzopardi (1983) named the former as the "ligament breakup entrainment mechanism", and he named the latter the "bag breakup entrainment mechanism". Krzeczkowski (1980), by means of a photographic camera and a spark flash, identified four types of droplet breakup mechanisms in his investigations on droplet deformation and disintegration in a gas stream in which the above mentioned two mechanisms were included.

Hall-Taylor et al. (1963) investigated the motion and frequency of the disturbance waves in a vertical annular two-phase flow (Tube ID = 31.25 mm). Using high-speed cine films, they observed that the collision and combination of two disturbance waves lead to liquid droplet entrainment. However, no photographs were presented to show how this process happened. In the study, they defined three types of wave collisions. Based on that mechanism, Wilkes et al. (1983) derived a wave coalescence model by which the wave coalescence process was modeled and the entrainment fraction due to the wave coalescence was predicted. Comparison of the modeling results with the experimental data indicated that the liquid entrainment fraction due to the wave coalescence could be a significant portion of the total liquid entrainment. The Monte-Carlo technique was used in the modeling.

The ripple wave shearing-off entrainment mechanism was proposed by Woodmansee and Hanratty (1969). They investigated the liquid entrainment mechanism of a stratified flow in a horizontal rectangular channel. Their high speed photographs revealed that liquid entrainment occurs by the removal of small wavelets which exist on top of the disturbance waves in the liquid film. The authors further pointed out that it is

the Kelvin-Helmholtz instability that caused the removal of ripples from the surface of the disturbance wave.

From the above survey, it is clear that there exist different theories and explanations for the wave entrainment mechanisms of annular flow, but a full understanding of such mechanisms is at best incomplete and uncertain at present. In addition, there are no sufficient details about any of them, or direct and consistent proof to favor any mechanism over the others. This is partially due to the limitations of current instrumentation methods, but also due to the extreme complexity of the liquid entrainment process itself. With such limitations and complexity of the experimental procedure, and with the significant progress in CFD techniques, several studies have attempted using numerical modeling to get clues into the process.

So far, there exist a few models to study the wave entrainment mechanisms. In addition to the work by Wilkes et al. (1983) on the wave coalescence mechanism, Holowach et al. (2002) developed a model to study wave entrainment. The foundation of their model was the wave crest shearing-off mechanism. The model was based on a force balance and interfacial instability. The forces considered in the model were wave crest drag force, gravitational force, and surface tension force. The model was used to predict the liquid entrainment rate.

The limitations of these models could be summarized as follows: (a) they are highly dependent on dimensionless groups and sometimes experimental correlations; and (b) they have more or less dependency on the physical process of the targeted mechanism. These limitations reduce the usefulness of these existing models.

According to the author's best knowledge, no CFD model was found to be reported in the open literature.

2.2 Simulation Work Methodologies

The methodologies for conducting the experiments and experimental data analysis of this research are thoroughly described in future chapters. This section introduces the methodologies used for the numerical simulation work. Flow characteristics analysis (discussed later in Chapters 3 and 4) has shown that both the gas core and the liquid film are in the turbulent state and that the film flow has strong features of the near-wall flows. Therefore, a k-ε turbulence model, which should consider the near-wall effects, is employed for the simulation. In addition, a volume of fluid (VOF) scheme is used to reconstruct the interface between the gas phase and the liquid phase. In this section, various versions of the k-ε and VOF models are introduced and the specific schemes that were adopted in this research work are presented.

2.2.1 k-ε Model

The k-ε model has been successfully applied to a wide range of flows including many applications in multiphase flow such as bubbly flows (Gosman et al., 1992; Issa and Oliveira, 1994; Wu and Minemura, 1999; Troshko and Hassan, 2001; Behzadi et al., 2004), slug flows (Moalem Maron et al., 1991; Clarke and Issa, 1997), stratified flows (Meknassi, 2000; Nordsveen, 2001; Newton and Behnia, 2001; Gao et al., 2003a; Shen et al., 2003), annular flows (Huang et al., 1994; Jayanti and Hewitt, 1997; Wongwises and Naphon, 1998; Kishore and Jayanti, 2004), sedimentation phenomena (Lyn et al., 1992; Zhou et al., 1992; Vitasovic et al., 1997; Armbruster et al., 2001), and

other multiphase flow phenomena. Turbulent flows are characterized by small fluctuations of the velocity and pressure fields. These small scale fluctuations are too computationally expensive to resolve. Instead, the instantaneous Navier-Stokes (N-S) equations are time-averaged (or ensemble-averaged) and two additional transport equations for the turbulent kinetic energy, k, and the turbulence dissipation rate, ε, are used to model the small scale fluctuations which appear in the newly-added terms of the averaged N-S equations. This is the reason why k-ε models are also called two-equation models or Reynolds-averaged N-S (RANS) models. By modeling the small scales of the turbulence in the k-ε model, the computational time is greatly reduced. Fluent® CFD software provides three choices for the k-ε turbulence model schemes: standard k-ε model, renormalization-group (RNG) k-ε model, and realizable k-ε model. This section briefly summarizes each scheme and introduces the scheme chosen for this research.

By averaging the exact N-S and continuity equations, all three k-ε models include the same RANS equations. These are written in the Cartesian tensor form as:

Continuity Equation

$$\frac{\partial \rho}{\partial t} + \frac{\partial}{\partial x_i}(\rho U_i) = 0, \tag{2.1}$$

N-S Equations

$$\frac{\partial}{\partial t}(\rho U_i) + \frac{\partial}{\partial x_j}(\rho U_i U_j + \rho \overline{u_i' u_j'}) = -P_{,i} + \frac{\partial}{\partial x_j}[\mu(\frac{\partial U_i}{\partial x_j} + \frac{\partial U_j}{\partial x_i})], \tag{2.2}$$

where U_i and u_i' are the mean and fluctuating velocity components (i = 1, 2, 3); ρ and μ are the density and dynamic viscosity of the fluid; $P_{,i}$ is the pressure gradient; x_i represents the coordinate; and the additional terms, $\rho \overline{u_i' u_j'}$, represent the effects of the turbulence and are called the Reynolds stress tensor. In order to close the RANS

equations, the Reynolds stresses are modeled inside the k-ε models in such a way as to include the effect of turbulence as an increased viscosity. Thus the eddy-viscosity model for the Reynolds stresses is introduced

$$-\rho\overline{u_i' u_j'} = \mu_t\left(\frac{\partial U_i}{\partial x_j} + \frac{\partial U_j}{\partial x_i}\right) - \frac{2}{3}\rho\delta_{ij}k \,. \tag{2.3}$$

Here, k is the turbulent kinetic energy

$$k = \frac{1}{2}\overline{u_i' u_i'}\,, \tag{2.4}$$

and μ_t is defined as the eddy or turbulent viscosity that is related to the k and ε. In addition, two transport equations for the k and ε are added to the averaged N-S equations in all such models.

The standard k-ε model was first proposed by Launder and Spalding (1972). Both the model transport equations for k and ε can be derived from the exact N-S equations, while the derivation for the ε equation involves a great amount of physical reasoning. The standard k-ε model, in essence, is a high Reynolds number turbulence model. It is only valid for fully turbulent flows. Several improvements have been made to the model to improve its performance. The RNG k-ε model and the realizable k-ε model are two types of its variants with superior performance over the standard model where the flow features include strong streamline curvature, vortices, and rotation.

The realizable k-ε model is a relatively new model that was proposed by Shih et al. (1995). It differs from the standard k-ε model in two important ways: (1) it contains a new formula for μ_t; and (2) a new form of transport equation for ε is derived. The second feature makes it more capable of accurately predicting the spreading rate of both planar and round jets. This type of k-ε model, by its nature, is also a high Reynolds

number turbulence model. Initial studies by Shih et al. (1995) and Kim et al. (1997) showed that it provides best performance in separated flows and flows with complex secondary flow. However, it is not clear under exactly what conditions the realizable turbulence model consistently outperforms the RNG model.

The RNG k-ε turbulence model, proposed by Yakhot and Orszag (1986), was derived from the instantaneous N-S equations using a rigorous statistical technique called the "renormalization group" method. This model has a similar form to that of the standard turbulence model, but it differs from it in four ways: (1) The RNG model has a new term in its ε equation which greatly improves the accuracy of simulating rapidly strained flows; (2) the effect of swirl on turbulence is considered in the model, which enhances the accuracy for swirling flows; (3) unlike the standard model which uses constant values in the turbulent Prandtl numbers, the RNG model uses an analytical formula; and (4) it provides an analytically derived differential equation for the effective viscosity (the sum of turbulent viscosity of the flow and the molecular viscosity of the fluid) that accounts for low-Reynolds-number effects.

Mainly because of the last feature, the RNG turbulence model is selected for the simulation work of this research since the liquid film in annular flow has a strong resemblance to the flow in the near-wall region. Also, the enhanced wall treatment method is combined with the RNG model to deal with the near wall region in annular flow. The next section will address this in more detail. In the following section, further details of the RNG model will be discussed since it is employed in this thesis.

The RANS equations for all the k-ε turbulence models are given above. Two additional transport equations in the RNG model are written for k and ε, respectively as

$$\frac{\partial}{\partial t}(\rho k)+\frac{\partial}{\partial x_i}(\rho U_i k)=\frac{\partial}{\partial x_j}(\alpha_k \mu_{eff}\frac{\partial k}{\partial x_j})+G_k+G_b-\rho\varepsilon-Y_M+S_k \quad , \quad (2.5)$$

and

$$\frac{\partial}{\partial t}(\rho\varepsilon)+\frac{\partial}{\partial x_i}(\rho U_i \varepsilon)=\frac{\partial}{\partial x_j}(\alpha_\varepsilon \mu_{eff}\frac{\partial \varepsilon}{\partial x_j})+C_{1\varepsilon}\frac{\varepsilon}{k}(G_k+C_{3\varepsilon}G_b)-C_{2\varepsilon}\rho\frac{\varepsilon^2}{k}-R_\varepsilon+S_\varepsilon . \quad (2.6)$$

G_k is the production of turbulent kinetic energy calculated from

$$G_k=-\rho\overline{u_i' u_j'}\frac{\partial U_j}{\partial x_i}, \text{ and} \quad (2.7)$$

G_b is the generation of k due to buoyancy in terms of gravity and temperature gradient,

$$G_b=\beta g_i\frac{\mu_t}{Pr_t}\frac{\partial T}{\partial x_i} . \quad (2.8)$$

In the present study, $G_b = 0$ since the temperature remains constant.

Y_M is the dilatation dissipation term. It reflects the compressibility of high-Mach number flows on turbulence. For incompressible flows, this term is normally neglected. α_k and α_ε are the inverse effective Prandtl numbers for k and ε. They are computed using the following formula derived analytically from the RNG theory

$$\left|\frac{\alpha-1.3929}{\alpha_0-1.3929}\right|^{0.6321}\left|\frac{\alpha+2.3929}{\alpha_0+2.3929}\right|^{0.3679}=\frac{\mu}{\mu_{eff}} , \quad (2.9)$$

where $\alpha_0 = 1.0$, and μ_{eff} and μ are the effective viscosity and fluid physical viscosity, respectively. S_k and S_ε, are user-defined source terms (both terms are set to zero since there are no specific sources in this research to generate or dissipate k). R_ε is an additional term that makes the RNG model different from the standard k-ε models. It is given by

$$R_\varepsilon = \frac{C_\mu \rho \eta^3 (1-\eta/\eta_0)}{1+\beta\eta^3}\frac{\varepsilon^2}{k}, \tag{2.10}$$

where $\eta = Sk/\varepsilon$ (S is the modulus of strain rate tensor), $\eta_0 = 4.38$, and $\beta = 0.012$. C_μ, $C_{1\varepsilon}$, $C_{2\varepsilon}$, and $C_{3\varepsilon}$, are constants. In Fluent® $C_{3\varepsilon}$ is not specified, but rather is calculated by Fluent®. C_μ, $C_{1\varepsilon}$ and $C_{2\varepsilon}$ have values derived analytically from RNG theory (Choudhury, 1993) and they take values of 0.0845, 1.42 and 1.68, respectively. These default values are adopted in this study.

In the RNG k-ε model, a differential equation is used to calculate the turbulent viscosity, μ_t, where

$$\frac{d(\rho^2 k/\sqrt{\varepsilon\mu})}{d\nu'} = 1.72\frac{\nu'}{\sqrt{\nu'^3 - 1 + C_\nu}} \tag{2.11}$$

and where $\nu' = \mu_{eff}/\mu$ (turbulent kinematic viscosity), $C_\nu = 100$, and $\mu_{eff} = \mu + \mu_t$. It is equation (2.11) that allows the RNG model to better handle low-Reynolds-number and near-wall flows.

2.2.2 Near-Wall Treatment

The k-ε models are primarily valid for turbulent core flows, i.e., the flow in the regions sufficiently far from the walls. In order to make the models more suitable for near-wall flows, special treatments are needed. It is commonly agreed that the near-wall flows are composed of three regions: a viscous sublayer region where molecular viscosity plays a dominant role in the flow transport phenomena, a buffer region where both turbulent and molecular viscosities play important roles, and a turbulent core region where the effect of molecular viscosity can be neglected. Physically speaking,

the viscous sublayer is an extremely thin layer. According to the law of the wall, the velocity profile (White, 1999) in the each region is expressed as

$$\begin{cases} \text{Viscous Sublayer}: & u^+ = y^+ & \text{for} & y^+ < 5, \\ \text{Buffer Region}: & u^+ = 5\ln y^+ - 3.05 & \text{for} & 5 < y^+ < 30, \\ \text{Turbulent Core} & u^+ = 2.5\ln y^+ + 5.5 & \text{for} & 30 < y^+ < 1000, \end{cases} \tag{2.12}$$

where u^+ is a dimensionless velocity = u / u*; u* is the friction velocity = $(\tau_w / \rho)^{1/2}$; τ_w is the wall shear stress; and y^+ is a dimensionless distance from the wall = y u* / ν, where ρ and ν are the fluid density and kinematic viscosity, respectively. This equation group is generally called the "universal velocity profile". It is worth noting that the division of y^+ for each region is not strict. Pope (2000) believed that the viscous contribution can be neglected for $y^+ > 50$, otherwise the viscous contribution is significant (which is correct in both the viscous sublayer and buffer regions). Pope's criterion is adopted for the analysis in this thesis.

Another significant feature of the near-wall region is that the fluid velocity has large gradients in the viscosity-affected region due to the no-slip boundary condition of viscous flows. It follows that if near-wall flow features are critically important in the modeling, carefully chosen meshes must be placed in the near-wall region.

Fluent® subroutines effectively solve this problem by providing a special wall treatment technique known as the enhanced wall treatment method. This is the only method that Fluent® allows for near-wall flow effects. With the above discussion in mind, a coarser mesh is allowed in the viscosity-affected near-wall region with little impact on the accuracy of simulation in that region. This greatly reduces the computational time. For the simulation work of this research, the enhanced wall treatment method for the near-wall region is employed with the RNG k-ε model.

2.2.3 VOF Model

The VOF model is selected to track and resolve the interface between the gas and liquid. Among the three basic formulations to track liquid-gas interfaces in the literature (Lagrangian particle methods, level set methods, and volume of fluid methods), the VOF method is the most developed and robust. Just as in the applications of k-ε models, VOF models have been successfully employed to a wide range of multiphase flow cases. They have been used to simulate the bubble's motion in bubbly flows (Cook and Behnia, 2001; Essemiani et al., 2001; Lörstad and Fuchs, 2004), slug flow (Taha and Cui, 2002; Kang et al., 2004), waves in stratified flow (Gao et al., 2003a), waves in core annular flows (Li and Renardy, 1999), and waves of free-surface flows (Gao et al., 2003b; Hieu et al., 2004). Although no such models are applied to the gas-liquid two-phase annular flow yet, their successful applications to other multiphase flows strengthen the confidence in them. The new version, Fluent® 6.18, provides various VOF schemes for material interface reconstruction.

The VOF methods are designed for two or more immiscible fluids where the ability to predict the position of the interface between the fluids with certainty is of interest. These methods do not directly track the interface; instead they reconstruct the interface. In VOF models, two aspects are very important: the interface reconstruction algorithms and volume advection algorithms. The method used for time integration of the volume advection equation is either one-dimensional (operator split) or multidimensional. One significant identifiable interface reconstruction feature is the assumed interface geometry, which tends to be either piecewise constant, piecewise constant/"stair-stepped", and piecewise linear. The above three schemes were first

introduced by DeBar (1974), Noh and Woodward (1976), and Hirt and Nichols (1981), respectively. Since Hirt and Nichols (1981) first used the term volume of fluid and the acronym VOF to describe their model, many variants have been developed and most of them fall into the above three interface reconstruction categories. DeBar's piecewise linear scheme is generally preferred in modern volume tracking algorithms. Among the pioneering developments of this type of scheme, the PLIC (piecewise linear interface calculation) VOF methods devised by Youngs (1982 and 1987) are the most successful and "have proven to be robust and reasonably accurate…" (Benson, 2002). The methods proposed by Noh and Woodmard (1976) and Hirt and Nichols (1981) are called the SLIC method and the donor-acceptor method, respectively. Figure 2.3 shows the comparison of the three different interface reconstruction methods. Results indicate that PLIC method reconstructs the most accurate interface than others.

Fluent® provides four types of VOF schemes: geometric reconstruction scheme, donor-acceptor scheme, Euler explicit scheme and implicit scheme. The geometric reconstruction approach is directly based on the work of Youngs (1982). In order to calculate the convection and diffusion fluxes through the cell faces for the VOF model, the first two schemes take the special treatment methods as mentioned above; while the latter two methods treat the cells near the interface with the same interpolation as the cells that are completely filled with one fluid or another; no other special treatments are involved. Thus, the latter two schemes cannot capture the interface as accurately as the former two. Based on the above analysis, the geometric reconstruction VOF model is adopted for this research.

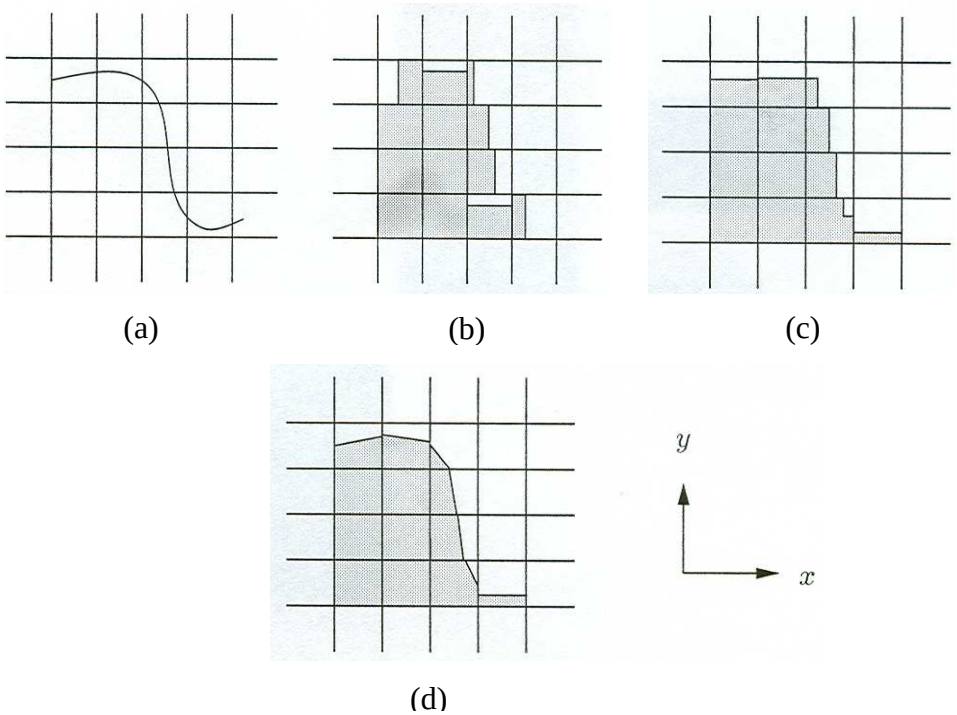

Figure 2.3 Comparison of the three different interface reconstruction methods: (a) exact interface shape; (b) SLIC interface reconstruction; (c) donor-acceptor interface reconstruction; and (d) PLIC interface reconstruction.

In two-phase annular flow, surface tension is believed to be a key force to shape the waves on the interface and hence the effects of this force are included in the VOF model adopted in this research. The surface tension scheme used for the VOF model in Fluent® is the continuum surface force (CSF) scheme proposed by Brackbill et al. (1992). With this model, the surface tension is treated as a source term in the momentum equations. However, when large body forces, such as the surface tension force and gravitational force, exist in multiphase flows, the body force and pressure gradient terms in the momentum equations are almost in equilibrium with the comparably small contributions of convective and viscous terms. The solution solvers combined with the VOF model in Fluent® converge poorly unless partial equilibrium of the pressure gradient and body forces is considered. Thus, in Fluent® an optional

“implicit body force” treatment is provided which can account for this effect and make the solution more robust. In the simulation, this option was turned on.

2.2.4 Solution Algorithm

Fluent® provides two solution algorithms to solve the governing equations for the conservation of mass, momentum, and turbulence scalars: a segregated solver and a coupled solver. Because only the segregated solver in Fluent® can work with the VOF model, it is chosen as the solution algorithm for the simulation work. In this approach, the governing equations are solved sequentially and an iteration method is necessary due to the non-linearity of the governing equations. The solution steps of the segregated solver are outlined below and are illustrated in Figure 2.4:

1. Fluid properties are calculated based on the current solutions (or assumed solutions at the start of the simulation process).
2. Each of the momentum equations for velocities (u, v, and w) are solved in turn using current values for pressure and face mass fluxes. Thus the velocity field is updated.
3. The pressure-correction equation is then solved to obtain corrected pressure and velocity fields. For details of the pressure-correction equation, please refer to Patankar (1980).
4. The turbulence scalar equations for k and ε are solved using the previously updated values of the other variables. If the VOF model is involved, continuity equations of volume fraction for the fluids are also solved.

5. Check the convergence of the equation set. If convergence occurs, stop the calculation; if not, repeat the steps 1-5.

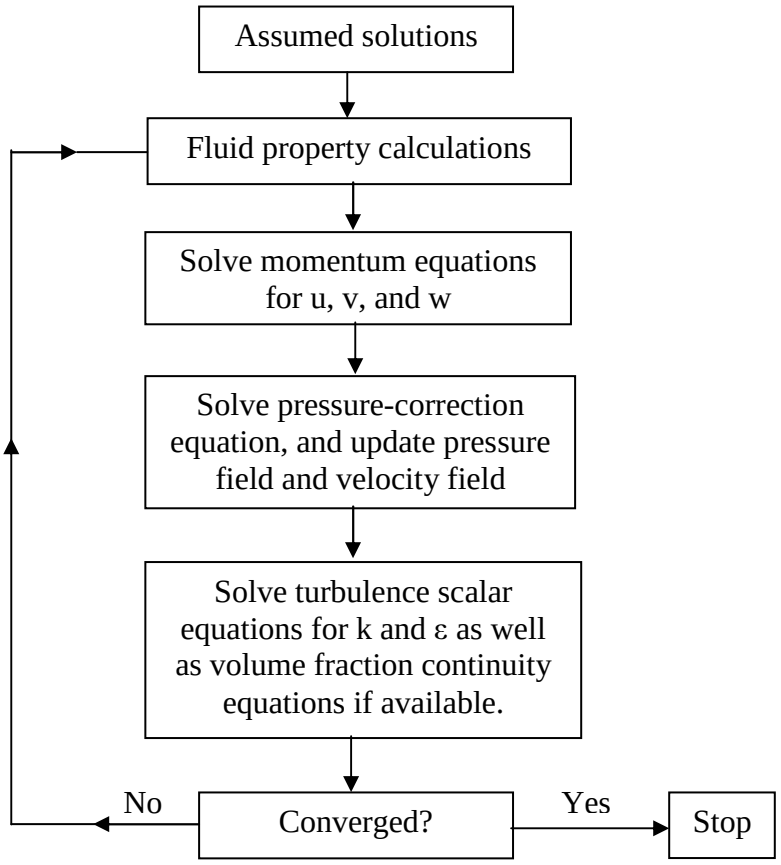

Figure 2.4 Solution steps of the segregated solver.

These solution steps are for a steady state problem. For a transient problem, once the converged solutions are obtained at the current time level, the calculations will go to the next time level and the above steps are repeated.

2.2.5 Discretization Methods

Fluent® uses the control-volume approach (Patankar, 1980) to transform the governing equations into algebraic equations that can be solved numerically. This

approach consists of integrating the differential governing equations over each control volume to yield discretized equations that conserve each quantity on a control-volume basis. Thus, discretization methods are needed for this process and some details are given in this section.

Convection terms: Fluent® provides several selections for the discretization of the convection terms of the governing equations: first-order upwind scheme, second-order upwind scheme, QUICK scheme, and power-law scheme. When the segregated solver is employed, the governing equations are, by default, solved using the first-order upwind discretization for convection. This discretization scheme means the face value ϕ_f is set equal to the volume-centred value of ϕ in the first upstream volume. Due to the following considerations, the default discretization scheme for the convection term is adopted for the simulation work: (1) when the flow is aligned with the grid (quadrilateral or hexahedral grid), which is the case in the simulation, the first-order upwind discretization for the convective term is acceptable since this will not increase the numerical diffusion in the calculations (Patankar, 1980); and (2) although the scheme cannot produce highly accurate results, it generally yields better convergence.

Pressure terms: In Fluent® the default discretization scheme assumes the normal pressure gradient at the wall is zero, which is not valid in the presence of body forces (e.g., gravitational force and surface tension force). The body-force-weighted scheme solves this problem. It computes the face pressure by assuming that the normal gradient of the difference between the pressure and the body forces is constant. This works well if the body forces are known. Therefore, the body-force-weighted scheme is chosen for the discretization of pressure terms in the governing equations.

Pressure-velocity coupling: Pressure-velocity coupling is achieved through the pressure-correction equation which is derived from the continuity and momentum equations. Fluent® provides three algorithms for the pressure-velocity coupling: SIMPLE, SIMPLEC, and PISO, which are proposed by Patankar and Spalding (1972), Issa (1982), and Van Doormaal and Raithby (1984), respectively. Moukalled and Darwish (2002) compared several SIMPLE variants and they concluded that SIMPLE and SIMPLEC have the similar performances on CPU times for some multiphase flow problems and the PISO algorithm is in general more expensive than SIMPLE. The PISO is the acronym of Pressure-Implicit with Splitting of Operators. It also belongs to the SIMPLE family of algorithms. The PISO algorithm is based on a higher degree of the relationship between the corrections for pressure and velocity. One of the limitations of the SIMPLE and SIMPLEC methods is that new velocities and corresponding fluxes do not satisfy the momentum balance after the pressure-correction equation is solved. As a result, iterations are repeated until the momentum balance is met. The PISO algorithm performs two additional corrections to improve the efficiency of the iterations: the neighbour correction and the skewness correction. The skewness correction is for meshes with a high degree of distortion. In this work, a quadrilateral mesh is used, and thus the simulation does not benefit from this feature of PISO. The neighbor correction, also called the momentum correction, is to move the repeated calculations required by SIMPLE and SIMPLEC inside the solution stage of the pressure-correction equation (Issa, 1986). After one or more additional PISO loops, the corrected velocity field meets the continuity and momentum equations more closely. Though the PISO algorithm costs a little more CPU time per solver iteration, it can greatly reduce the number of iterations

required for convergence, especially for transient problems. In addition, the PISO algorithm allows a larger time step while maintaining stable calculations. The above mentioned advantages of the PISO algorithm make it a preferred choice for this research.

Linearization and temporal discretization: In Fluent® each discrete governing equation is linearized implicitly with respect to that equation's dependent variable when the segregated solver is used. For this research, first-order implicit discretization is used for the temporal terms of the governing equations

$$\frac{\phi^{n+1} - \phi^{n}}{\Delta t} = F(\phi^{n+1}), \tag{2.13}$$

where ϕ^{n} and ϕ^{n+1} refer to values at the current time level t and the next time level t + Δt.

However, there are exceptions for the VOF schemes: the linearization of the continuity equations for the volume fraction of the fluids and the discretization of their temporal terms use explicit schemes. The first-order explicit temporal discretization is given by

$$\frac{\phi^{n+1} - \phi^{n}}{\Delta t} = F(\phi^{n}), \tag{2.14}$$

i.e., for VOF schemes, the volume fraction equations are solved using an explicit time-marching scheme. It is known that the explicit scheme is not an unconditionally stable scheme. A balance is needed between the time step and the grid length based on the flow features. In Fluent®, the Courant number is used to control this balance. It is given by

$$\frac{\Delta t}{\Delta x_{\min,\text{cell}} / V_{\max,\text{fluid}}}, \tag{2.15}$$

where $\Delta x_{min,cell}$ is the least grid length of a cell; Δt is the time step; and $V_{max,fluid}$ is the maximum fluid velocity in the x axis direction.

Discretization equations: A discretized scalar governing equation for u, v, w, k or ε contains the unknown scalar variable ϕ at the centre point, P, and the unknown values ϕ_{nb} in its surrounding neighbor volumes. Its linearized form can be written as

$$a_P \phi_P = \sum_{nb} a_{nb} \phi_{nb} + b, \tag{2.16}$$

where a_P and a_{nb} are the linearized coefficients, and b is the source term. In general this equation is non-linear with respect to these variables and hence iteration techniques are necessary for its solution.

2.2.6 Solution Convergence

In this study, the solution convergence is mainly judged by residuals for the solution variables. At the end of each iteration, the residual sum for each of the conserved variables is computed and compared to the convergence criterion. If the criterion is met, the solution for the variable is converged; otherwise, it is not. The criterion is usually set to be smaller than 0.001 for convergence. The residual sum is the sum of absolute values of the residual for each control volume. The residual is also normalized. Based on the discretization equation (2.16), it is defined as

$$R = \frac{\sum_{C.V.S\ P} \left| \sum_{nb} a_{nb} \phi_{nb} + b - a_P \phi_P \right|}{\sum_{C.V.S\ P} \left| a_P \phi_P \right|}, \tag{2.17}$$

where the subscript C.V.S means all the control volumes in the calculation domain.

CHAPTER 3

ANNULAR FLOW FEATURES

3.1 Purpose

Extensive research to accurately describe annular flow features has been conducted in the past by means of experimental, analytical, and numerical methods. In this chapter, an analytical method based on prior experimental data was employed to predict the flow features of the liquid film. For this study, the law of the wall was applied to available liquid film thickness measurements. In addition, flow images relating to disturbance waves and wave entrainment phenomena are presented and the influences of flow parameters on them are studied.

3.2 Experimental Data Analysis

3.2.1 Data Source

The data for this study are the air-water annular flow data collected at microgravity (μg) and normal gravity (1g) conditions by MacGillivray (2004), a former graduate student in the Microgravity Research Group. The microgravity data were collected on board two ESA parabolic flights (Airbus A300; operated by Novespace) during the 29^{th} and 30^{th} European Space Agency Microgravity Science missions. Microgravity refers to the conditions where the gravitational acceleration on the aircraft

is in the range of +/- 0.05 of earth gravity (normal gravity). The normal gravity data were collected using the same apparatus on the ground. For further details on the experimental loop and the measurement procedure and instrumentation, the reader is referred to MacGillivray (2004).

The main information contained in these data sets is the two-phase pressure drop across the test section and the film thickness readings. Other information includes the two phase velocities and system pressure. The data were then processed to obtain the average pressure gradient and the average film thickness (MacGillivray, 2004).

3.2.2 Analysis Method

The law of the wall was introduced earlier as the equation group (2.12). The application of the law of the wall to the liquid film mainly involves the calculations of a dimensionless average film thickness (H^+) based on the measured average pressure gradient and average film thickness. The average pressure gradient is used to calculate the average wall shear stress in annular flow through a force balance. The friction velocity is also computed. Using the friction velocity and the average film thickness, the dimensionless average film thickness is obtained. Finally, H^+ and y^+ in the equation group (2.12) are compared, from which it is determined which range of y^+ the dimensionless liquid film thickness falls in. It should be noted that Pope's (2000) criterion is adopted in this study. This near-wall region reflects the flow state of most of the liquid annular film flow.

Force balance model: Consider a small control volume of length dz which contains both liquid film and gas core from a vertical annular flow in steady state. The

forces acting on it are the wall shear stress, τ_w, pressure force, and the gravitational body force, F_g, as shown in Figure 3.1. Assume the flow fully developed.

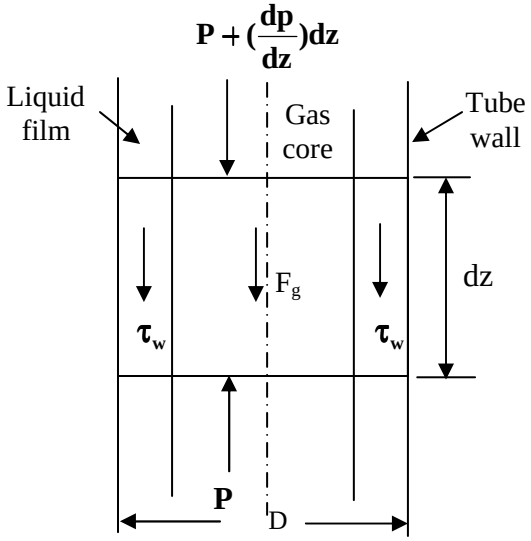

Figure 3.1 Illustration of force balance on the control volume of upward annular flow.

From the force balance, the following result is obtained

$$(P+\frac{dP}{dz}dz)\frac{\pi}{4}D^2+F_g+\tau_w\pi Ddz=P\frac{\pi}{4}D^2. \tag{3.1}$$

Assume the gas void fraction is α ($0 \le \alpha \le 1$), thus,

$$F_g=\{\alpha\rho_g+(1-\alpha)\rho_l\}gdz\frac{\pi}{4}D^2. \tag{3.2}$$

Substitute (3.2) into (3.1), and reorganize the equation to obtain the following result

$$(-\frac{dP}{dz})-[\alpha\rho_g+(1-\alpha)\rho_l]g=\frac{4\tau_w}{D}. \tag{3.3}$$

In annular flow, α is close to unity and ρ_g is small and thus gravitational force is negligible compared to the pressure term. The following result is obtained

$$\tau_w=\left(-\frac{dP}{dz}\right)\frac{D}{4}. \tag{3.4}$$

The average pressure gradient is used to calculate the average wall shear stress using equation (3.4). The friction velocity, u^*, is calculated from

$$u^* = \left(\frac{\tau_w}{\rho_l} \right)^{1/2}. \tag{3.5}$$

The dimensionless average liquid film thickness, H^+, can then be determined by

$$H^+ = \frac{Hu^*}{\nu_l}, \tag{3.6}$$

where H is the average liquid film thickness and υ_l is liquid kinematic viscosity.

3.2.3 Results and Discussion

The above procedure was applied to all experimentally collected annular flow data at μg and 1g conditions using the same experimental loop (Tube ID = 9.525 mm). The results are shown in Figures 3.2 and 3.3. In the two figures, each point represents an annular flow. According to Zhu's (2004) study using the same data, the average liquid film thickness was found to be more strongly influenced by changing the gas mass flow rate than the liquid mass flow rate. Thus the gas mass flow rate is the x-coordinate in the plots, and the dimensionless average liquid film thickness is the y-coordinate. The y-position of each point, H^+, indicates in which near-wall region the film flow falls.

In Figure 3.2 most of the points fall in the region of $16 < y^+ < 50$, where the viscous effects are important in the rate of momentum, mass, and energy transport. It indicates that the flow in the liquid film at normal gravity condition is mainly in the buffer region. In Figure 3.3 most of the points fall in the region of $50 < y^+ < 90$, where turbulence effects dominate. It indicates that the flow in the annular liquid film examined at microgravity condition belongs to the turbulent core regime. These results

suggest that a turbulence model that includes the near-wall flow effects should be used to study the annular flow features.

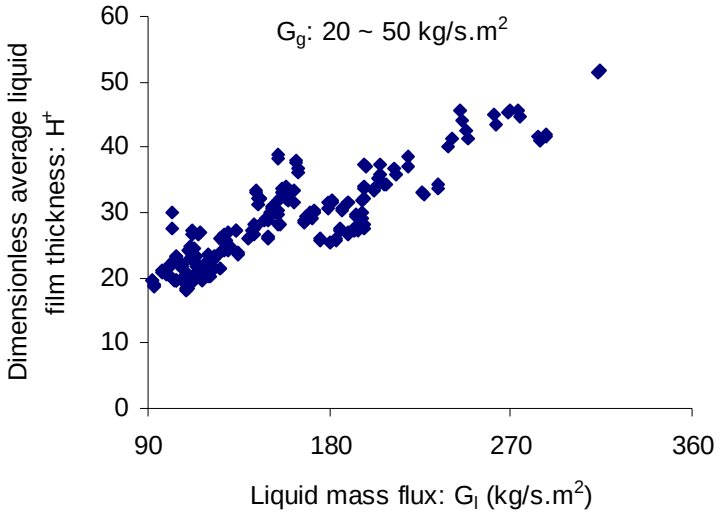

Figure 3.2 Dimensionless average liquid film thickness, H^+, 1g case.

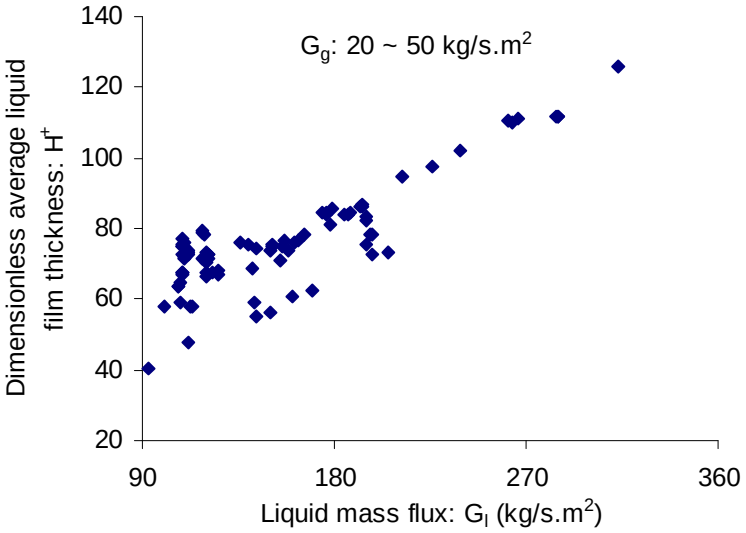

Figure 3.3 Dimensionless average liquid film thickness, H^+, μg case.

In the derivation of the force balance model, gravitational force is considered negligible. The results shown in Figures 3.2 and 3.3 suggest otherwise. To explain the large differences in the dimensionless average liquid film thicknesses (H^+) between 1g

and μg conditions, the definition of H^+ is needed to consider. H^+ is a function of the average wall shear stress multiplied by the average liquid film thickness. While the wall shear stress is not influenced by changing gravity, the liquid film thickness is strongly influenced by the change from 1g to μg. According to the results of MacGillivray (2004), the average liquid film thicknesses at μg are nearly one to two times larger than those at 1g. This perhaps explains why H^+ significantly varies between 1g and μg.

3.3 Video Image Analysis

3.3.1 Introduction

This work is based on the flow images collected by MacGillivray (2004) during ground and microgravity test conditions. MacGillivray collected extensive experimental data on air-water vertical upward annular flow on ground in April and May of 2002. The images of the flows were recorded at the same time using a video camera at a rate of 30 frames/second. In this section, the videotape images are converted into computer images and further detailed studies of the liquid entrainment phenomena are conducted based on the 2-D computer images. The computer images shown below are further magnified, not proportionally, for convenient viewing purposes.

3.3.2 Wave Entrainment Phenomenon

Based on the analysis of the experimental flow images and prior studies of disturbance waves and entrainment phenomena by other investigators, the wave entrainment phenomenon is identified and presented in this section. Woodmansee and Hanratty (1969) pointed out in their work that the initiation of liquid entrainment and the appearance of disturbance waves occur at the same time if the liquid film is very

thin. In this study, the average liquid film thickness in most cases is less than 0.6 mm (MacGillivray, 2004) and therefore meets the requirement. If the disturbance waves could be identified, then the entrainment phenomena could be identified at the same time. When viewed by the naked eyes through the external tube wall, the disturbance waves look like a "milky band" of liquid (Martin and Azzopardi, 1985; Azzopardi, 1986), or patches of "white water" (Wallis, 1969b). In the computer images, the "milky band" or "white water" appears as a black cloudy zone as shown in Figure 3.4.

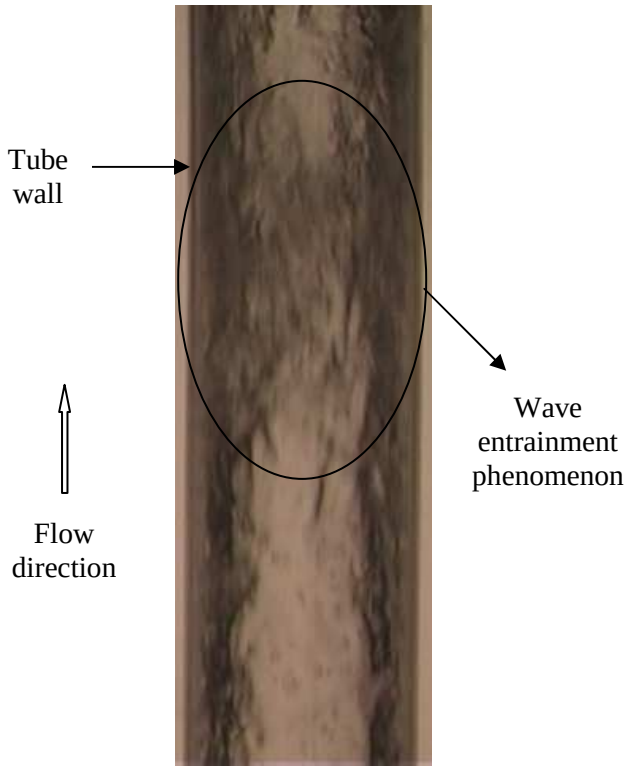

Figure 3.4 A sample image of annular flow (V_{sl} = 0.114 m/s; V_{sg} = 31.0 m/s).

As mentioned earlier, the liquid entrainment is linked to the formation and passing of a disturbance waves in annular flow. In this study, the black cloudy zone in Figure 3.4 is actually due to the combined effect of the disturbance wave "dynamics" and the liquid entrainment. The interface of disturbance waves is rough and is usually covered with many ripples. The liquid entrainment mechanism produces many liquid

droplets with various sizes. The mixed effect of interface roughness and the accumulation of liquid droplets resulting from the entrainment mechanism are given a new name in this study: “Liquid Droplets Cloud Phenomenon (LDCP).”

3.3.3 Parametric Studies of LDCP

The effects of both the gas velocity and liquid velocity on the formation and intensity of the LDCP are discussed in this section. Two features of the LDCP are considered in this study: (1) occurrence frequency and (2) intensity. The occurrence frequency of the LDCP is determined by counting the frames of computer images with LDCP within two-second periods. Due to the limited frame rate of the camera compared to the flow velocity, some flow information between consecutive flow images could be missed. Therefore, the actual frequency of the LDCP will likely be higher than the one counted using this method. If the captured pictures are considered as the even-time samplings and that the information deduced from the images to reflect the whole flow condition, then it must be concluded that the occurrence frequency of the LDCP and any subsequent conclusions must be treated as qualitative rather than quantitative. The intensity of the LDCP, on the other hand, is judged by the repeated observations of the captured images.

(1) LDCP at high vs. low velocities

Occurrence frequency: Both the LDCP occurrence frequency and intensity were investigated at high and low gas and liquid velocities. The frequency results are listed with flow conditions in Table 3.1.

Table 3.1 Occurrence frequency of LDCP at different gas-liquid velocities

File name	V_{sl} (m/s)	V_{sg} (m/s)	LDCP frequency (1/s)
R-Para12	0.288	25.7	12
Para 108	0.097	18.7	9.5

In table 3.1, V_{sl} and V_{sg} are liquid and gas superficial velocities, respectively. Table 3.1 indicates that the LDCP occurs more frequently at higher gas-liquid velocities than at lower gas-liquid velocities, which suggests that liquid entrainment becomes more and more active with the increase of both phase velocities.

The 2-D flow images of Figures 3.5 and 3.6 qualitatively show the difference in the LDCP intensity between the two cases.

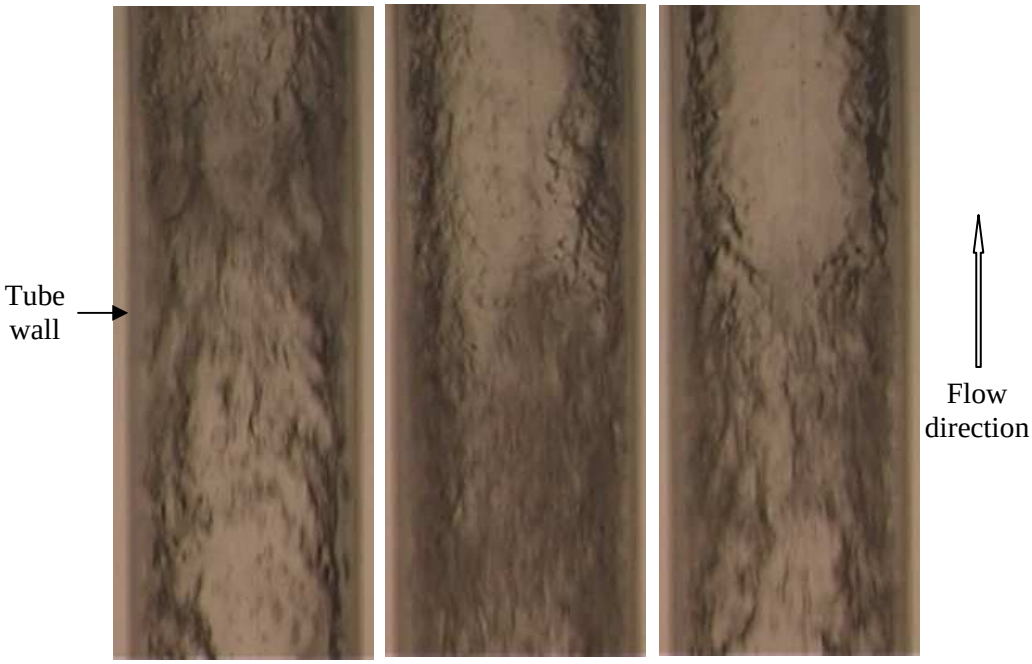

Figure 3.5 LDCP intensity of the annular flow at V_{sl} = 0.288 m/s and V_{sg} = 25.7 m/s.

Intensity: Figures 3.5 and 3.6 each show three frames with LDCP within one second. Comparing the two figures, it can be seen that the LDCP is more intense at higher gas and liquid velocities than at lower ones. Flow images without LDCP are also presented in Figure 3.7.

Figure 3.6 LDCP intensity of the annular flow at V_{sl} = 0.097 m/s and V_{sg} = 18.7 m/s.

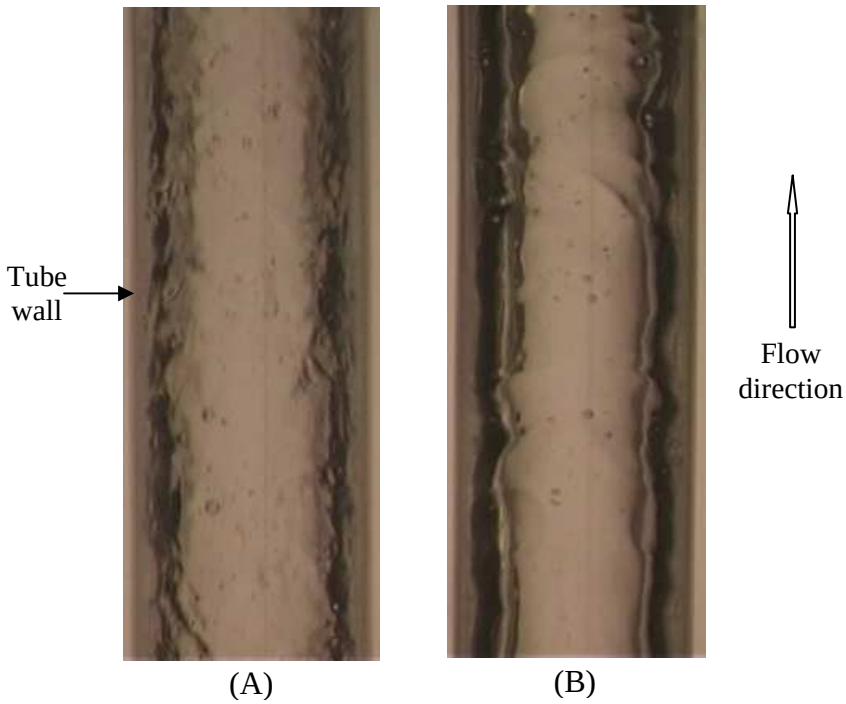

Figure 3.7 Flow images without LDCP of annular flows at: (A) V_{sl} = 0.288 m/s and V_{sg} = 25.7 m/s; and (B) V_{sl} = 0.097 m/s and V_{sg} = 18.7 m/s.

Figure 3.7 shows less intensity of the LDCP process and also suggests that the interface is “rougher” at higher gas-liquid velocities than at lower ones. This could be attributed to the presence of more small ripples with various scales covering the interface at higher velocities. From the entrainment fraction measurements, the greater the gas-liquid velocities, the higher the liquid entrainment fraction becomes. This perhaps explains why the rougher gas-liquid interface and the more liquid droplets present in the gas core contribute to the flow image at higher gas-liquid velocities becoming more “misty”.

To summarize, at higher gas-liquid velocities, both the frequency and intensity of LDCP are strengthened compared to conditions of lower gas-liquid velocities. In the following analysis, the influence of the individual phase velocity on the LDCP is presented and discussed.

(2) Influence of changing the liquid velocity on LDCP

Occurrence frequency: The LDCP frequencies at constant gas velocities and changing liquid velocities are listed in Table 3.2.

Table 3.2 Occurrence frequency of LDCP at different liquid velocities

File name	V_{sl} (m/s)	V_{sg} (m/s)	LDCP frequency (1/s)
R-Para 7	0.189	25.9	12.5
R-Para 10	0.227	25.9	12.5
R-Para 12	0.288	25.7	12

Table 3.2 suggests that changing the liquid velocity has little or no influence on the LDCP occurrence frequency in this study.

Intensity: The LDCPs of two annular flows listed in Table 3.2 are compared: flow R-Para12 with the maximum liquid velocity, and flow R-Para7 with the minimum liquid velocity. Flow images with LDCP of the flow R-Para12 have already been presented in Figure 3.5. Flow images of the flow R-Para 7 are presented in Figure 3.8. Comparison of the two figures indicates that the intensity of the LDCP is strengthened at higher liquid velocity. This, in turn, suggests that either the liquid entrainment is strengthened or the interface of the disturbance wave becomes rougher, or possibly both effects are present. It is known that the liquid entrainment fraction in annular flow increases with increasing the liquid velocity according to entrainment fraction measurements made by this author and several others. Thus, at least the former suggestion exists.

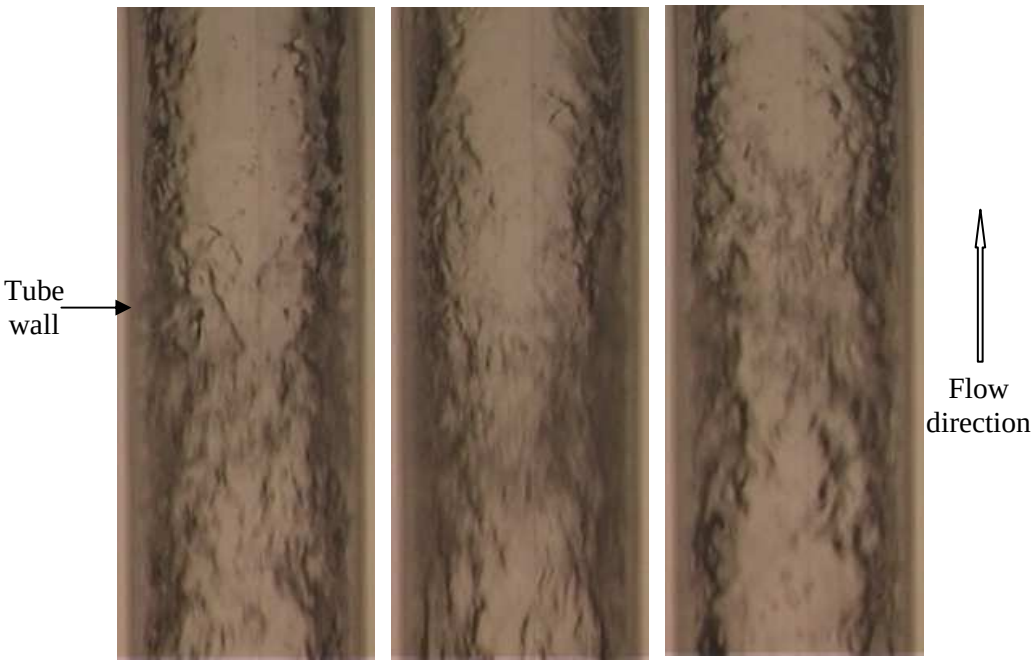

Figure 3.8 LDCP intensity of annular flow at V_{sl} = 0.189 m/s and V_{sg} = 25.9 m/s.

In summary, and qualitatively speaking, the occurrence frequency of the LDCP does not appear to depend on the liquid velocity, while the LDCP intensity is strengthened with the increase of the liquid-phase velocity.

(3) Influence of changing the gas velocity on LDCP

Occurrence frequency: The LDCP frequency at a constant liquid velocity and varying gas velocities is presented in Table 3.3.

Table 3.3 Occurrence frequency of LDCP at different gas velocities

File name	V_{sl} (m/s)	V_{sg} (m/s)	LDCP frequency (1/s)
Para85	0.112	18.7	8.5
Para86	0.112	27.6	13.5
Para87	0.114	31.0	11.5

The results show that the occurrence frequency of LDCP increases with increasing the gas velocity, suggesting an enhanced entrainment at higher gas velocity.

Intensity: Two sets of flow images are compared: flow Para87 with the maximum gas velocity and flow Para85 with the minimum gas velocity, as shown in Figures 3.9 and 3.10, respectively. The figures, qualitatively speaking, suggest that the intensity of the LDCP is strengthened at higher gas velocities. It has been previously demonstrated that the liquid entrainment fraction in annular flow increases with increasing the gas velocity which in turn could explain the difference.

It is concluded that, once again qualitatively speaking, the occurrence frequency and intensity of the LDCP increase with the increase of gas velocity.

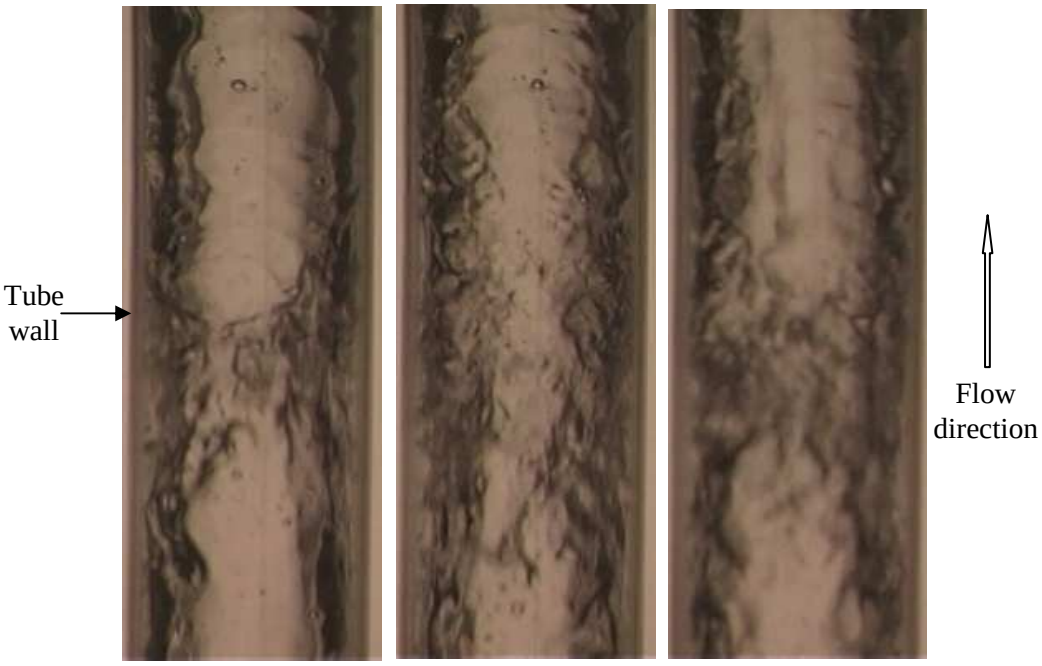

Figure 3.9 LDCP intensity of annular flow at V_{sl} = 0.112 m/s and V_{sg} = 18.7 m/s.

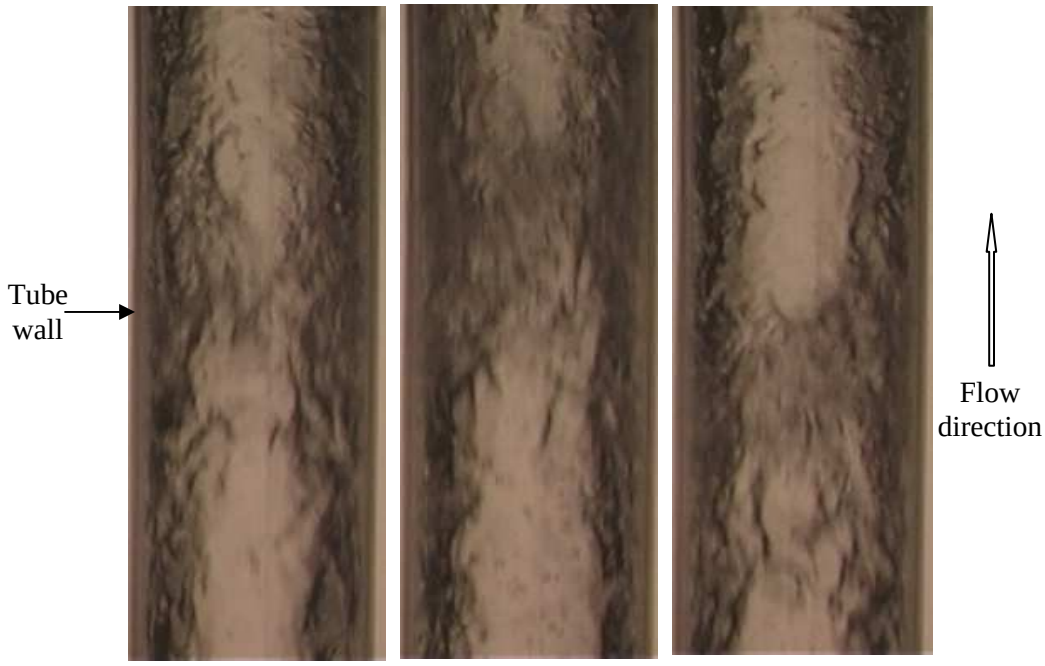

Figure 3.10 LDCP intensity of annular flow at V_{sl} = 0.114 m/s and V_{sg} = 31.0 m/s.

3.4 Summary

Using the data of the average pressure gradient, the average wall shear stress was calculated. The wall shear stress was further used to calculate the friction velocity and the dimensionless average film thickness, H^+. It was determined that the flow in the liquid film belongs to the buffer region at 1g. At μg, the dimensionless average film thickness of most annular flows is in a range of the turbulent core region. Therefore, it is concluded that the liquid film flow has strong features of the near-wall turbulent flow. This conclusion is important in the modeling work.

Flow images of annular flow were examined to improve the understanding of the liquid entrainment phenomena. Because of the low frame rate, and the fact that images are presented in a 2-D fashion, the results are more qualitative than quantitative. The results can be summarized as follows:

(1) The LDCP occurrence frequency is not sensitive to the liquid velocity while the intensity is strengthened with the increase of the liquid velocity;

(2) The LDCP occurrence frequency and intensity increase with the increase of the gas velocity.

CHAPTER 4

SIMULATION I: FLOW FEATURES IN THE GAS CORE

4.1 Purpose

This chapter explores the flow characteristics in the gas core of annular flow using CFD techniques. A two-dimensional, steady-state numerical model was constructed for the gas core. The model employs the RNG k-ε turbulence model and the enhanced wall treatment method. A physical wave model, developed earlier by Zhu (2004), provides information on the boundary conditions for the numerical model. The results of the simulation provide new insights into the velocity profile, velocity contour, pressure contour, and interfacial shear stress distribution in the gas core.

4.2 Background on Annular Flow Modeling

CFD techniques are frequently employed in the simulation of interfacial dynamics where in-situ measurements are difficult or impossible to make. In annular gas-liquid flows, there are challenges with the application of CFD techniques. For example, if the simulation is to include the entire two-phase flow domain, a major challenge arises in accurately modeling the very “chaotic” interface. If the simulation is

focused only on one of the two phases of annular flow, such as the gas core or the liquid film, this greatly simplifies the work. However, the interfacial wave configuration and its dynamic properties are not well known or understood since the two-phase interface is almost always covered with waves of different types and different scales. As such, it is difficult to determine the exact calculation domain for the gas core or the liquid film, and hence the exact boundary conditions for the purpose of simulation. In an effort to simplify the above mentioned conditions, Jayanti and Hewitt (1997) assumed, as a reasonable compromise, a sinusoidal wave profile and adopted established empirical friction factor correlations for the wavy interface to determine the wave velocity. They used standard and low-Reynolds-number k-ε models in the liquid film to explore the features of the concurrent air-water annular flow. They concluded that the low-Reynolds-number turbulence model was more suited to explore the film flow features. Interestingly, a similar conclusion has been presented in the previous chapter. In both cases, a steady-state model was developed. Wongwises and Naphon (1998) assumed a smooth gas-liquid interface of countercurrent air-water annular flow in their modeling. They further assumed that the mean liquid-film velocity was equal to the interfacial velocity. They built a standard k-ε transient model in the gas core, coupled with heat and mass transfer models, to obtain the temperature field and mass fraction of vapor in the gas core. Kishore and Jayanti (2004) also assumed a smooth gas-liquid interface in their steady-state model. The simulation adopted a standard k-ε turbulence model and a modified wall function as the near-wall-treatment method. Unlike the two previously mentioned models, the effect of droplets was considered by solving an additional scalar transport equation for the mass fraction of the droplets. Entrainment and deposition of

droplets were included as a source term and a boundary condition in the mass fraction equation. The model predicted pressure gradient and film thickness results agreeable with the experimental data available in the literature. Due to the limitation of the near-wall treatment method, this model could not provide detailed information on the liquid film.

It is reasonable to say that a common shortcoming of the current models is due in large part to the treatment method used for the gas-liquid interface configuration and its dynamic properties. Due to lack of accurate measurements of the interface dynamics, either a simple wave shape was assumed or even a smooth gas-liquid interface was adopted in many of the solution models. To supplement this deficiency of lacking interface properties, usually empirical correlations were applied to calculate its dynamic properties or other simple assumptions were made. In most cases, such simplifications of the interface configuration discounted the accuracy and reliability of the simulation results.

In this study, the physical wave model of Zhu (2004) is used to provide a more accurate interface shape based on extensive experimental measurements. In addition, it is commonly believed that entrained liquid droplets play an important role in the mass, momentum, and heat transfer processes in annular flow. Among all the previously mentioned models, only one model included the liquid entrainment effects. In this study, the liquid entrainment influence was considered in a simple way. Its influence on annular flow was reflected in the calculations of the physical properties of the two phases, such as the density and viscosity of the mixture in the gas core, and the mixture mass flow rate. In the present model, the annular flow was assumed fully developed,

and the liquid entrainment process was assumed to have reached an equilibrium state (the liquid entrainment fraction remains constant). In the simulation, experimental data of the liquid entrainment fraction were also used.

4.3 Modeling

4.3.1 Model Formulations

The study of Zhu (2004) clearly showed that disturbance waves dominate the two-phase interface in all of the cases in this study. Due to the axisymmetry and circumferential coherence of the disturbance waves in fully developed annular flow in small-diameter tubes, a steady-state two-dimensional numerical model is deemed appropriate for the present simulation work. Therefore, a 2-D numerical model was applied to the gas core.

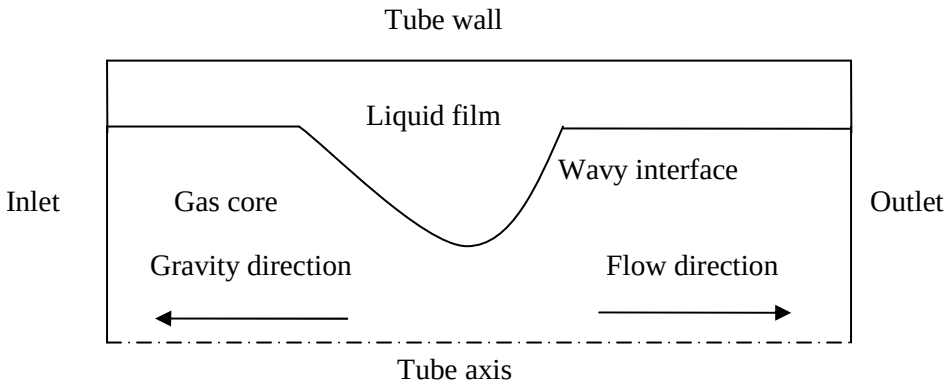

Figure 4.1 Calculation domain of the gas core in annular flow; liquid film with one wave length (wave peak region is magnified).

The simulation domain is schematically shown in Figure 4.1. For convenience, it is placed horizontally and the liquid film region is also shown in the sketch. Due to symmetry, only one-half of the gas core domain is used in the calculation. The

simulation domain is chosen as one wavelength in the flow direction. The domain, therefore, consists of the tube axis, a wavy interface (disturbance wave), and wave inlet and outlet. It should be noted that the wavy interface is directly based on the physical wave model. The model provides a detailed wave configuration and wave velocity. In the simulation, the wavy interface was treated as a moving wall with a net wave velocity in the flow direction. This moving wall assumption of the interface is popular among researchers and was adopted in many simulations of separated flows.

The wave inlet and outlet are treated as periodic boundary condition in the simulation. Assuming that the disturbance wave keeps its shape in a fully developed annular flow, which is a common assumption in the literature of modeling work, then the inlet of a wave is in fact the outlet of the next closest upstream wave. Similarly, the outlet of a wave is the inlet of its closest downstream wave. Except for the pressure, all flow variables (e.g., velocity, turbulent kinetic energy, and turbulent kinetic energy dissipation rate) have the same corresponding distribution at the wave inlet and outlet. The pressure distributions at the inlet and outlet are identical, the only difference being their respective positions. In other words, if the pressure distribution at the inlet is subtracted by a constant, it will coincide with the distribution at the outlet. This constant results from the pressure drop that drives the net mass of fluid in the flow direction. Patankar et al. (1977) presented detailed studies on these, allowing for periodic boundary conditions to be employed at the inlet and outlet of the flow domain as shown in Figure 4.1. In Barbosa et al. (2002), the liquid droplet concentration was almost uniform in the radial direction in a fully developed annular flow. Thus it was appropriate to treat the water droplets and air in the gas core as an incompressible

mixture since both phase velocities and system pressures were low. In addition, flow temperature changed very little in the adiabatic annular flow. Measured entrainment fraction data, in Chapter 5, were used in the calculation of mixture density and viscosity. A formula, in terms of the momentum conservation law, was proposed to calculate the "dynamic" mixture density as equation (4.1). The derivation of this equation is shown in Appendix A.

$$\rho_h = \frac{(\dot{m}_g + \dot{m}_{TD})^2}{\frac{(\dot{m}_g)^2}{\rho_g} + \frac{(\dot{m}_{TD})^2}{\rho_l}}, \tag{4.1}$$

where $\dot{m}_{TD}$ and $\dot{m}_g$ are the mass flow rates of the entrained liquid droplets and the gas phase, respectively, and ρ_h is the density of the mixture (gas phase and liquid droplets). A correlation proposed by Dukler et al. (1964) is adopted here to calculate the mixture viscosity,

$$\mu_h = \mu_g \frac{x\rho_h}{\rho_g} + \mu_l \frac{(1-x)\rho_h}{\rho_l}, \tag{4.2}$$

where μ_l, μ_g, and μ_h are respectively the viscosity of liquid phase, gas phase, and mixture in the gas core; and x is the gas quality.

4.3.2 Turbulence Model

For annular flow, the gas core is always in the turbulent state due to the high gas velocity associated with this type of flow regime. In this study, the Reynolds number of the gas-droplets mixture, based on the actual mixture velocity and gas-core dimensions, is estimated in a range of 1.5×10^4 to 4.0×10^4 for all the tested data. Hence, a RNG k-ε

turbulence model is used in Simulation I, in conjunction with an enhanced wall treatment method and the commercial software (Fluent® 6.18).

4.3.3 Boundary Conditions

Based on the above analysis, a periodic boundary condition (B.C.) was applied to the inlet and outlet, a moving wall B.C. was applied to the wavy interface, and an axisymmetric B.C. to the tube axis. The experimental data sets that were collected by MacGillivray (2004) at normal and microgravity conditions had been applied to the periodic B.C. In the data, the overall flow pressure gradient is known. The velocity of the moving wall is obtained from the physical wave model of Zhu (2004).

4.3.4 Convergence

To reach convergence, residuals were monitored for the radial velocity, V; streamwise velocity, U; turbulent kinetic energy, k; kinetic energy dissipation rate, ε; and mass balance, Δm. The convergence criterion for all the variables is 10^{-6}. In addition, the mass flow rate of the gas-droplets mixture is also monitored at one cross-section to ensure that it reaches a constant value when the model converges.

4.3.5 Mesh

Since the air-water interface is assumed as a moving wall and due to the near wall flow effect, the mesh is heavily concentrated near the interfacial region. The mesh in the other region is evenly distributed. Some information on the wave structure and mesh node number is shown in Table 4.1. The mesh-distribution characteristics in the calculation domain are shown in Figure 4.2.

Table 4.1 Wave structure and mesh nodes

	Wavelength	Wave interface to tube axis at inlet
Dimension	131.9 mm	3.99 mm
Mesh nodes	350 (axial direction)	42 (radial direction)

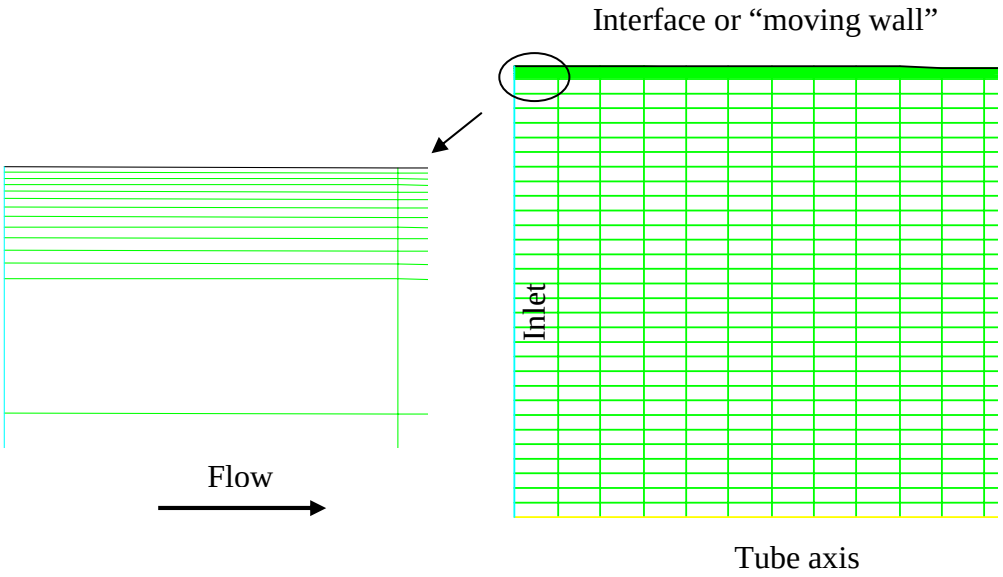

Figure 4.2 Mesh distribution characteristics: mesh at the enlarged inlet and interfacial regions (produced by Fluent® 6.18).

4.3.6 Input Parameters

The input parameters to Fluent® 6.18 include physical properties of the gas-liquid mixture and operating parameters of flow. Physical properties include density and viscosity, as shown in Table 4.2. Flow operating parameters refer to the mixture mass flow rate, the overall flow pressure gradient, and the wave velocity, as shown in Table 4.3. In this model, the pressure gradient and wave velocity were input into Fluent® 6.18 as values of boundary conditions. The mixture mass flow rate is used to validate the model and to calculate the physical properties of the mixture in the gas core.

The mixture mass flow rate is the sum of entrained liquid droplet mass flow rate and the gas phase mass flow rate. The entrained liquid mass flow rate is calculated

according to the entrainment fraction experimental data. Thus, once the gas flow rate and liquid entrainment fraction data are known, the mixture mass flow rate can be solved. For further analysis, the mixture mass flow rate from this method is called the experimental mixture mass flow rate. Based on the turbulence model in the gas core and the input data of wave velocity and pressure drop, a simulated mixture mass flow rate can be also obtained. The two values of mixture mass flow rates are compared, and if they agree, then the results are considered reliable.

Table 4.2 Physical properties

	Density (kg/m^3)	Dynamic viscosity (kg/ms)
Gas: air	1.2	1.8×10^{-6}
Liquid: water	998	10^{-3}
Mixture (air + droplets)	1.79	1.82×10^{-6}

Table 4.3 Flow operating parameters

Gas mass flow rate $\dot{m}_g$ (kg/s)	0.00228
Liquid mass flow rate $\dot{m}_l$ (kg/s)	0.02045
Experimental entrainment fraction E (%)	2.3
Experimental mixture mass flow rate (kg/s)	0.00275
Pressure gradient (-dp/dx) (Pa/m)	2266
Average film thickness H (mm)	0.251

4.4 Results and Discussion

4.4.1 Model Validation

The validation of the model is carried out in two stages. In the first stage, the predicted results for single-phase flow are compared with theoretical/numerical results

for laminar and turbulent pipe flows. In the second stage, the predictions of the model for annular flow are compared with the experimental data and the analytical results. The theoretical results of laminar pipe flow are taken from White (1999) and the numerical results of turbulent pipe flows are taken from Bhaskaran (2002). The mean velocity profile and pipe mass flow rate from the current model are compared with those of White and Bhaskaran, respectively. The results show a strong agreement in both cases. This agreement strengthens the case presented in this thesis that a RNG k-ε turbulence model used with a well-selected enhanced wall treatment method is a good combination to model common turbulent axisymmetric duct flows. The details of the validation of the second stage are given here as they pertain directly to the present study.

In the second stage, the validation is made by comparing two types of data: the mass flow rate of the mixture in the gas core and the average shear stress on the interface (called moving wall in the simulation). During the simulation process, the mixture mass flow rate at a certain cross-section of the calculation domain is monitored. The results showed that the mass flow rate reached an asymptotic value of 0.00240 kg/s when all variables met the convergence criteria. The relative difference with the actual mixture mass flow rate was 12.7 %. The experimental value of mixture mass flow rate was determined to be 0.00275 kg/s, as shown in Table 4.3. Considering that this result is acceptable, it partly validates the model. The other comparison is the average shear stress on the interface. The simulation value of the average interfacial shear stress was 4.65 Pa; while, the analytical value on the basis of a homogeneous flow model (Whalley, 1987b) was 5.07 Pa. Their relative difference is 8.3%, which is an acceptable result. The derivation of the homogeneous flow model is presented in Appendix B.

4.4.2 Mesh-Independence Calculations

A finer mesh was devised to test if the originally chosen "standard mesh" meets the simulation requirement to produce mesh-independent results. The finer mesh had similar features as the standard one, with the difference being that the nodes are increased to 650 in the axial direction and 52 in the radial direction of the calculation domain. The results from the comparisons of the simulation results from the two meshes in terms of the mixture mass flow rate in the gas core and the velocity profile at an axial position x = 10 mm are shown in Table 4.4 and in Figure 4.3.

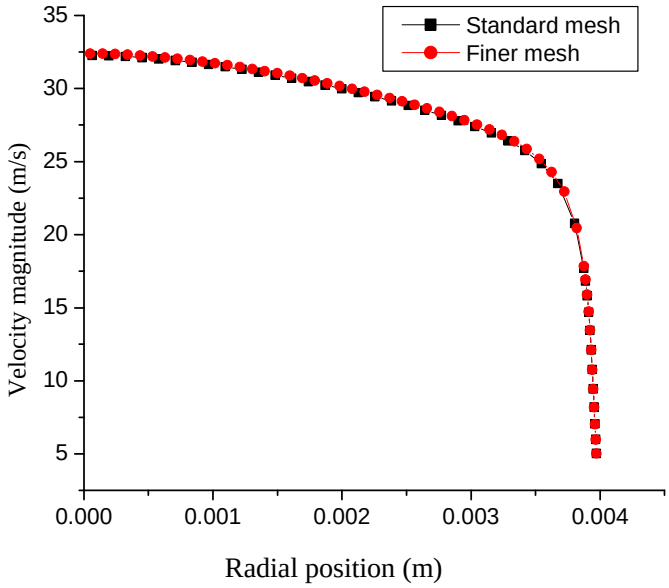

Figure 4.3 Mesh-independence calculations: comparison of the velocity profile of the two meshes at x = 10 mm.

Table 4.4 Mesh-independence calculations: comparison of simulated mixture mass flow rate in the gas core of the two meshes

	Standard mesh	Finer mesh	Relative difference
Mixture mass flow rate	0.00240 kg/s	0.00241 kg/s	0.4 %

From these results, it can be deduced that the standard mesh meets the simulation requirement to produce mesh-independence results.

4.4.3 Sensitivity Studies

The purpose of this section is to evaluate the effect of certain assumptions and choice of parameters on the simulation results. These include: (a) position of the wave profile to the tube wall, (b) wave velocity, (c) pressure gradient, (d) density of the mixture, and (e) viscosity of the mixture. The "base" and "new" cases are shown in Table 4.5. The calculations are obtained with the model settings for each calculation being the same as those of the base case (except for the studied parameter and those influenced by the studied parameter). The results are presented in terms of the changes in the mixture mass flow rate of the gas core.

Table 4.5 Specific cases for the sensitivity studies

Sensitivity calculations	Base case	New cases			
Position of wave profile (mm)	0.8954	0.6954	0.7954	0.9954	1.0954
Wave velocity (m/s)	4.5733	2	3	5	6
Pressure gradient (Pa/m)	-2266	-1522	-1800	-2400	-2931
Mixture density (kg/m^3)	1.79	1.3	1.6	1.9	2.0
Mixture viscosity ($\times 10^{-6} Ns/m^2$)	1.82	1.4	1.6	1.9	2.0

Sensitivity of wave profile position: The wave profile position along the tube wall is in fact related to the average film thickness. The position along the tube wall is adjusted as shown in Table 4.5. The simulated mixture mass flow rates in the gas core are compared with the experimental values and the results are shown in Figure 4.4. It can be seen from the figure that the closer the wave profile is to the tube wall, the larger the difference between the simulation results and the experimental values. In essence,

increasing the distance between the wave profile and the tube wall has the same effect as reducing the gas core passage for the mixture to flow. It can be also noted that the simulated mixture mass flow linearly changes with the wave profile position within the adjusted range. From the linear trend, the simulation mass flow rate changes about 0.6 % when the wave position changes about 1 %. Thus, it is concluded that the wave position moderately affects the simulation results.

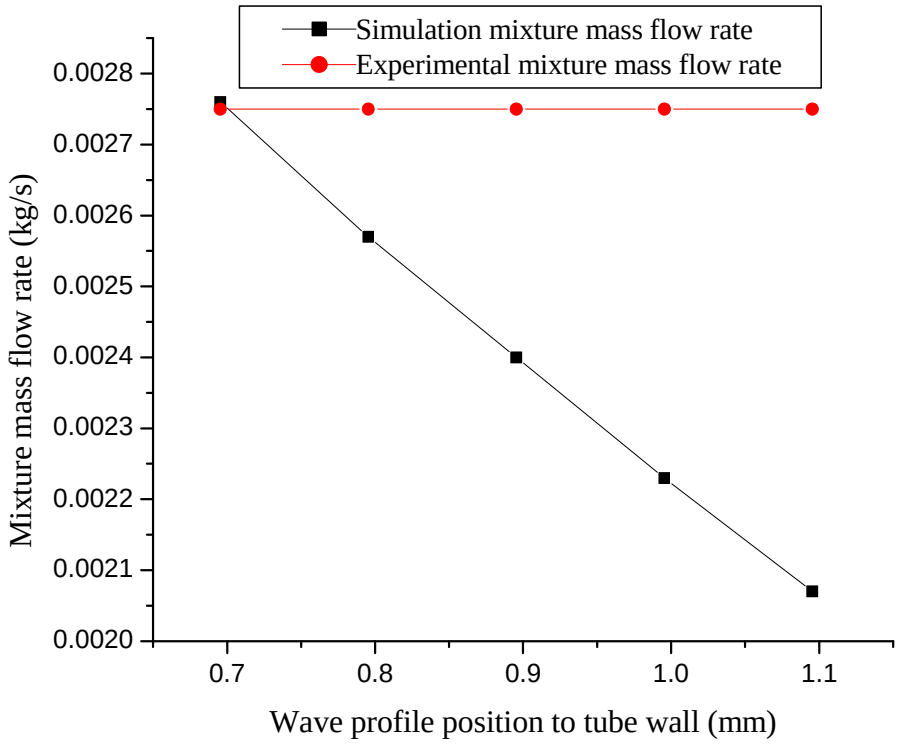

Figure 4.4 Sensitivity of calculations to the wave profile position from the tube wall.

Sensitivity of wave velocity: Figure 4.5 shows the influence of wave velocity on the simulation results. It can be seen that the higher the wave velocity, the larger is the difference in the mass flow rate. As mentioned earlier, the wave has been assumed as a moving wall in the modeling exercise. Thus, a higher wave velocity leads to a higher

gas velocity near the wave region. This increases the mass flow rate of the mixture in the gas core. Figure 4.5 indicates that simulation results moderately change with the wave velocity in a linear fashion. For every 1 % change in the wave velocity, the mixture mass flow rate changes by about 0.14 %. Thus, it is concluded that the simulation results are insensitive to the wave velocity.

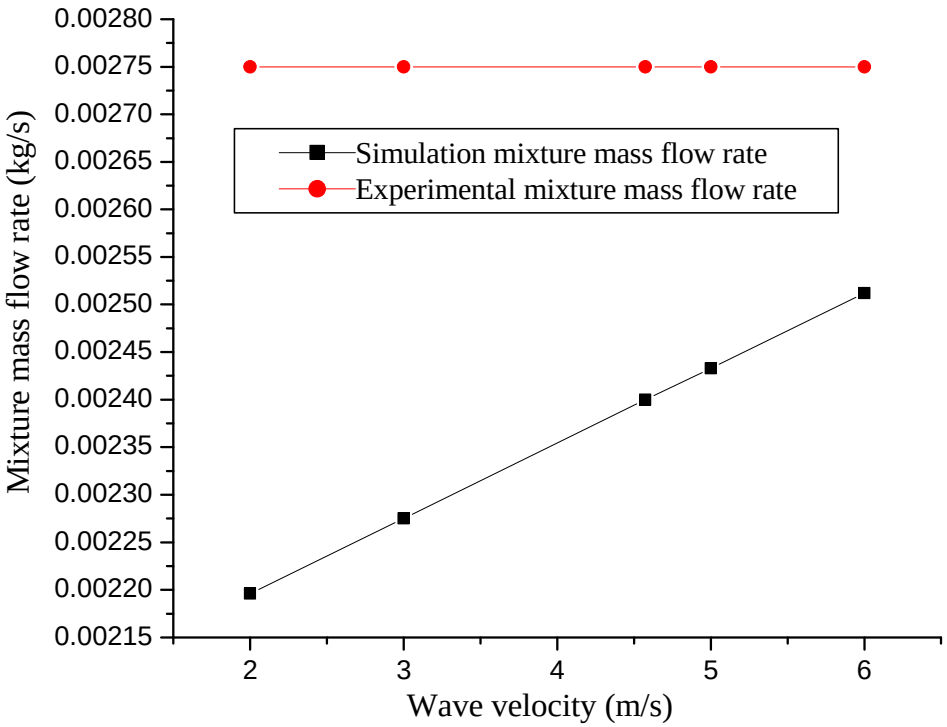

Figure 4.5 Sensitivity of calculations to the wave velocity.

Sensitivity of pressure gradient at tube inlet and outlet: The pressure gradient is negative since pressure decreases in the flow direction. The pressure gradient is used as an input to the model. Its influence on the simulation results is shown in Figure 4.6. The figure indicates that the mixture mass flow rate linearly changes by approximately 0.5

% for every 1 % change in the pressure gradient within the adjusted range. The sensitivity of the mixture mass flow rate to the pressure gradient is moderate.

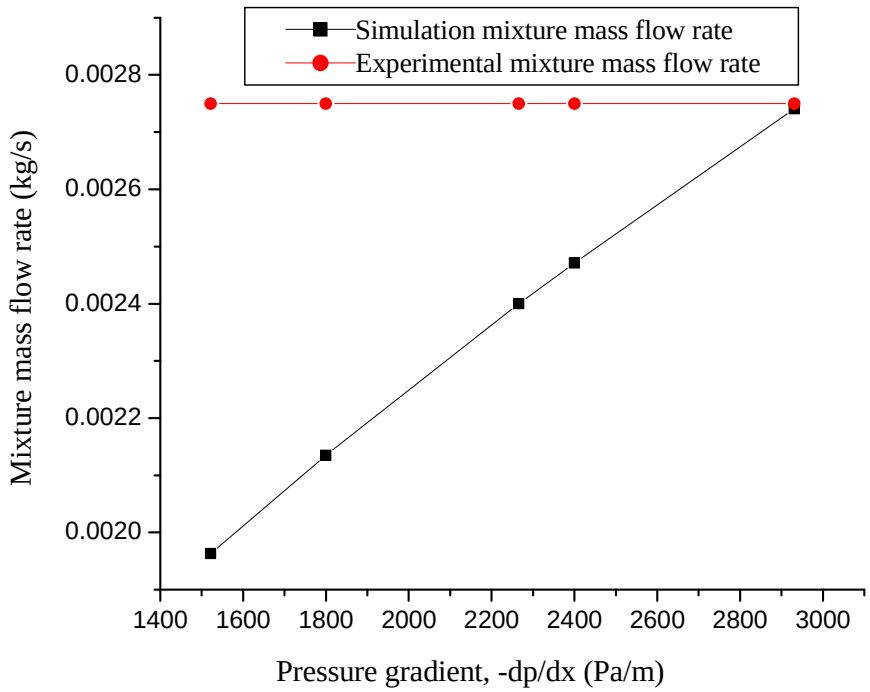

Figure 4.6 Sensitivity of calculations to the pressure gradient.

Sensitivity of the mixture density: A method based on the momentum conservation law is used to calculate the mixture density in the simulations. In the sensitivity calculations, the mixture density changes within a reasonable range. The results of Figure 4.7 indicate that the mixture mass flow rate linearly increases with the increase of the mixture density. This trend in many ways is self-evident. It is found that the mass flow rate changes by 0.6 % ~ 0.7 % for every 1 % change in the mixture density. This also indicates that the sensitivity of the simulation results to the mixture density is moderate.

Sensitivity of the mixture viscosity: A correlation is used to calculate the mixture viscosity. In these calculations, some reasonable values are used. The results of Figure 4.8 clearly show that the mixture mass flow rate linearly decreases with the increases of the mixture viscosity. The increase of the mixture viscosity means an increase of the flow friction, thus the mixture flow rate decreases. Figure 4.8 indicates that the mass flow rate changes by 0.2 % for every 1 % change in the mixture viscosity. It is concluded that the mixture mass flow rate is insensitive to the mixture viscosity.

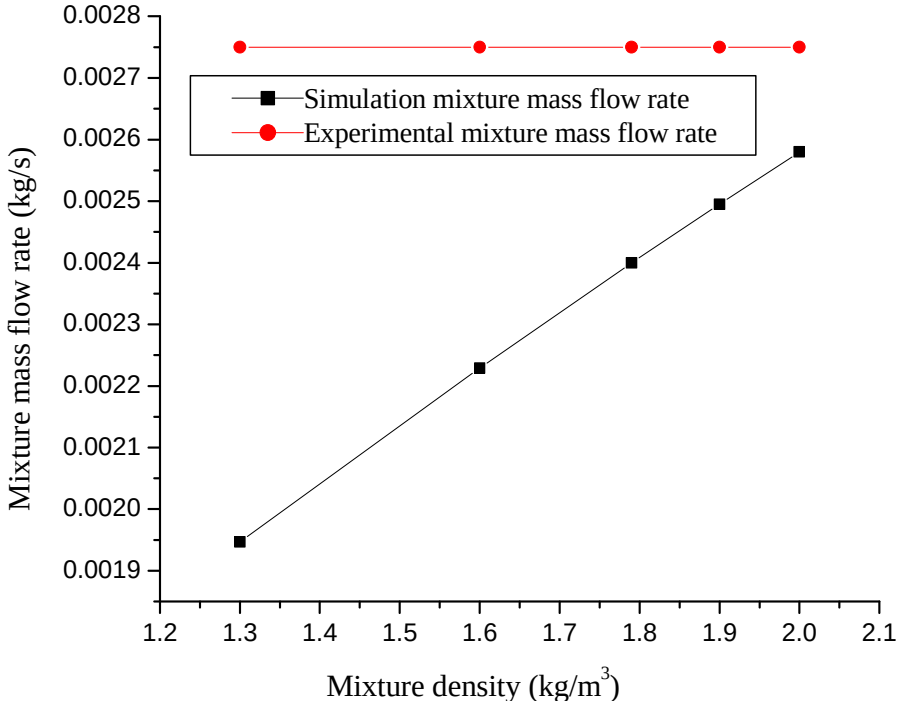

Figure 4.7 Sensitivity of calculations to the mixture density.

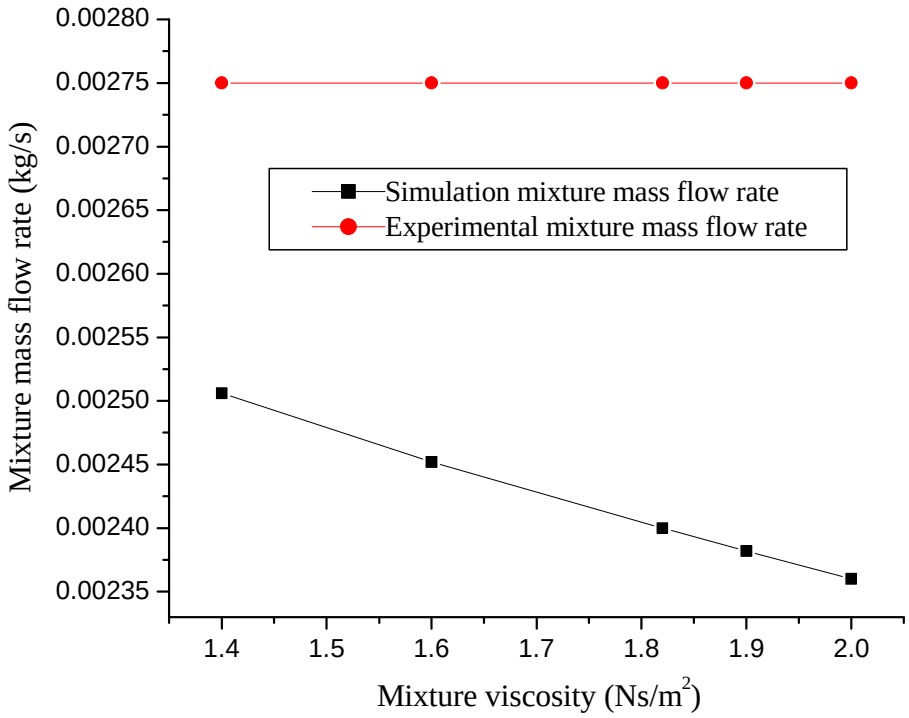

Figure 4.8 Sensitivity of calculations to the mixture viscosity.

4.4.4 Simulation Results and Discussion

The mixture velocity contour and profile, static pressure contour, and profile of the interfacial shear stress are shown in the Figures 4.9 to 4.12. In the contours, the other symmetrical part of the calculation domain is added using the "mirror" function of Fluent®. Figure 4.9 shows the velocity contour of the wave peak region in the gas core. It indicates that the velocity reaches its highest value in the wave peak region. This is because of the contraction of the gas core.

Figure 4.10 shows the velocity profiles in the radial direction at three cross sections in the gas core. The sections are chosen in three different regions: the inlet region (x = 0.01 m), the wave peak region (x = 0.068 m), and the outlet region (x = 0.12 m). All profiles exhibit strong characteristics of turbulent flow. The velocity profiles at

the inlet and outlet regions completely overlap. This agrees well with the periodic boundary conditions as discussed earlier.

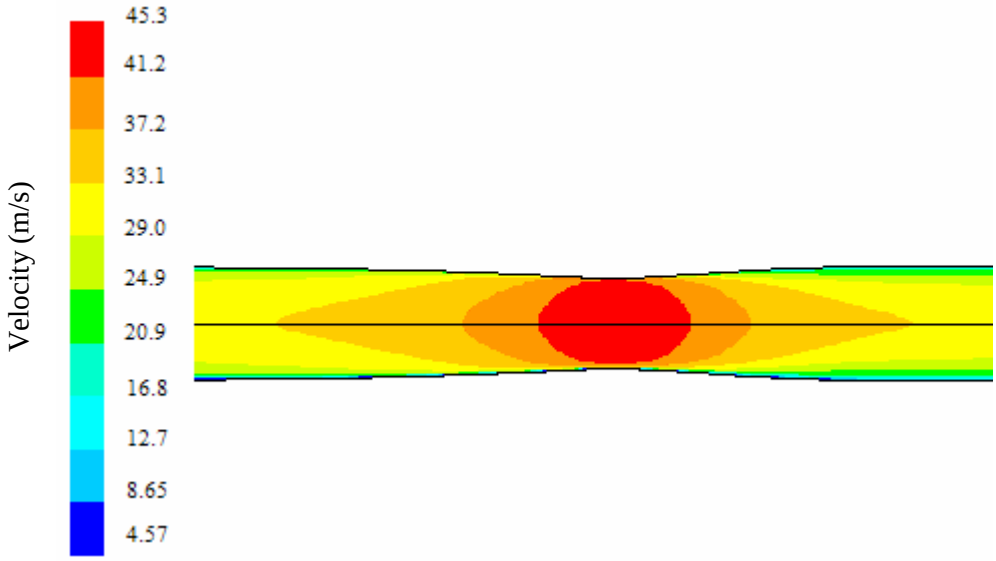

Figure 4.9 Velocity contour of wave peak region in gas core at 1g.

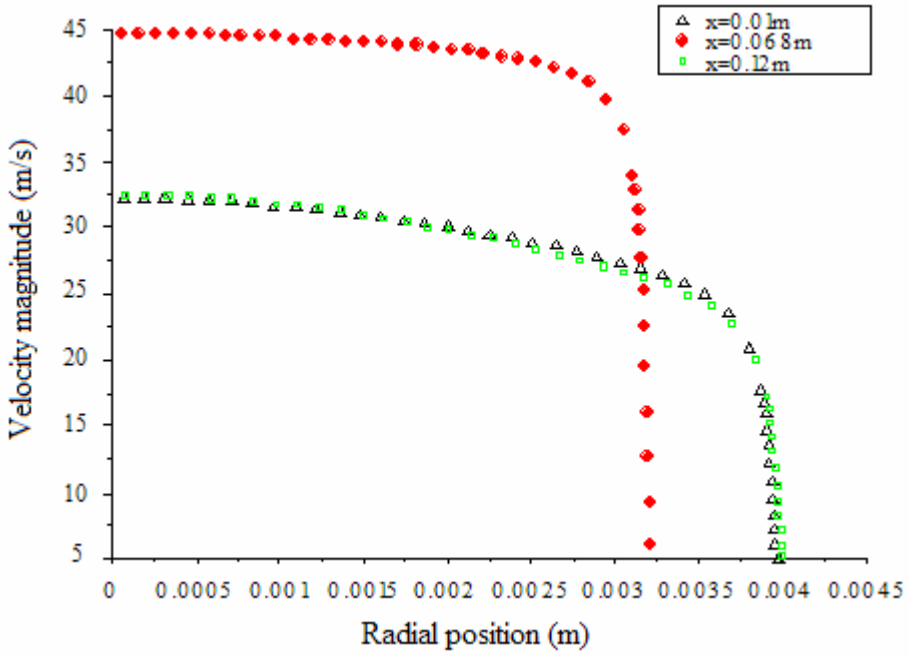

Figure 4.10 Velocity profiles at inlet, outlet, and wave peak region at 1g.

Figure 4.11 demonstrates the static pressure distribution in the wave peak region of the gas core. The values shown in this figure are relative pressure values with the reference pressure being 101.3 kPa. It indicates that the static pressure reaches its lowest values near the wave peak region where fluid flow is relatively faster than all of the other regions. Compared to the nearby regions, the wave peak region acts as a 'pressure sink', which tends to draw in the liquid phase.

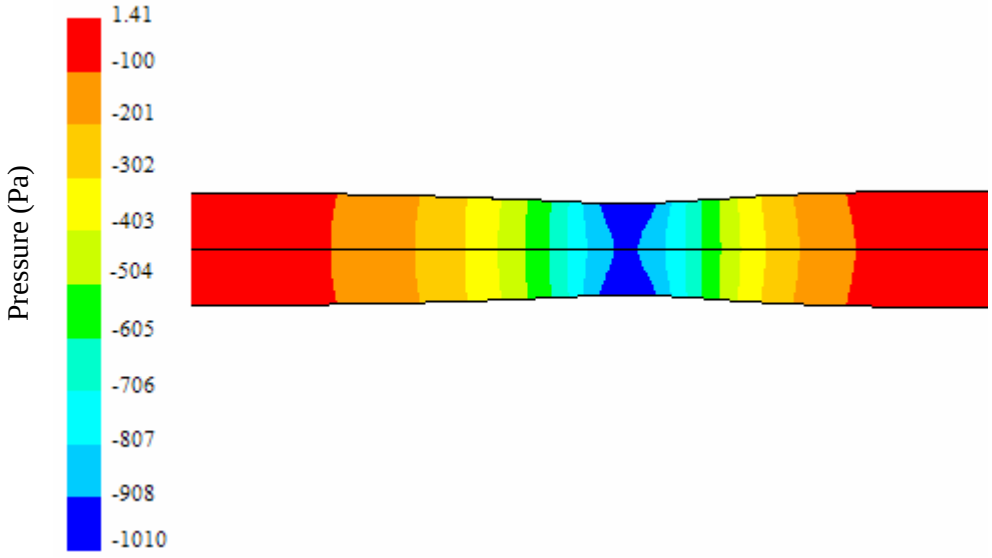

Figure 4.11 Static pressure contour of wave peak region in gas core at 1g.

Figure 4.12 shows the shear stress distribution on the interface. It indicates that the interfacial shear stress in the wave peak region is several times higher than those at all other regions, and that it reaches its maximum value at the location of the wave peak. In conjunction with the velocity contour, it indicates that the flow experiences its largest change in the wave peak region and hence the largest interfacial shear stress.

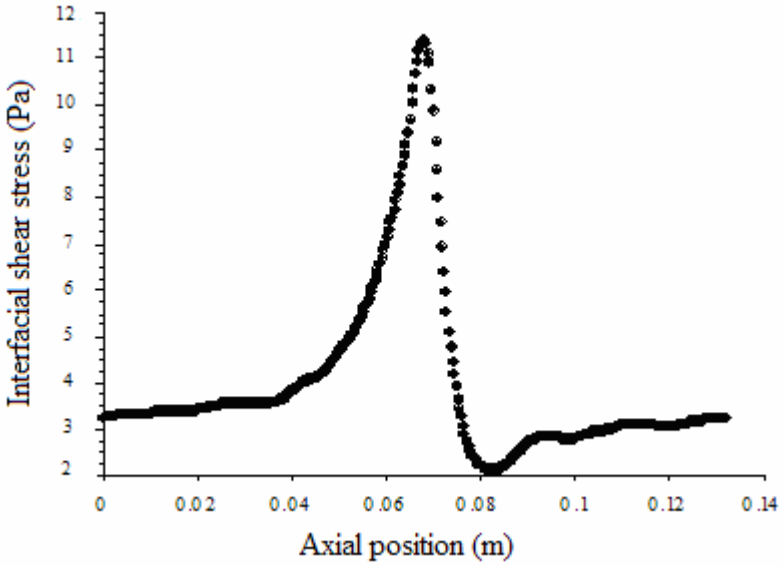

Figure 4.12 Interfacial shear stress distribution at 1g.

4.5 Force Mechanism of Liquid Entrainment

Based on the above simulation results, the force mechanism to trigger the liquid entrainment will now be considered. The most common interpretation of the liquid entrainment mechanism attributes it to the shearing-off of the wave crests of the disturbance waves into the gas core. As noted above, the wave peak region in the gas core is a low pressure region and acts as a “pressure sink”, which tends to draw in the liquid wave and causes it to cave in. The wave peak region also has the largest and acutest interfacial shear stress distribution, which indicates the strongest shearing ability of the region.

Besides the pressure and the interfacial shear stress in the wave peak region, there are another two forces: (a) gravitational force and (b) surface tension force. The role of the surface tension force in the disturbance wave is considered positive since this force prevents the liquid escaping from the body of the wave. On the other hand, the

gravitational force trends to tear some liquid from the wave. Anecdotally, the wave peak region becomes the fiercest “battle ground” for all the forces. Under the action of these forces, the wave peak deforms. During this process, part of the fluid in the wave crest is sheared into the gas core. The above discussion focuses on how the force mechanism triggers the liquid entrainment mechanism. However, it does not explain the details of how the entrainment phenomena occur in annular flow.

As mentioned in Chapter 1, the wave entrainment mechanisms available in the open literature, e.g., wave undercut, wave rolling, wave coalescence, and ripple wave shearing-off entrainment mechanisms, are useful in explaining this process; but none of them has been verified experimentally or otherwise.

4.6 Summary

This chapter presented some of the flow features of the gas core by means of CFD techniques. It started with information on the wave shape and properties at the interface. The present model is axisymmetric and considers the influence of the entrained liquid phase, as it is embodied in the calculations of the physical properties of the mixture in the gas core.

The mixture density is calculated using a new method that assumes homogeneous distribution of the droplets in the gas core. The new method is derived based on the momentum conservation of the entrained liquid phase and gas phase. The RNG k-ε model was used and an enhanced wall treatment method was adopted to deal with the moving wall region. The model was validated for single-phase flow and the

predictions of the model for annular flow compare well with the experimental and analytical results.

A finer mesh was designed to conduct the mesh-independence calculations. The results from the comparisons indicated that the base mesh already produced mesh-independent results. Sensitivity calculations were also conducted to evaluate the effects of the assumptions and parameters in the modeling on the simulation results. Studies showed that (a) the simulation results are moderately affected by the wave position, the pressure gradient, and the mixture density; and (b) the simulation results are insensitive to the wave velocity and the mixture viscosity.

The simulation results in the gas core, e.g., the velocity profiles at different positions, velocity contour at the wave peak region, pressure contour at the wave peak region, and interfacial shear stress distribution were presented and discussed. They showed the turbulent features of the gas core and were strongly influenced by the presence of the waves. In the last section, the force mechanism to trigger the liquid entrainment was interpreted based on the features of the simulation results. The work in this and the previous chapters lays the foundation for the primary objective of the thesis.

CHAPTER 5

ENTRAINMENT FRACTION MEASUREMENTS

5.1 Purpose

This chapter introduces a new method to measure the liquid entrainment fraction in gas-liquid two-phase upward annular flow in a vertical tube (i.d. = 9.525 mm) using a newly-designed separator and a chemically-based titration method. A formula to calculate the entrainment fraction according to the experimental principle is derived. The entrainment fraction data are presented and analyzed. Experiments are conducted at low system pressure (~ 1 atm) and relatively low fluid superficial velocities (V_{sg} = 25.8 m/s to 45.5 m/s, and V_{sl} = 0.15 m/s to 0.30 m/s).

5.2 Experimental Setup and Measurement Techniques

5.2.1 Experimental Loop

A sketch of the experimental loop is shown in Figure 5.1. In the experiments, air and water were supplied at room temperature and near atmospheric pressure conditions. The loop consists of five sections: 1) an air supply section, 2) a water supply section, 3) a test section, 4) a liquid film collecting section, and 5) a liquid droplet collecting

section. In the air supply section, the air flow rate is controlled by a mass flow controller (MKS®, 200 SLM). Air is radially supplied to a mixer, while water is axially injected into the mixer. The water flow rate is controlled by a rotameter (Dwyer® 40GPH). The mixture of air and water concurrently flows upwards into the test section, which is comprised of a vertical 9.525-mm diameter tube and a separator at its end. The

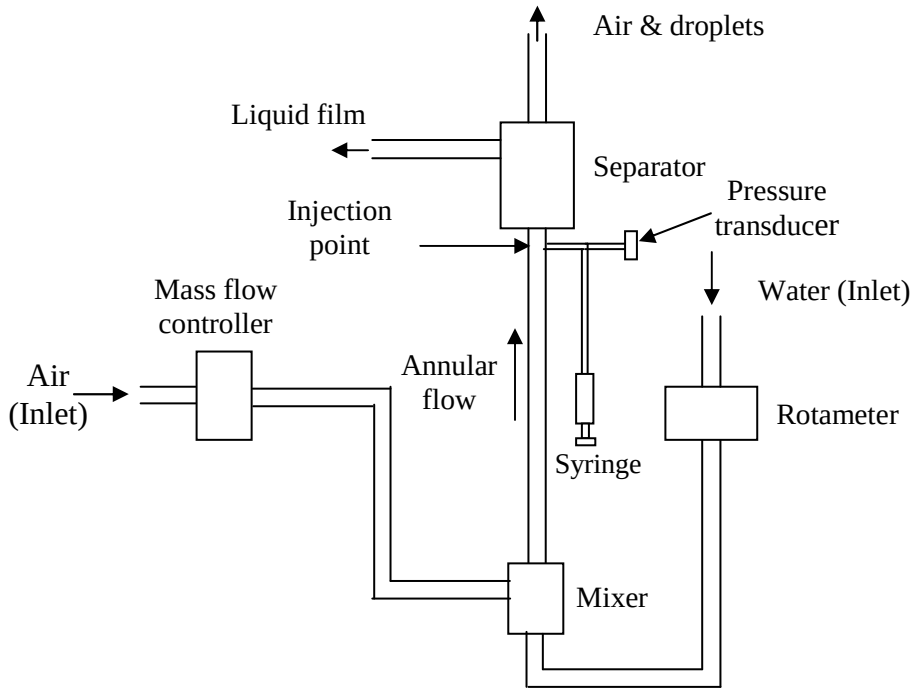

Figure 5.1 Sketch of test loop for entrainment fraction measurement.

separator is designed to capture the droplets from the liquid film. The tube length is 1581 mm (L / D = 166), long enough to guarantee a fully developed annular flow in the test section (the critical ratio of L / D for fully developed annular flow is about 72, Whalley, 1987a). Just below the separator, there is an injection point. It could be used to measure the system pressure with a Validyne® differential pressure transducer, or to inject a dye (or some other solution) into the flow. After separation, the liquid film and

droplets within the gas core are respectively directed into the liquid film collecting section and the droplet collecting section. During the experiments, samples of the liquid film and droplets are collected at the same time at the end of the two collecting sections. At the end of the droplet collecting section, an orifice flow meter (12.5 mm) is used to measure the flow rate in the gas core. The collecting time is recorded using a stopwatch. The samples are weighed using a digital balance. The temperature of the two sample solutions is measured using two glass thermometers, and atmospheric pressure is measured with a mercury manometer.

In this loop, the key component is the liquid-film-and-gas-core separator. The separator and its working principle are introduced in the following sections.

5.2.2 Separator

The separator is the key component of this measurement method. It is used to separate the liquid film and the gas core at the designated location of the test loop. It is schematically shown in Figure 5.2. Its design is based on the hypothesis that annular flow in small-diameter tubes is assumed to be axisymmetric. This greatly simplifies the design of the separator. The separator is comprised of two concentric cylinders with inner diameters of 7.0 mm and 26.0 mm, respectively. The inner and outer cylinders form an annulus that is directly connected to a liquid film collecting tube. The gap between the inner annulus and the inner tube wall is chosen to be 1.26 mm, which is slightly larger than the average film thickness (< 1.0 mm) of all the annular flow cases that were tested. This would allow most of the liquid film to be collected by the liquid film collecting tube. For detailed drawings of the separator, please consult Appendix C.

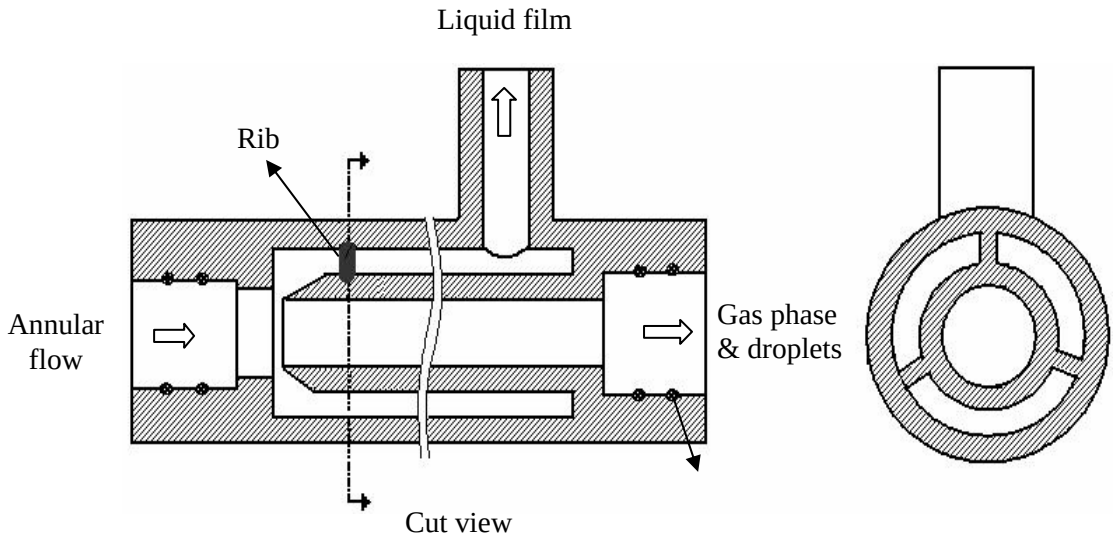

Figure 5.2 Gas-liquid separator; front and side view cross-sections.

In the experiments, when the annular flow passes through the separator, the liquid film is removed from the gas core and directly enters into the annulus between the inner and outer cylinders and is then collected in the film collecting tube. The gas core containing liquid droplets continues flowing upward and directly flows into the inner cylinder. It then flows into the droplet collecting tube which is directly connected to the inner cylinder.

One drawback in this design is the potential that part of the liquid phase carried by the crest of the disturbance waves (whose amplitudes are typically several times larger than that of the average film thickness) is physically sheared into the gas core by the separator itself. This part of the liquid phase is accounted for by using the titration method. The titration method will be introduced next with the derivation of the formula to calculate the liquid entrainment fraction based on the above-mentioned working principle.

5.3 Measurement and Calculation Principles

5.3.1 Calculation Principles and Titration Method

Based on the above descriptions, the ratio of the droplet mass flow rate ($\dot{m}_{TD}$) to the total liquid mass flow rate ($\dot{m}_L + \dot{m}_{TD}$), where $\dot{m}_L$ is the liquid mass flow rate in the film, is equal to that of the droplets sample solution mass (m_{TD}) to the total liquid sample solution mass ($m_{TD} + m_L$). The liquid portion (E_L) in the gas core (after passing through the separator) is expressed as follows

$$E_L = \frac{\dot{m}_{TD}}{\dot{m}_L + \dot{m}_{TD}} \times 100\% = \frac{m_{TD}}{m_{TD} + m_L} \times 100\% . \tag{5.1}$$

However, m_{TD} includes, in addition to the mass of droplets caused by the entrainment mechanism, an estimated portion that is caused by the instrument itself. As mentioned earlier, this is due to the fact that, as annular flow passes through the separator, part of the liquid film is physically sheared into the gas core by the blade of the inner annulus of the separator. This part of liquid (m_S), in addition to the part collected from the entrained droplets (m_D), gives the total m_{TD}, i.e.,

$$m_{TD} = m_D + m_S . \tag{5.2}$$

Equation (5.1) is then transformed to the following form to estimate the actual entrainment fraction

$$E_L = \frac{m_D}{m_{TD} + m_L} \times 100\% + \frac{m_S}{m_{TD} + m_L} \times 100\% . \tag{5.3}$$

Equation (5.3) clearly shows that the source of E_L is made up of two parts: one part comes from the entrained droplets, while the other comes from the sheared liquid caused by the separator. For convenience, the former part is called “droplet entrainment fraction”, or “flow entrainment fraction”, E_D, and the second part is called “entrainment fraction by separator”, E_S. Using E_L as the “total liquid portion” in the gas core, it then can be written as

$$E_L = E_D + E_S . \tag{5.4}$$

In order to determine E_S (or m_s), the titration method is applied. In the experiments, a $CaCl_2$ solution (2 ~ 3 ml) is injected into the liquid film through a port just below the separator within 1 ~ 2 minutes. Because the liquid film is very thin and due to the strong convection and turbulent mixing of the flow, $CaCl_2$ is quickly dispersed evenly in the radial direction in the liquid film. The mass fraction of $CaCl_2$ appearing in the gas core reflects the liquid portion that has been sheared off from the liquid film; therefore,

$$m_S = \dot{m}_L \times \Delta t \times E_{CaCl_2}, \tag{5.5}$$

where $\dot{m}_L$ is the liquid film mass flow rate, Δt is the sample collecting time, and E_{CaCl_2} is the mass fraction of $CaCl_2$ in droplets. E_{CaCl_2} is calculated from

$$E_{CaCl_2} = \frac{m_{CD}}{m_{CD} + m_{CL}} \times 100\%, \tag{5.6}$$

where m_{CD} is the mass of $CaCl_2$ in the droplets sample solution, m_{CL} is the mass of $CaCl_2$ in the liquid film sample solution which is collected simultaneously.

The liquid film mass flow rate at the injection position in the test section can be expressed by the total liquid mass flow rate, $\dot{m}_w$, and the flow entrainment fraction as follows

$$\dot{m}_L = \dot{m}_w (1 - E_D). \tag{5.7}$$

Substituting equation (5.7) into (5.5), the following result is obtained

$$\begin{aligned} m_S &= \dot{m}_w \times \Delta t \times (1 - E_D) \times E_{CaCl_2} \\ &= (m_{TD} + m_L)(1 - E_D) \times E_{CaCl_2}. \end{aligned} \tag{5.8}$$

Now, substitute (5.8) into (5.3), and combine the result with (5.4). The expression for E_D then becomes

$$E_D = \frac{E_L - E_{CaCl_2}}{1 - E_{CaCl_2}}. \tag{5.9}$$

In order to calculate the fraction of $CaCl_2$ in the gas core, the concentration of $CaCl_2$ in the droplets sample solution and in the liquid film sample solution must be first obtained. The titration method is used to estimate the $CaCl_2$ concentration in the two solutions. Once the E_{CaCl2} is calculated, the entrainment fraction in the flow can be then determined from equation (5.9).

Appendix D presents the titration method in some detail and introduces the method of calculating the concentrations of $CaCl_2$ in the liquid film and the droplets sample solutions. The derivation to calculate the E_{CaCl2} from such measurements is also presented in the appendix. The useful formula (see the derivation in Appendix D) is listed as follows

$$C_{CD} = C_{CDS} - C_{CW}, \text{ and } C_{CL} = C_{CLS} - C_{CW}, \tag{5.10}$$

where C_{CD} and C_{CL} are concentrations of titrated $CaCl_2$ in the collected droplet sample solution and liquid film sample solution, respectively; C_{CDS} and C_{CLS} are total concentrations of calcium/magnesium in the two solutions, respectively; and C_{CW} is concentration of original calcium/magnesium in water. Also,

$$E_{CaCl_2} = \frac{m_{TD} C_{CD}}{m_{TD} C_{CD} + m_L C_{CL}} \times 100\%. \tag{5.11}$$

In summary, five variables are measured in the experiments. They are the mass of the sample solution of droplets with sheared film (m_{TD}), the mass of sample solution of liquid film (m_L), the total concentration of calcium/magnesium in the droplets and film solutions (C_{CDS} & C_{CLS}), and the original concentration of calcium/magnesium in water (C_{CW}). Other variables, such as the mass of containers, sample-collecting time, temperature of solutions, and atmosphere pressure, are also measured. Therefore, the entrainment fraction can be determined from equations (5.1), (5.9), and (5.11).

5.3.2 Experimental Procedure

The working principles are introduced above. This section describes the experimental procedures:

1. Measure the mass of the two containers for the collection of the liquid film sample solution and the droplets sample solution. Then, titrate the water samples to obtain the concentration of calcium/magnesium in water.
2. Adjust the air and water flow rates to obtain an annular flow. When the two-phase flow reaches steady state, start to simultaneously collect the droplets and

liquid film sample solutions. Then, slowly inject the $CaCl_2$ solution into the liquid film. After 4 ~ 5 minutes, stop the sample collection.

3. Measure the gas flow rate at the end of the droplet collecting tube with the orifice flow meter.
4. Measure the masses of the sample solutions and titrate them to find the total concentration of calcium/magnesium in both solutions.
5. Wash and dry the containers and repeat the above procedure (steps 2 to 5).

5.3.3 Experimental Errors

Due to the design of the separator (the gap is larger than the average film thickness), part of the gas phase is inevitably removed from the gas core and escapes through the liquid film collecting tube. Furthermore, according to the isokinetic condition analysis (Appendix E) of the operation of the separator in the measurements, pressures on the film side are smaller than those on the gas-core side when the liquid film is separated from the gas core. The imbalance of the pressures in the separator causes more gas phase to escape through the film collecting tube. This fact obviously would have caused droplet losses that must be accounted for. The flow rate of the removed gas phase through the film collecting tube is measured by an orifice meter. Results show that the removed gas flow rate accounts for 11% to 25% of the total supplied gas flow rate in the tested data range. Assuming that the droplets are evenly distributed over the tube cross-sectional area (Barbosa et al., 2002), it is then assumed that the missed droplets are accounted for in the 11% to 25% of the total entrained

droplets. Corrections were made to the calculated entrainment fraction based on the above assumption.

When the separator is installed in the experimental loop, it would undoubtedly disturb the flow. This could reduce the accuracy of the results and measures may have to be used to minimize this condition. Because the liquid film is quickly removed in a short distance, one may argue that the influence on the droplets in the gas core could in fact be neglected.

Analysis (Appendix E) shows that, in the experiments, the isokinetic condition is in fact not achieved. As it turned out in the experiments, the isokinetic condition was not strictly required because of the speed with which the liquid film could be removed at the entrance of the separator. Consequently, one must conclude that the rest of the liquid that is still flowing in the main pass must be in the form of droplets. However, this requires that the film removal length must be small enough to ensure that no atomization occurs. The separator was designed with this in mind.

5.4 Results and Discussion

In the experiments, the range of velocities of water and air is set as follows: air superficial velocity, V_{sg}, 25.8 m/s ~ 45.5 m/s; and water superficial velocity, V_{sl}, 0.15 m/s ~ 0.30 m/s. The system pressure ranges from 0.98 atm ~ 1.1 atm. This range corresponds to the one used in prior experimental work that were conducted earlier to obtain film thickness at variable gravity levels.

Figure 5.3 shows the results of the liquid portion in the gas core (E_L), the flow entrainment fraction (E_D), and the entrainment fraction by separator (E_S) at a gas

superficial velocity of 35.8 m/s, and liquid velocity ranging from 0.15 m/s to 0.30 m/s. It can be seen that, for these flow velocities, the portion of the liquid phase sheared into the gas core by the separator is larger than that entrained by annular flow due to the interaction of the two phases. This indicates that the newly devised instrument could cause relatively large disturbances to the flow. However, the advantage of this new method is that disturbances to the flow can be quantified. This is not the case with the other two methods mentioned earlier (the liquid film withdrawal and the sampling probe methods).

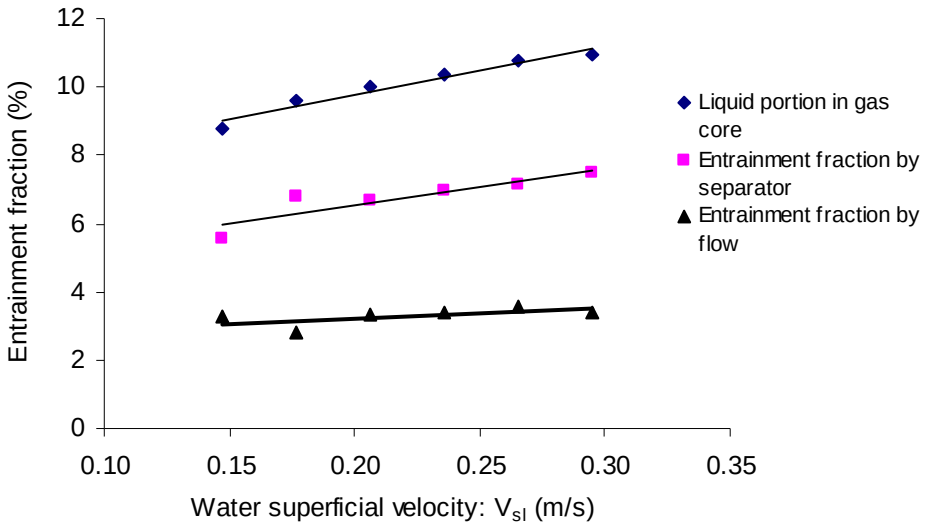

Figure 5.3 Liquid entrainment fraction; V_{sg} = 35.8 m/s.

Figure 5.4 shows the results of the flow entrainment fraction at different gas and liquid superficial velocities. From the figure, it can be seen that increasing the velocity of either phase leads to the increase of the entrainment fraction. In the tested data range, liquid entrainment fraction is measured to be in the range of 1.7% to 7.0%. These small values indicate that liquid entrainment is just beginning for the gas and liquid velocities tested. The data are shown in Appendix F.

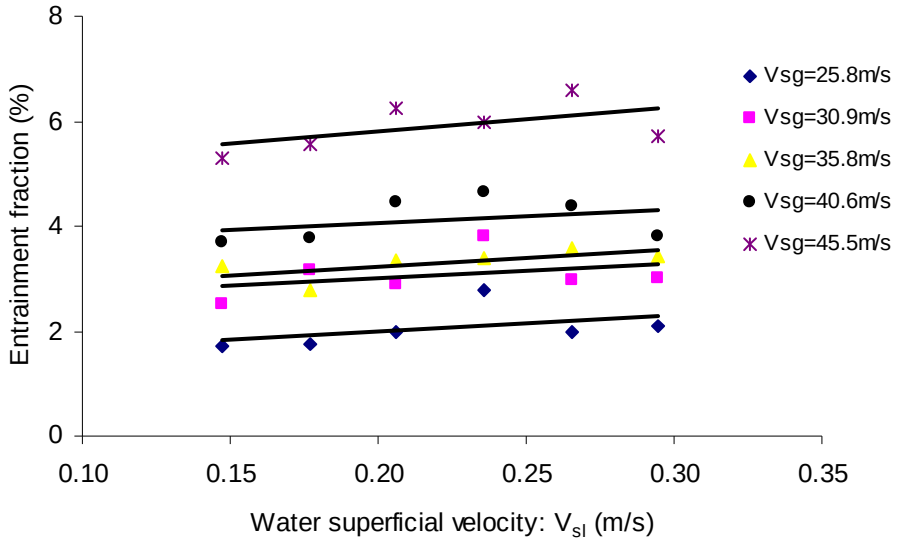

Figure 5.4 Entrainment fraction at different gas and liquid superficial velocities.

Figure 5.5 shows the influence of the injection method on the entrainment fraction. In one of the injection methods, the air is injected radially while the water flows axially into the mixer. In the other method, the gas is injected axially and the water flows radially. The corresponding entrainment fraction data at two different gas superficial velocities are presented and compared. The results indicate that when the flow is fully developed, the injection method has little or no influence on the measurements. This result agrees well with previous findings reported by investigators such as Hutchinson et al. (1974).

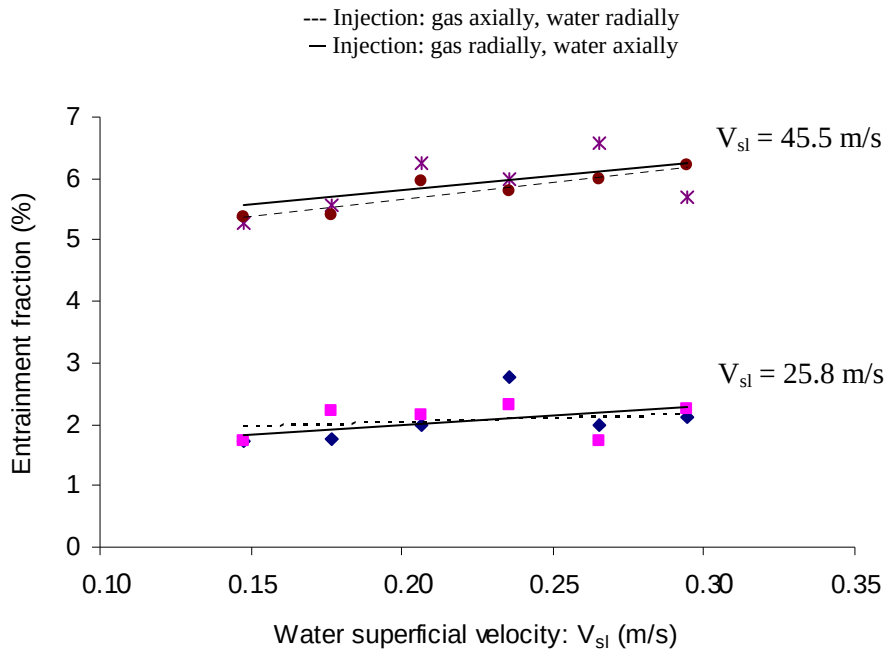

Figure 5.5 Influence of injection method on entrainment fraction.

In order to examine the performance of the new technique, the experimental results using the new method are compared to the results using the film removal technique commonly used by other investigators (e.g., Cousins and Hewitt, 1968; Jepson et al, 1989). The comparisons are made for similar experimental conditions. The gas and liquid mass fluxes and pipe inner diameters are similar, while the system pressure varies from 1 to 2 atm. The results, including the present experiments, are summarized in Table 5.1.

Table 5.1 Comparison of experimental conditions

Investigators	D, mm	P, atm	G_g, kg/m^{2}s	G_l, kg/m^{2}s	E, %	Fluid	Method
Cousins and Hewitt (1968)	9.525	2	71-124	88- 178	7 ~ 31	Air - water	Film removal method
Jepson et al. (1989)	10.26	1.5	40-120	40-140	1 ~ 25		
Present work	9.525	1	31-56	147-295	1~ 7		New method

The results of these comparisons are shown in Figures 5.6 and 5.7. It can be seen that the experimental data of both studies (Cousins and Hewitt, 1968 and Jepson et al., 1989) follow the same trend as the present data. This verifies that the new technique to

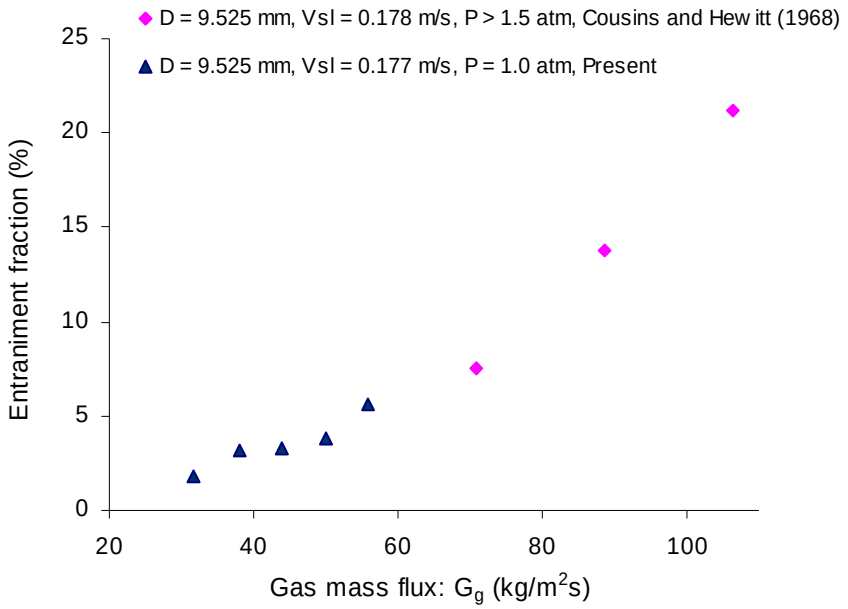

Figure 5.6 Comparison with results of Cousins and Hewitt (1968).

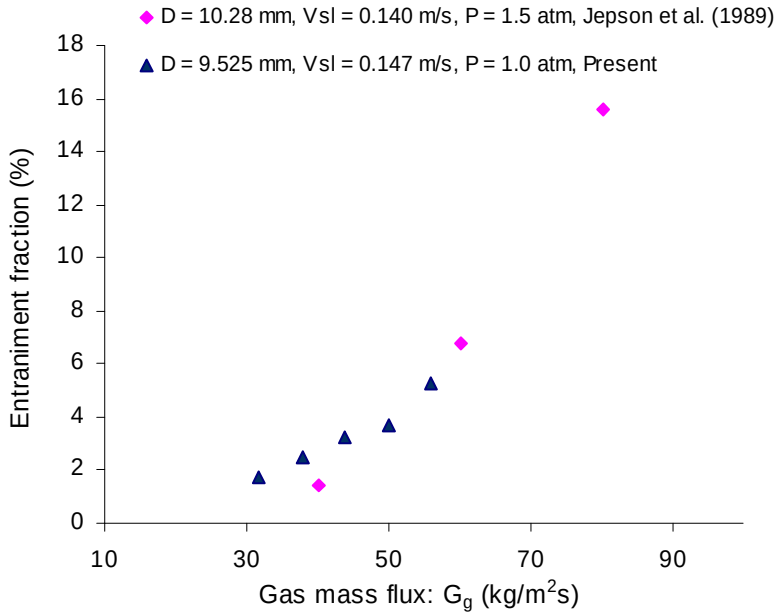

Figure 5.7 Comparison with results of Jepson et al. (1989).

measure the entrainment fraction can perform as well as the film removal technique. Figures 5.6 and 5.7 also show that most of the other researchers' data fall in an entrainment range larger than that of the present data. So far, the author has found very few entrainment data sets that are lower than 5%. One possible reason is that it is difficult to measure such low entrainment fraction using the sampling probe or the film removal methods. Figures 5.6 and 5.7 also suggest that low entrainment fraction can be satisfactorily measured using the new method.

Because there is no standard or reference for entrainment fraction measurements using this technique, each instrument is calibrated separately. Also, repeatability tests are performed to ensure the reliability of the proposed method. The repeatability tests are performed at the same flow settings covering the complete liquid flow rate range. While the gas flow rates are arbitrarily selected, each flow setting at lower and higher gas flow rate was repeated at two separate set points and the results are shown in Figure 5.8. It is clear that the data are very repeatable. The data indicate that the maximum absolute difference is within 0.3% of the entrainment fraction.

The method to calculate the experimental uncertainty in the measurements is that of Coleman and Steele (1999). For every measurement, there is a systematic uncertainty, B_i, and a random uncertainty, P_i. The total uncertainty of a measurement, U_i, is the root-sum-square of the components of uncertainty,

$$U_i = (B_i^2 + P_i^2)^{1/2}. \tag{5.12}$$

Both the systematic and the random uncertainties are also calculated using the root-sum-square method to combine the components.

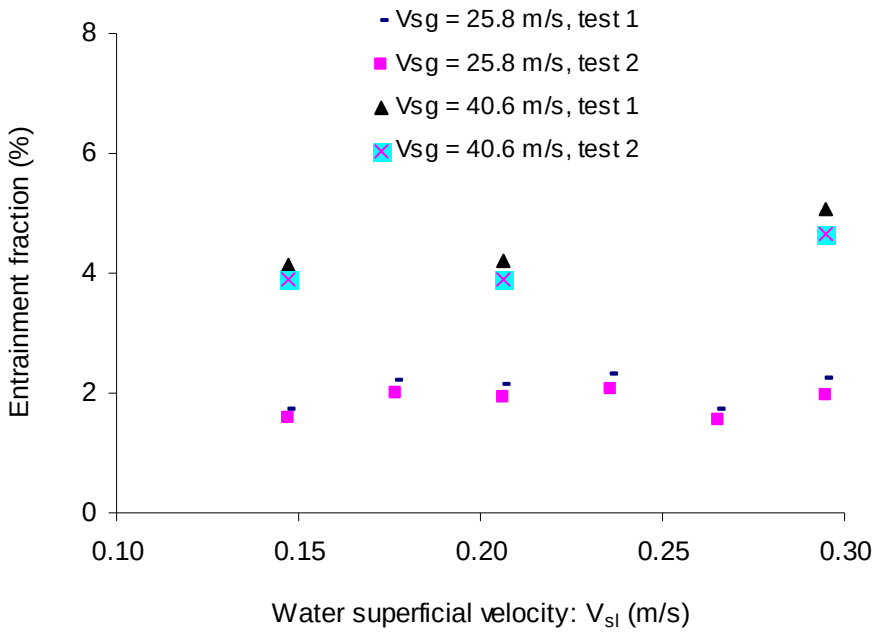

Figure 5.8 Comparisons of the results of repeatability tests.

The following parameters are mainly considered in the calculations of the uncertainty: the mass of droplet solution, the mass of liquid film solution, the mass of the two containers for solution collections, the EDTA amount to titrate water, the EDTA amount to titrate droplets solution, and the EDTA amount to titrate the liquid film solution. The details of the analysis and calculations of the experimental uncertainty are presented in Appendix F. Calculations show that the maximum uncertainty of the entrainment fraction at different gas superficial velocities is estimated to be 0.26% in the present range of data. Figure 5.9 shows the experimental data with error bars.

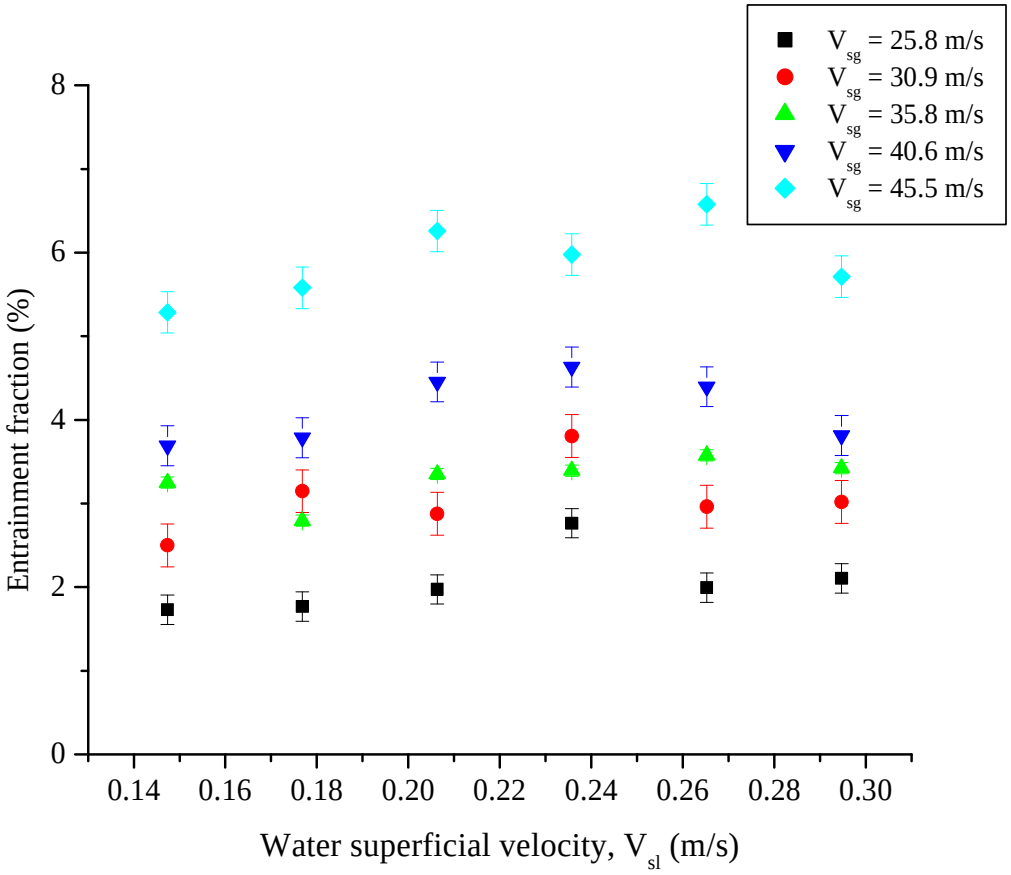

Figure 5.9 Entrainment fraction data with error bars.

5.5 Summary

A gas-liquid separator was designed, in conjunction with the chemically-based titration method, and was used to effectively measure the liquid entrainment fraction in annular flow. The entrainment fraction data showed consistent trends in that the fraction increases with the increase of both the liquid and gas flow rates. Also the injection method had little or no influence on the results for fully developed annular flow. Results also showed that the entrainment fraction was less than 7% over the range of liquid and gas mass fluxes with a maximum uncertainty of 0.26%. The low entrainment fraction

data indicate that wave entrainments are barely initiated in the annular flow at these conditions.

Comparisons with other entrainment data collected using the liquid film removal method indicated that the new technique can perform as well as the film removal technique (which is currently believed to be the only accurate method for small-diameter tube measurement). The comparisons also indicated that the new technique is applicable to lower entrainment fraction data measurements. Repeatability of test results verified that the new technique produced reliable, consistent, and repeatable data.

CHAPTER 6

SIMULATION II: LIQUID ENTRAINMENT MECHANISM

6.1 Purpose

Due to the chaotic nature of the gas-liquid interface in annular flow, limited space for employing accurate measuring devices, and the rather complicated mechanism of liquid entrainment, experimental methods provide limited information on such mechanisms. In this chapter, CFD techniques are employed to improve the understanding of the liquid entrainment mechanism and, in particular, to show how the interfacial waves are involved in the entrainment process.

6.2 Modeling

6.2.1 Model Description

Based on previous discussion, the gas core of annular flow in this study is in the turbulent state while the liquid film has strong features of the near-wall flow. The RNG k-ε model, employing a scheme to consider the near-wall flow effects, is used in the simulation. The enhanced wall treatment method is used to deal with the near-wall region of the flow. In order to reconstruct the gas-liquid interface of annular flow, the

geometric reconstruction scheme of VOF model is adopted. Chapter 2 contains the details of these models and provides the reasons for adopting them in the simulation. Due to the flow axisymmetry, a two-dimensional model is constructed. Unlike the previous simulation (Simulation I), the model in this simulation is a transient model.

Fluent® 6.18, is used as the solution tool. For the model, the package uses a segregated solver that solved the governing equations sequentially, and implicit discretization schemes for the momentum, k, and ε transport equations. However, the package uses an explicit time-marching scheme to solve the time-dependent continuity equations for the volume of fractions. In the modeling, the surface tension is included and its value is set to that of the air-water surface tension, i.e., 0.072 N/m. Some other information on the model configuration is listed in Table 6.1. The convergence criterion is set such that the residuals of all the variables are $\leq 10^{-3}$.

Table 6.1 Summary of the model configuration

Item		Model configuration
Phases in VOF model	Air	Primary phase
	Water	Secondary phase
Relaxation factors for all variables		1.0
Discretization schemes of convective terms in governing equations	Pressure	Body force weighted
	Pressure-velocity coupling	PISO
	Momentum equation	First order upwind
	Turbulent kinetic energy	First order upwind
	Turbulence dissipation rate	First order upwind

As shown in Table 6.1, air is set as the primary phase and water is the secondary phase. In Fluent®, the results are not affected by the selection of which phase is chosen

as the primary phase. The only difference is the solution methods for their volume fractions.

6.2.2 Simulation Domain

The simulation domain is shown in Figure 6.1. Only half of the tube domain is simulated since the flow is axisymmetric. The simulation domain is bounded by the tube wall, tube axis, and the tube inlet and outlet sections. Air and water enter the inlet section with the air inlet radius set to 4.2 mm; the water annulus width at the inlet section is set to 0.5625 mm. These values are chosen based on the range of measured liquid film thickness in channel of 9.525 mm inside diameter. In the simulation, the tube length is set to 500 mm, shorter than the actual length. This length is chosen because it can satisfy the simulation objective with a minimum computational cost.

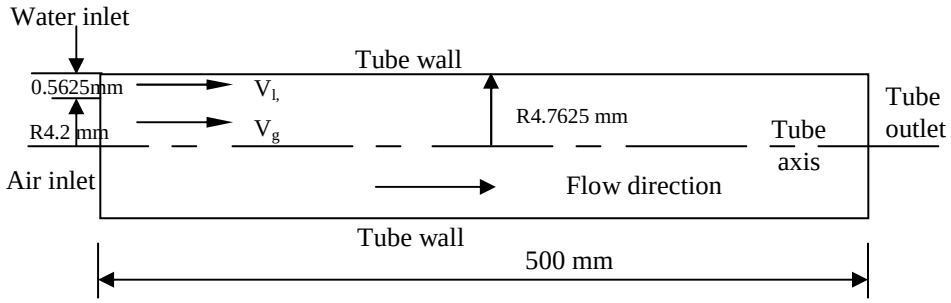

Figure 6.1 A schematic of the simulation domain.

6.2.3 Boundary and Initial Conditions

Boundary conditions: As shown earlier in the experimental study, water is supplied through the tube's inlet at a constant velocity, V_l. In the simulation, the water

velocity ranges from 0.7 m/s to 1.1 m/s, corresponding to the actual measured liquid velocity. The volume fraction of water at the inlet was set to “1”, meaning only water is flowing at the water annulus inlet section. As to the turbulence boundary conditions, the turbulence intensity and hydraulic diameter are used as the turbulence specification. The turbulence intensity, I, is defined as the ratio of the root-mean-square of the velocity fluctuations, u', to the mean flow velocity u, i.e., $I = u' / u$. Commonly, for low turbulent flow, $I \leq 1$ %; and for high turbulent flow, $I > 10$ %. This principle is used to estimate the turbulence intensity at the inlet. Because in this study the liquid film of annular flow has the features of near-wall flow, a low value for I is appropriate in the simulation. At the water inlet, the turbulence intensity of the water is set in a range of 0.2 % ~ 1.2 %, corresponding to the different water inlet velocities. The hydraulic diameter is kept the same as the width of the water annulus inlet (0.5625 mm).

Air is supplied through the gas portion of the inlet section at a constant velocity, V_g, as shown in Figure 6.1. In the simulation, V_g ranges from 0.5 m/s to 15 m/s, which is in fact lower than the actual measured gas velocity. This arrangement is mainly to save on computational time and the potential liquid flow breakdown at higher gas velocities (the latter consideration will be addressed at some length in the following section). The volume fraction of water at this portion of the inlet was set to “0”, meaning no water flow. As to the turbulence boundary conditions, the turbulence intensity of the air was set in the range from 1 % to 10 % corresponding to various air velocities. The hydraulic diameter remains the same as the diameter of the air inlet section of 8.4 mm. The boundary conditions at the tube inlet are summarized in Table 6.2.

Table 6.2 Boundary conditions at tube inlet (air and water inlets)

Boundary condition		Water inlet	Air inlet
Constant velocity inlet (m/s)		0.7 ~ 1.1	0.5 ~ 15
Turbulence specification	Turbulence intensity (%)	0.2 ~ 1.2	1 ~ 10
	Hydraulic diameter (mm)	0.5625	8.4
Volume fraction of secondary phase (water)		"1" (with water flow)	"0" (no water flow)

A no-slip boundary condition is assumed at the tube wall. The flow is axisymmetric with the gradient of all the variables about the axis being zero, i.e., $\partial\phi/\partial r = 0$ (ϕ = velocity, k, or ε). An outflow boundary condition is assumed at the tube outlet.

Initial conditions: The initial conditions in the simulation are the same as those in the experiments. At t = 0 s, the tube is full of air. This means the volume fraction of the secondary phase, i.e., water, is zero everywhere in the tube. The initial pressure in the tube is 1 atm. As far as the velocities, both radial and axial velocities in the tube are set to 0 m/s at t = 0 s. The same applies to the initial k and ε values.

6.2.4 Phase Properties

The air and water properties are listed in Table 6.3.

Table 6.3 Phase properties

Phase	Density (kg/m^3)	Viscosity ($kg/(m \cdot s)$)
Air	1.23	1.8×10^{-5}
Water	1000	10^{-3}

6.2.5 Simulation Considerations

Additional considerations are addressed here dealing with the effects of changing the gravity level, the mesh size and the time step in the simulation.

Gravity level: The gravity level is an important factor that could strongly influences the two-phase flow behavior. Gravity has a de-stabilizing effect on the flow. At a starting point in this simulation, the gravity is set to zero. It will be considered later when its role in disturbing the flow is discussed.

Mesh size: The mesh size contributes to the computational time and the accuracy of the results. A finer mesh has the potential to improve the accuracy of the simulation results, but this improvement comes in many cases at the expense of computational time. A balance between the accuracy of the results and the cost should be always sought. The mesh size, shown in Table 6.4, used for this research attempts to meet this principle. A quadrilateral mesh is used for this simulation.

Table 6.4 Mesh size for the simulations

Mesh size (mm)			Mesh node numbers		Domain dimensions (mm)	
Δr_{max}	Δr_{min}	Δx	Tube radius	Tube length	Tube radius	Tube length
0.476	0.138	5	20	101	4.7625	500

In Table 6.4, Δr_{max} and Δr_{min} are the maximum and minimum mesh sizes in the radial direction, respectively; and Δx is the mesh size in the axial direction. In addition, 20 mesh nodes are arranged on the tube radius and 101 nodes on the tube axis or tube wall.

The mesh is evenly distributed in the axial direction while an uneven distribution of the mesh is used in the radial direction in such a way as to satisfy the goals of the simulation. It has been suggested earlier in Chapter 2 that the near-wall region of the flow needs a finer mesh than the other regions due to the acute changes of the flow variables in that region. Another consideration in the simulation is that it is

known that the wave-induced entrainment phenomenon occurs on the gas-liquid interface. This also requires a finer mesh near the tube wall region in order to capture the features of this process in the simulation. Therefore, in this research, the mesh distribution in the radial direction is designed in such a way that the mesh is fine near the wall but as it gets closer to the tube axis, it becomes coarser. Figure 6.2 shows an enlarged view of the mesh near the inlet region.

Using the mesh size of Table 6.4 as the "base" mesh, some finer and coarser meshes were also designed to test the mesh's influence on the simulation results. The results will be presented later.

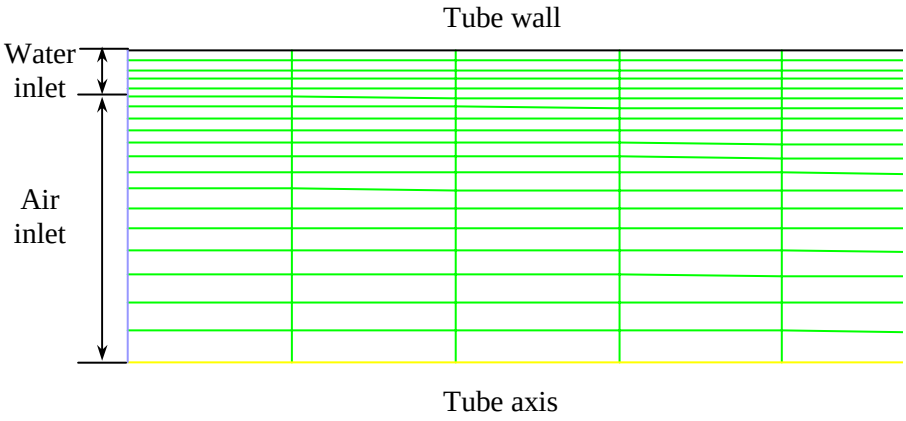

Figure 6.2 Mesh characteristics at the inlet region.

Time step: Fluent® used explicit time-marching scheme to solve the time-dependent continuity equations for the volume fraction. In order to ensure the stability of the explicit discretization scheme, the time step must meet some restrictions: the smallest grid size and the maximum phase velocity determine the maximum time step in the model. Their relationship can be expressed by the Courant number as described by equation (2.15). Equation (2.15) can be transformed into another form

$$\frac{\Delta t \cdot V_{max,fluid}}{\Delta x_{min,cell}}. \tag{6.1}$$

The meaning of the Courant number can be seen more clearly from Equation (6.1): it is the ratio of the maximum distance that the fluid could transit within one time step to the minimum mesh size in the flow direction. Therefore, in order to accurately simulate the entire flow information, Courant number must satisfy the following requirement

$$\frac{\Delta t \cdot V_{max,fluid}}{\Delta x_{min,cell}} \leq 1.0. \tag{6.2}$$

The time step that makes the Courant number equal to 1.0 is the maximum time step for the established mesh. In each simulation, the corresponding maximum time step according to Equation (6.2) is used for most of the time-marching schemes except for the volume fraction calculation.

The time step used for the volume fraction calculation is not the same as the one used for the rest of the transport equations. Instead, Fluent® uses a more refined time step based on a default Courant number (0.25), which is small enough to ensure the stability of the explicit scheme of the volume fraction as well as to provide physically realistic simulation results.

In the simulation, the gas phase has a maximum velocity which changes from time to time with the evolution of the two-phase interface. According to the Courant number, the time steps for the time-marching schemes are changing accordingly. For example, once a wave is generated on the interface, the maximum gas velocity will increase due to the contraction of the gas core near the wave peak region, and the time step should be refined accordingly. This adjustment of the time step is manual.

The initial time step, Δt_0, is calculated based on the gas inlet velocity. Δt_0 is the time step that works throughout the whole simulation if a smooth interface is generated between the two phases. In the simulation, the initial time step is soon substituted by a smaller one as the interface evolves.

6.3 Simulation Process

6.3.1 Step 1: Attaining Annular Flow

The main objective of the study is to explore the liquid entrainment mechanism in annular flow. Based on the mesh described above, two annular flow cases, as shown in Table 6.5, are simulated and their results are presented and discussed. Case I with the lower gas velocity is considered as the "base" case. It is also used to make the parametric study. This arrangement is based on the following considerations: (1) the time step is optimum for the base case; (2) the base case produces a reasonable liquid-film thickness that does not frequently collapse (if much higher gas velocities similar to those used in the experimental conditions were adopted, the liquid film would be much thinner and would frequently collapse); and (3) under the conditions of Case I, the modelled tube length is long enough for the simulation to allow the liquid entrainment phenomena in fully developed annular flow in the tube.

Table 6.5 Annular flow cases for Simulation II

Cases	V_l (m/s)	V_g (m/s)	Flow regime
Case I	1	6	Annular flow
Case II	1	15	Annular flow

6.3.2 Step 2: Defining the Simulation Domain

In the simulation, water is supplied from the water inlet and air from the air inlet. As time elapses, the liquid phase gradually covers the whole tube wall. For the base case, over one second is needed to develop a complete liquid film covering the tube wall, while less time is needed for Case II to develop a whole liquid film due to its high gas velocity. Then, the flow in the tube becomes predictable and repeatable. The analysis in this chapter is made on the simulation results from the stable stage of the flow. A general description of the simulation results is given below.

The simulated annular two-phase flow can be divided into two regions: a smooth region and a wavy region. In the first region, which starts at the tube inlet, the gas-liquid interface is very smooth and the velocities of the two phases are strongly influenced by their initial inlet values. The smooth region is short compared to the whole tube length. The faster the inlet velocities, the longer is the smooth region. In the wavy region, the two-phase interface is covered by waves. At the beginning of this region (transitional wavy region), the interface becomes slightly wavy and the two-phase velocities are still affected by the inlet velocities. Not until after some length (about 1/4 ~ 1/3 of the tube length for Case I), do the waves grow and the two-phase velocity profiles become fully developed. At this stage, liquid entrainment is observed in the simulation.

Some simulation images are presented to show this feature of the simulation results. In these figures, the entire annular flow is presented by means of utilizing the “mirror” function in Fluent®, although only one-half of the domain is simulated. In the figures, the dark color represents the liquid phase while the grey color represents the gas phase. The axial solid line in the flow of each figure represents the tube axis. The radial

solid line in the flow is the marking line produced by Fluent® and is used to locate the flow in the tube.

Figure 6.3 presents the results in the enlarged tube inlet region that contains the smooth region and the starting of the wavy region of annular flow. In the figure, x = 0 mm marks the tube inlet position. Figure 6.3 (A) shows that the first wave is generated at about x = 7 mm and for the higher gas velocity case (B), this distance is 9 mm.

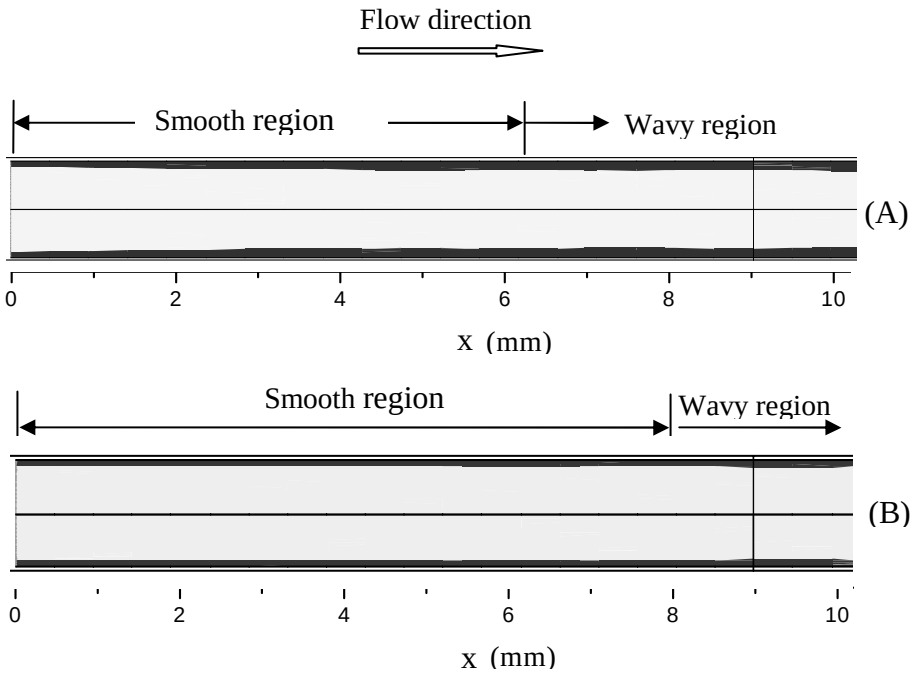

Figure 6.3 Simulation results: (A) Case I (V_g = 6 m/s; V_l = 1 m/s) at t = 2.113 s; and (B) Case II (V_g = 15 m/s; V_l = 1 m/s) at t = 3.1779 s.

Figure 6.4 shows the velocity profiles of the two phases in the smooth and wavy regions for Case I. In the figure, R = 0 mm indicates the tube axis position while, R = 4.7625 mm indicates the tube wall position. Each velocity profile consists of two distinct parts: the first part has a relatively high velocity and represents the gas velocity in the core; the second part has a much lower velocity and represents the liquid velocity

profile in the liquid film. Figure 6.4 shows the velocity profiles at axial positions of x = 1, 6, and 190 mm. The results clearly show that the profiles are a strong function of the inlet velocity and the relative position in the smooth region (x = 1 mm). The velocity profile at x = 6 mm in the transitional wavy region indicates a transitional profile to a fully developed one (profile at x = 190 mm) in the fully-developed wavy region.

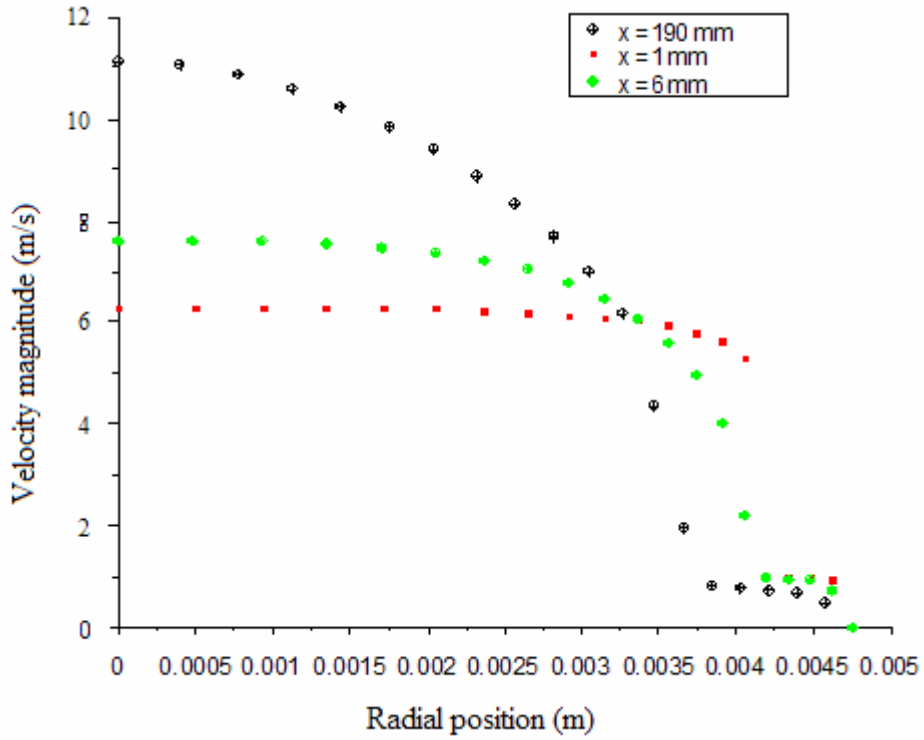

Figure 6.4 Velocity profiles of the two phases in the smooth and wavy regions of Case I (V_g = 6 m/s; V_l = 1 m/s) at t = 2.113 s.

Figure 6.5 shows part of the enlarged wavy region. It can be seen that the interface is completely covered by waves with various shapes and at some point downstream, the liquid phase is sheared off from the wave crest into the gas core.

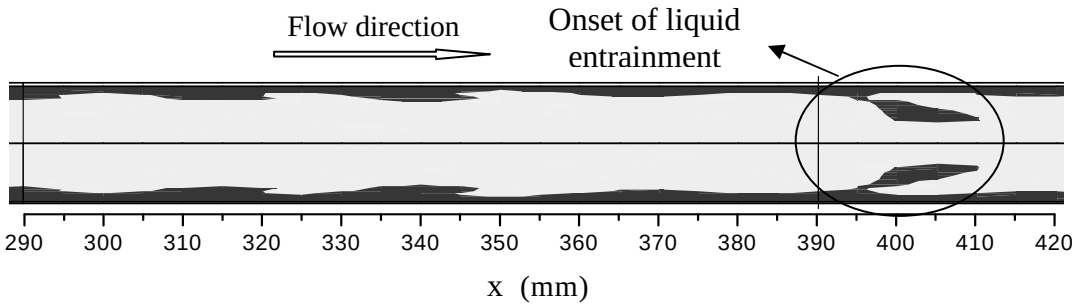

Figure 6.5 Simulation results in the wavy region of Case I (V_g = 6 m/s; V_l = 1 m/s) at t = 2.163 s.

6.3.3 Step 3: Simulation of the Waves on the Interface

The main purpose of this simulation is to explore the liquid entrainment mechanism in annular flow. However, due to the waves' role in the entrainment mechanism, they need to be considered. In the simulation, the waves are generated on the interface by means of the VOF model (to be further discussed in the following chapter). Figure 6.6 shows an individual wave in the fully-developed wavy region where the inlet velocities no longer exert an influence on the velocity profiles of the two phases.

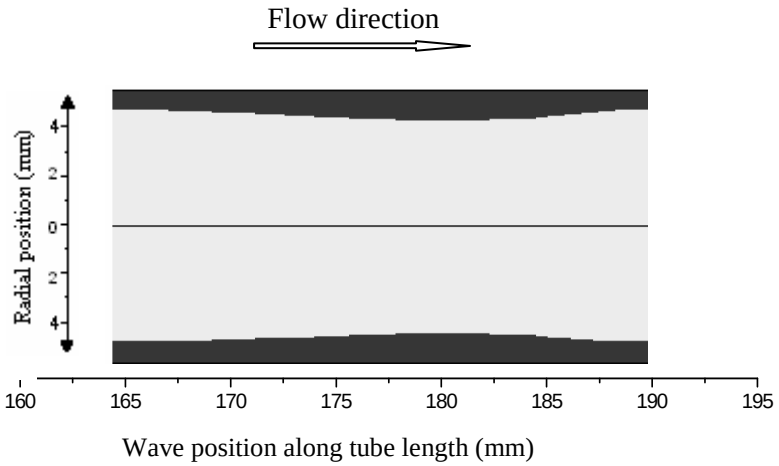

Figure 6.6 Wave shape and dimensions in the fully developed region; Case I (V_g = 6 m/s; V_l = 1 m/s) at t = 2.163 s.

6.3.4 Step 4: Mesh Independence

The work in this section is to examine if the simulation results are mesh-independent. Three meshes were compared to the base mesh (or standard mesh); two coarser and one finer. The number of nodes in both the radial and axial directions is increased for the finer mesh and decreased for the coarser meshes, as shown in Table 6.6. It should be noted that the numbers of the nodes in the table correspond to one half domain of the tube. All other model settings are the same as for the base case.

Table 6.6 Meshes for mesh-independence calculations

Mesh	Nodes in radial direction	Nodes in axial direction	Total nodes
Standard mesh	20	101	2,020
Finer mesh	21	106	2,226
Coarser mesh I	19	81	1,539
Coarser mesh II	17	73	1,241

The models with the additional meshes have been solved and the results are compared with those of the standard mesh. The comparisons are made in three ways: (1) comparison of the wave images; (2) comparison on the wave parameters; i.e., wavelength and wave height comparisons; and (3) comparison of velocity profiles at the wave crest at a certain position of the tube.

Comparison of the wave images: The wave images around a position of x = 190 mm for each mesh are shown in Figures 6.7, 6.8, and 6.9. They are compared to the wave image of the standard mesh as shown earlier in Figure 6.6. It can be seen that all the wave images from these meshes are similar.

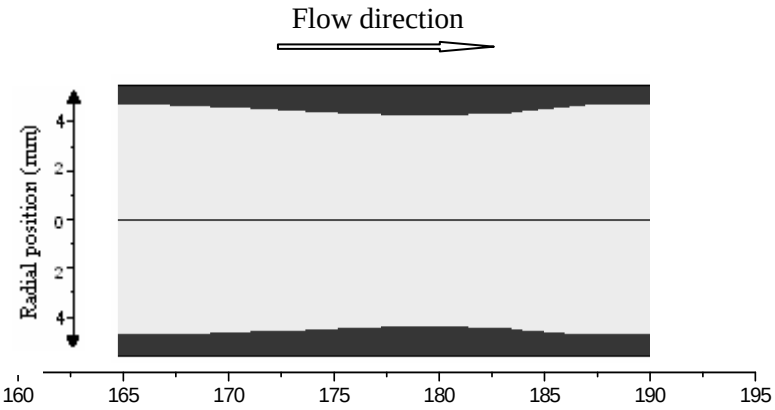

Figure 6.7 Wave shape and dimensions of the finer mesh (V_g = 6 m/s; V_l = 1 m/s) at t = 2.163 s.

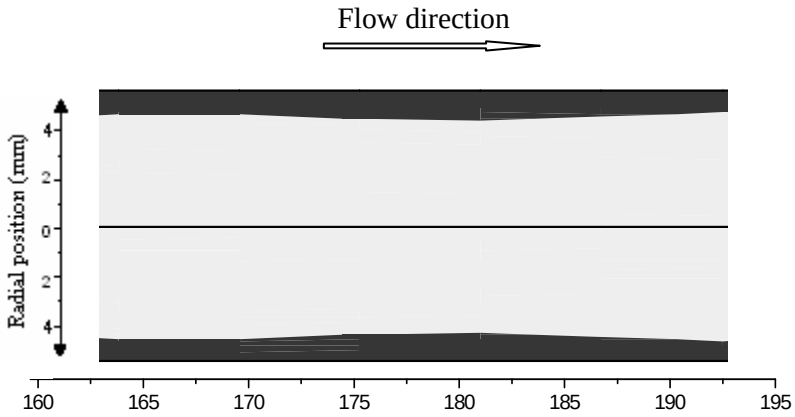

Figure 6.8 Wave shape and dimensions of the coarser mesh I (V_g = 6 m/s; V_l = 1m/s) at t = 2.163 s.

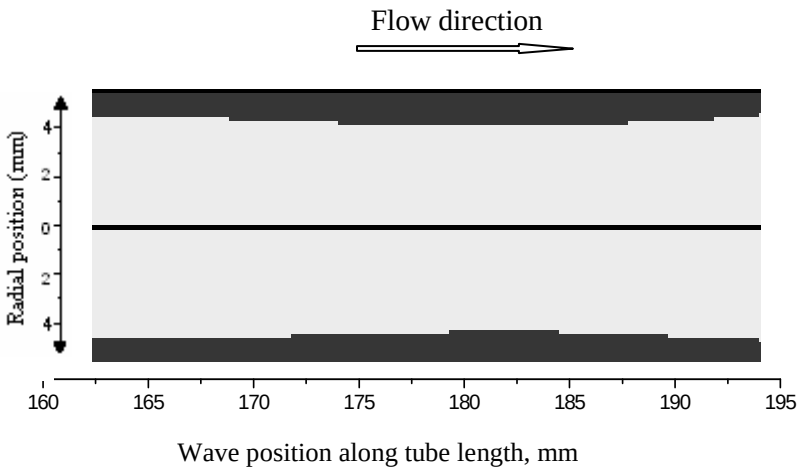

Figure 6.9 Wave shape and dimensions of the coarser mesh II (V_g = 6 m/s; V_l = 1 m/s) at t = 2.163 s.

Comparison of wave parameters: The results of comparing the wavelength and wave height of all four waves are summarized in Table 6.7. For convenience, the wave parameters of these meshes are shown in Figure 6.10. It can be seen that the wave height appears not to be influenced by the different meshes. The standard and the finer meshes produce almost the same wavelengths while those of the two coarser meshes are different. These results show that the standard mesh meets the requirement to generate mesh-independent results. This conclusion is further confirmed by the velocity profiles comparison at the wave crest of different meshes.

Table 6.7 Comparison of wave parameters: wave height and wavelength

Mesh	Node number	Wavelength (mm)	Wave height (mm)
Standard mesh	2,020	25.4	1.1
Finer mesh	2,226	25.3	1.1
Coarser mesh I	1,539	29.6	1.1
Coarser mesh II	1,241	31.6	1.1

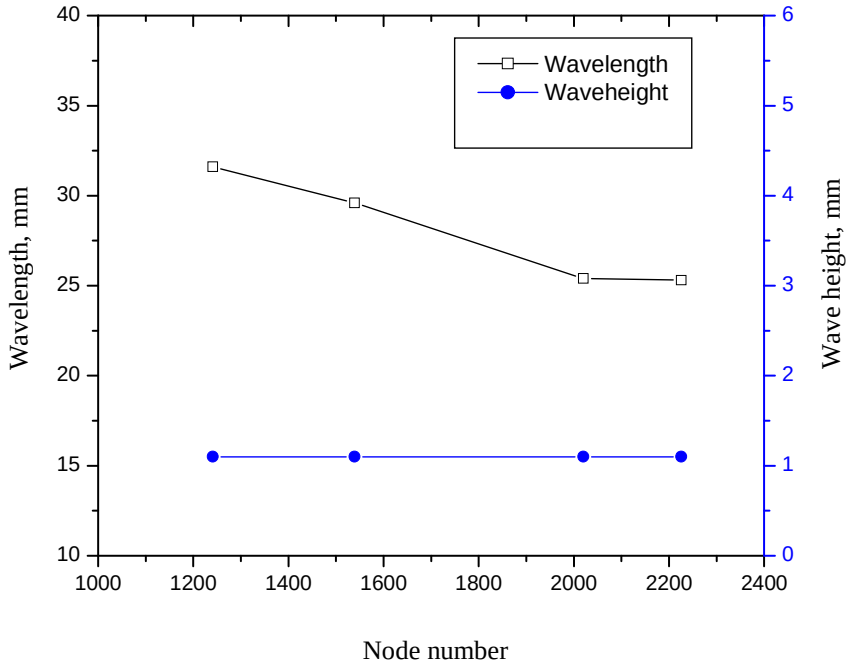

Figure 6.10 Comparison of the wave height and wavelength of the different meshes.

Comparison of velocity profiles: The velocity profiles at the wave crests of the above four individual waves are compared and the results are shown in Figure 6.11. Also, the wave crest positions are listed in Table 6.8. Figure 6.11 clearly shows that the three velocity profiles plus the one for the standard case overlap, which further confirms that the simulation results based on the standard mesh are mesh-independent.

Table 6.8 Position of the wave crest of the different meshes

Mesh	Node number	Wave crest position, x (mm)
Standard mesh	2,020	$x_1 = 180.0$
Finer mesh	2,226	$x_2 = 179.8$
Coarser mesh I	1,539	$x_3 = 180.8$
Coarser mesh II	1,241	$x_4 = 181.9$

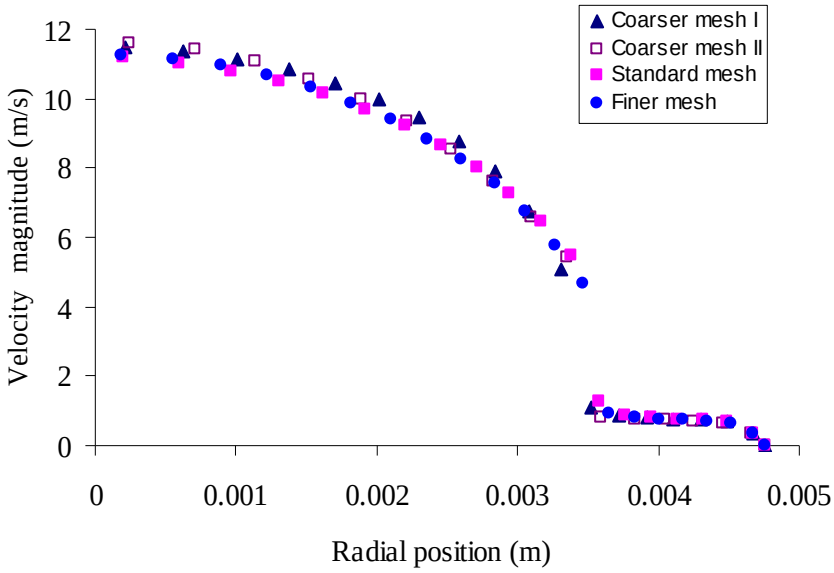

Figure 6.11 Comparison of the velocity profiles at the wave crests of different meshes.

6.3.5 Step 5: Sensitivity Studies

The purpose of the calculations presented in this section is to evaluate the effect of certain assumptions and parameters on the simulation results. The assumptions and parameters evaluated in the simulations are: turbulence intensity of the two phases at tube inlet, input film thickness at the inlet, inlet gas velocity, inlet liquid velocity, surface tension, and gravity. The corresponding and specific cases are designed as shown in Table 6.9. The calculations are based on the base case. All the model settings for each calculation are the same as those of the base case except for the parameter to be changed and those influenced by it. The results are presented in terms of the changes in wavelength and wave height as a result of changing a particular parameter.

Table 6.9 Specific cases for the sensitivity studies

Sensitivity calculations	Schemes		
Turbulence intensity of the two phases, I (%)		I_{gas}	I_{liquid}
	Base case	1	1
	Sensitivity of I_{liquid}	1	0.8
		1	0.2
	Sensitivity of I_{gas}	0.8	1
		0.5	1
Velocity of the two phase at the tube inlet (m/s)		V_g	V_l
	Base case	6	1
	Sensitivity of V_g	12	1
		15	1
	Sensitivity of V_l	6	0.9
		6	1.1
Input liquid film thickness (mm)	Base case	0.5625	
	New case	0.3625	
	New case	0.7625	
Surface tension (N/m)	Base case	0.072 (water-air)	
	New case	0	
Gravity (m^2/s)	Base case	0	
	New case	9.81	

Sensitivity of turbulence intensity: In the results of Table 6.9, when evaluating the influence of the gas turbulence intensity, the liquid turbulence intensity is kept constant at I_{liquid} = 1 %. Likewise, when evaluating the liquid turbulence intensity influence, the gas turbulence intensity is kept constant at I_{gas} = 1 %. For each evaluation, two additional calculations were made, as listed in Table 6.9. The results are shown in Figures 6.12 and 6.13. All waves are compared at approximately x = 190 mm for each mesh. Both figures indicate that the wave height is not influenced by changing the turbulence intensity at the inlet while the wavelength experiences small changes. It is not currently known how the turbulence intensity of the two phases influences the wave

structure. Some researchers believed that the interface in annular flow played a role similar to that of a solid wall to suppress the turbulence of the flow. In these calculations, both I_{gas} and I_{liquid} were adjusted in a range of low turbulence. The low turbulence of the two phases should be easily suppressed by the interface according to the above theory and hence causes little influence on the wave structure. It is therefore concluded that the simulation results are not sensitive to the turbulence intensity input values.

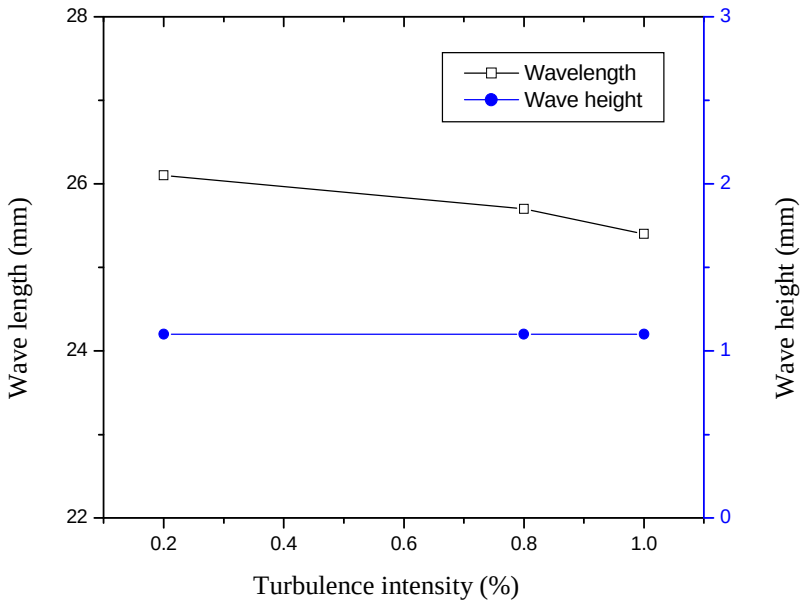

Figure 6.12 Changes of wave parameters due to change in I_{liquid} (I_{gas} = 1 % and t = 2.163 s).

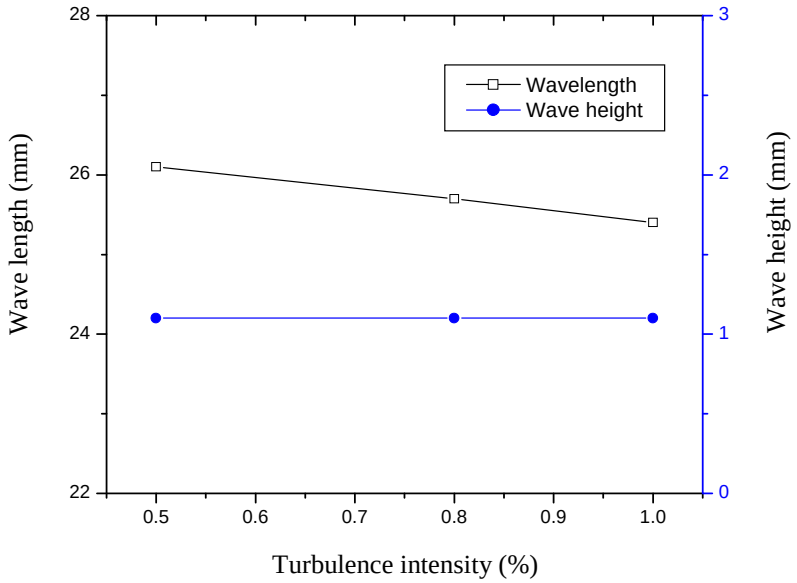

Figure 6.13 Changes of wave parameters due to change in I_{gas} (I_{liquid} = 1 % and t = 2.163 s).

Sensitivity of input film thickness: In the simulation, the width of the water inlet annulus refers to the experimental data of the average liquid film thickness. Two additional cases have been tested and the results are compared with those of the base case in Figure 6.14. The selection criteria of the waves for the comparison are the same as those for the sensitivity calculations of the turbulence intensity. Figure 6.14 indicates that the wavelength is not affected much by the changes in the input film thickness while the wave height is slightly affected. According to the calculations, the wave height changes by 0.3 % ~ 0.5 % for every 1 % change in the average film thickness. It is obvious that larger input film thickness means more water is supplied to the simulation domain. The direct reflection on the wave structure is that the wave height becomes larger due to the increase of the film substrate thickness in the simulation. The film substrate consumes the additional fluid. It is concluded that the simulation results are moderately sensitive to the input film thickness.

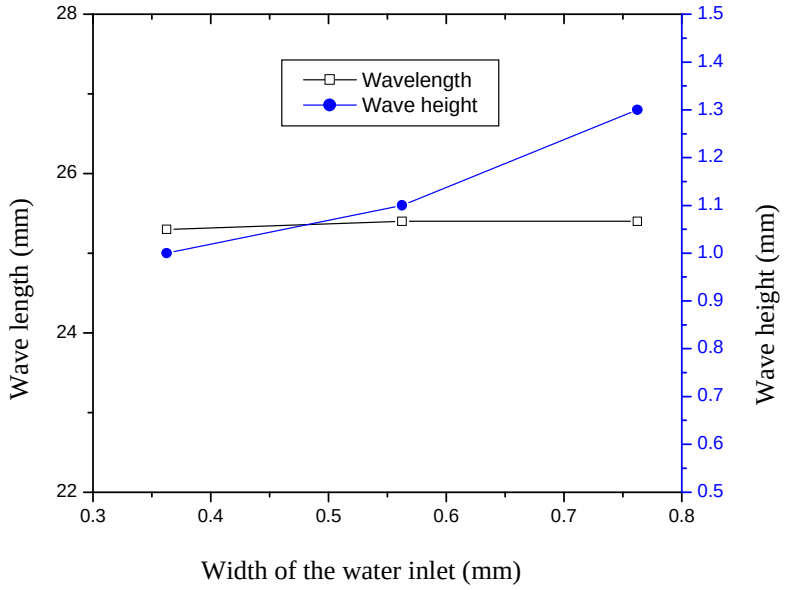

Figure 6.14 Changes of wave parameters in terms of the input film thickness (t = 2.163 s).

Sensitivity of two-phase velocities: The influence of changing the gas and liquid velocities on the simulation results were also assessed. When evaluating the effect of changing the gas velocity, the liquid velocity is kept constant and vice versa. Figures 6.15 and 6.16 illustrate the influence of changing the gas and liquid velocities on the wave parameters. Figure 6.15 shows that the wave height linearly decreases with the increase of the gas velocity while the wavelength increases. It is known from the literature that in annular flow, the gas phase plays a role in the wave structure similar to that imposed by a "suppression force". With the increase of the gas velocity, the wave height is further suppressed and the wavelength is pushed longer. According to calculations, for every 1 % change in the gas velocity, the wave height changes by approximately 0.2 %, and the wavelength changes by 0.3 % ~ 0.4 %. These results indicate that the simulation results are moderately influenced by the gas velocity.

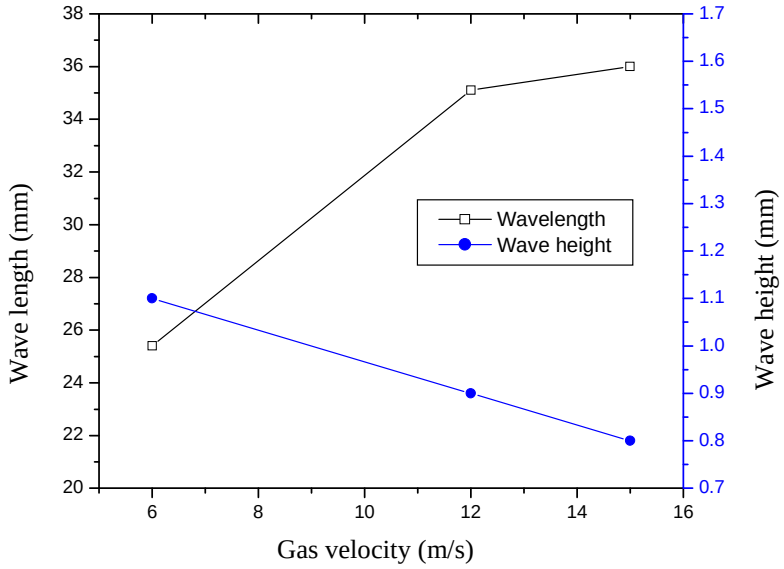

Figure 6.15 Changes of wave parameters as a result of changing V_g (t = 2.163 s).

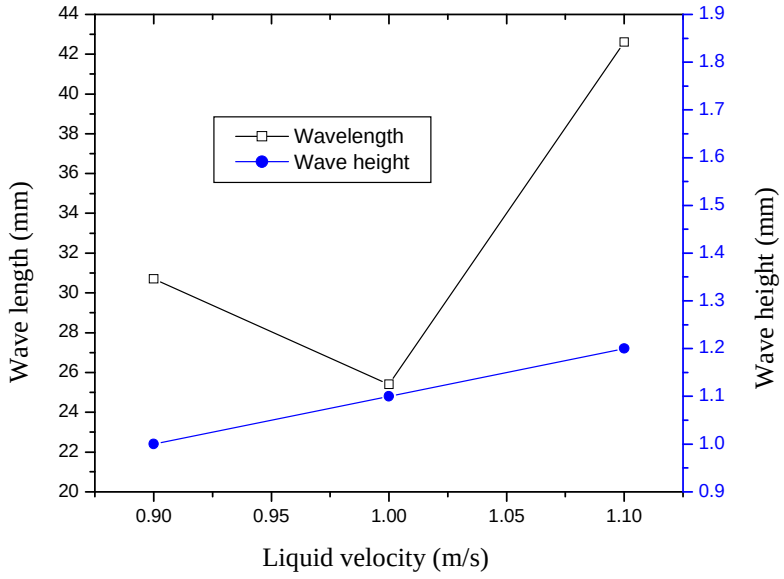

Figure 6.16 Changes of wave parameters as a result of changing V_l (t = 2.163 s).

Figure 6.16 shows that the wave height linearly increases with the increase in the liquid velocity. Compared to the base case, the wavelength increases every time when the liquid velocity changes. According to calculations, the wave height changes

by 0.9 %, and the wavelength changes from 2.1 % to 6.8 %. These results indicate that the simulation results are sensitive to changes in the liquid velocity. Higher liquid velocity means more water is supplied to the simulation domain and the waves are strengthened by the higher velocity liquid. The additional water is distributed in both the longitudinal and radial directions in the wave. Based on the above understanding, the decrease of the liquid velocity will lead to the decrease of the wave height; but it is hard to understand why the wavelength increases. One possible explanation may be that when the liquid velocity decreases, the liquid phase carried by the wave height decreases so significantly that part of the liquid has to be compensated for in the longitudinal direction of the wave.

Sensitivity of surface tension: Surface tension is included in the base case. The air-water surface tension coefficient is taken as a constant value of 0.072 N/m in the simulation. In this sensitivity calculation, the surface tension is reduced to zero. The simulation results on the wave parameters are listed in Table 6.10. The table indicates that the wavelength increases by 19 %, and the wave height decreases by 9 % when the surface tension is absent from the simulation. These results are expected since surface tension plays a major role as a stabilizing force for the waves. Once it is absent from the calculations, the ability for the waves to “hold” the liquid in the waves is weakened. Thus, it is concluded that the simulation results are sensitive to surface tension.

Table 6.10 Influence of surface tension on wave parameters

Case	Surface tension	Wavelength (mm)	Wave height (mm)
Standard	Included	25.4	1.1
New	Not included	30.2	1.0

Sensitivity calculation of gravity: In all the previous simulations, gravity was not considered. In order to evaluate its role in the flow, it was added to the base case. Results show that with gravity, annular flow was not achieved any more in this study. This indicates that gravity plays a destabilizing role in the vertical upward annular flow in a manner opposite to that of surface tension. Thus, the simulation results are much more sensitive to the presence of gravity in the simulation. Part of the simulation image when the gravity is present in the flow is shown in Figure 6.17.

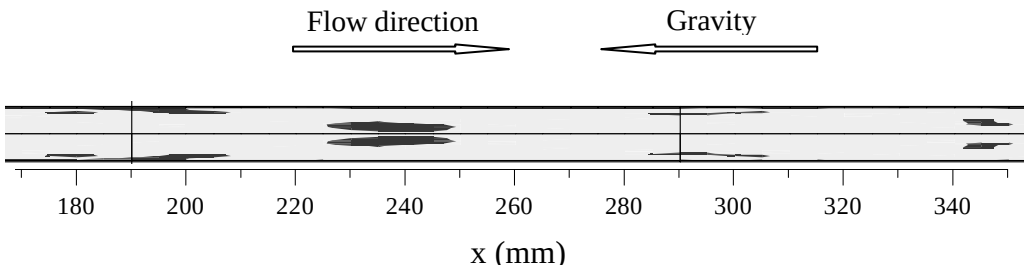

Figure 6.17 Simulated flow in the presence of gravity (V_g = 6 m/s; V_l = 1 m/s; and t = 3.11486 s).

6.4 Summary

Based on the physical attributes of annular flow, as presented in the earlier chapters, a transient two-dimensional turbulence model was established to investigate the liquid entrainment mechanism in annular flow. The RNG k-ε turbulence model in conjunction with the enhanced wall treatment method was used to deal with the turbulence of the flow, and the geometric reconstruction scheme of VOF model was adopted to track the gas-liquid interface. Fluent® 6.18 was employed as the solution tool.

The simulation results showed two domains: a smooth region and a wavy region. In the first region, the two-phase interface is smooth and the two-phase velocities are strongly affected by the input velocity distribution. In the wavy region the waves were generated on the interface, and the region could be further classified into transitional wavy region and fully-developed wavy region. In the transitional wavy region, the waves are small and the two-phase velocities are still influenced by the input velocity distribution. After some distance from the inlet, the waves grow and the velocity profiles of both phases become independent of the inlet velocity distribution.

Several meshes were used to examine if the results are mesh-independent. The comparisons with the base case indicated that the simulation results are in fact mesh-independent. Sensitivity calculations were also conducted to evaluate the effects of the assumptions and parameters used in the modeling on the simulation results. The results showed that:

(a) the simulation results are moderately affected by the input film thickness and the inlet gas velocity;

(b) the simulation results are sensitive to the inlet liquid velocity, surface tension, and gravity; and

(c) the simulation results are insensitive to the turbulence intensity of the two phases.

CHAPTER 7

SIMULATION II: RESULTS AND DISCUSSION

7.1 Introduction

This chapter presents and discusses the liquid entrainment mechanisms from the results of Simulation II. The entrainment mechanisms arising from the simulations are analyzed and compared with each other. They are also compared with the wave entrainment mechanisms found in the open literature. The characteristics of the waves on the interface from simulations are also introduced. Finally, the comparisons of the flow regimes resulting from the simulations with those obtained experimentally are made.

7.2 Wave Structure and Progression

In the previous chapter, it was shown from the simulation results (Figure 6.6) that a fully-developed wave has a wavelength of 25 mm, approximately three times the tube diameter; and a wave peak of about 1.1 mm, slightly larger than the average liquid film thickness. These features are typical of disturbance waves. In addition, just as in the case of a disturbance wave, the wave crest on the leeward side is relatively steep

while the part on the windward side is relatively smooth. Therefore, it can be concluded that the waves generated on the interface are disturbance waves.

The other wave characteristic that could be seen in the simulation is that they are dynamic. That is, they are continually developing over time and changing their shapes, under the action of the gas flow, from the moment of their inception. Figure 7.1 shows a number of interfacial waves in the wavy region. By careful examination of the wave shapes at the upstream locations of 250 – 280 mm and downstream locations of 310 – 350 mm, the reader can deduce that these waves are different from each other. In particular, the last two waves downstream have started to protrude into the gas core as demonstrated by the shape of the wave crests. The protruding part is due to the action of the gas flow on the wave crest and, as it develops further, it will finally be sheared off from the wave crest and entrained in the form of droplets in the gas core.

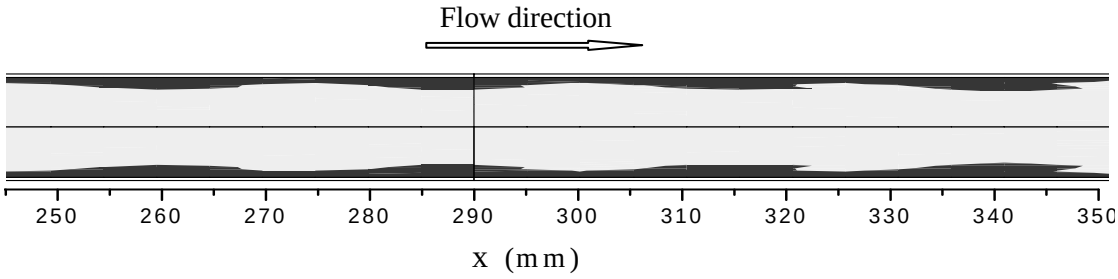

Figure 7.1 Waves in the enlarged wavy region of Case I (V_g = 6 m/s; V_l = 1 m/s); t = 2.163 s.

It should be noted that the static wave profiles as reported by Sekoguchi et al. (1985) and Zhu (2004) reflect a snap shot of the waves at a particular location within a very short life span (typical of such disturbance waves). To illustrate this even further,

Figure 7.2 shows the experimental data of the transient liquid film thickness (MacGillivray, 2004), which clearly demonstrates the chaotic nature of the liquid waves.

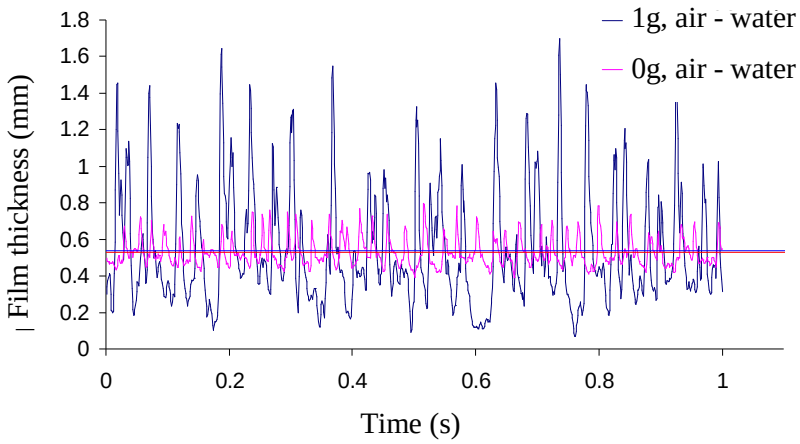

Figure 7.2 Time trace of the waves at different gravity levels (MacGillivray, 2004).

7.3 Liquid Entrainment Mechanisms

The simulation results confirm that the waves on the interface are in fact dynamic waves. They are continually changing from initial growth to further development and eventually their crests break off by the gas phase resulting in entrained liquid into the gas core. During this process, and in addition to the interactions between the two phases, it is also found that under certain conditions neighboring waves interact with each other, which further contributes to the entrainment process.

From this study, two types of liquid entrainment mechanisms are identified: one mechanism (from Case II with comparatively higher gas velocity) shows that an individual wave keeps on developing and deforming and its crest is finally sheared off by the gas phase; the other mechanism shows wave coalescence as the source of the

waves breaking off into the gas core. The two mechanisms are presented in detail in this section. It should be noted that all the figures shown here are plotted to the same scale and that the dark color always represents water while the grey color represents air. The entrainment mechanism of Case II is described first since this mechanism is covered by Case I.

7.3.1 Entrainment Mechanism of Case II with Higher Gas Velocity

This mechanism is identified based on the analysis of the simulation results of Case II (the gas velocity is set to 15 m/s). It is found that individual waves in the simulation are generated and in the process of evolving, part of the liquid in the wave crest gains extra momentum from the incoming high speed gas phase. This causes a protruding part to be formed in the wave front. During this process, the wave grows in both the radial and axial directions, absorbing the liquid from the film in front of and behind it. The protruding part continues to be stretched forwards by the incoming high speed gas phase. It draws most of the liquid from the wave crest to maintain its growth. Finally, it is cut off by the higher-speed gas phase and is entrained into the gas core. Figures 7.3 (a) – (j) show the entire liquid entrainment process and demonstrate how the evolution of an individual wave eventually leads to liquid entrainment.

Figure 7.3 (a) shows that an individual wave has already grown to become a disturbance wave at time t = 3.00 s. After 0.02 s, it can be seen in Figure 7.3 (b) that the wave front becomes shorter and steeper. This indicates that the liquid in the wave crest moves relatively fast under the influence of the gas phase and absorbs part of the wave front. Figure 7.3 (c) further confirms this trend. After another 0.02 s, as shown in Figure

7.3 (d), the faster liquid in the wave crest moves ahead of the wave front and protrudes into the gas core. With time, the protruding part of the wave further develops while at the same time, the liquid film before and after the wave becomes thinner. The wave crest is stretched in both the axial and radial directions. This indicates that the wave draws the liquid phase from the film. In addition, due to the lift of the interfacial shear stress exerted on the wave by the gas phase, the tip of the protruding part is stretched towards the tube axis; Figures 7.3 (e) – (g) show this process. The protruding part continues to be stretched longer and thinner by the gas phase. It eventually loses its connection to the wave crest and is ultimately broken off and entrained into the gas core. In this process, and because the gas phase cannot provide sufficient lift to the protruding part, it finally reaches a “balanced” position and its surface is flattened as seen in Figures 7.3 (h) – (j). Figure 7.3 (i) shows that the protruding part is barely connected with the wave body. Figure 7.3 (j) indicates that the protruding part has broken off from the wave body and is entrained into the gas core.

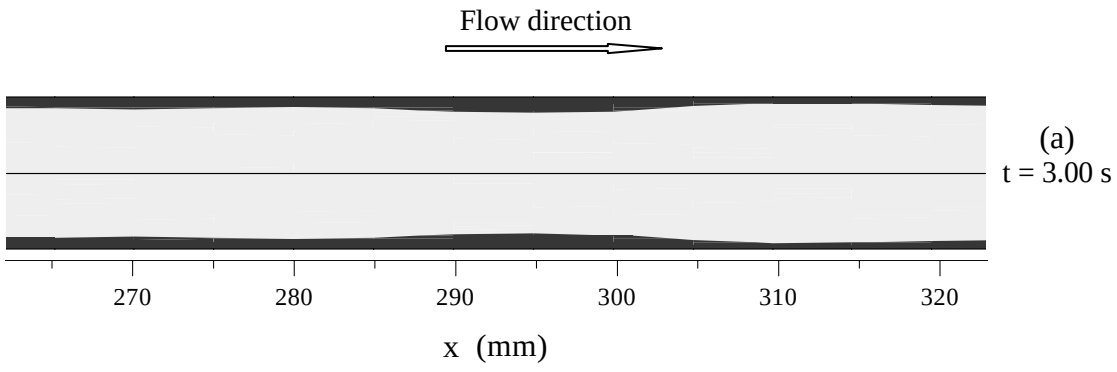

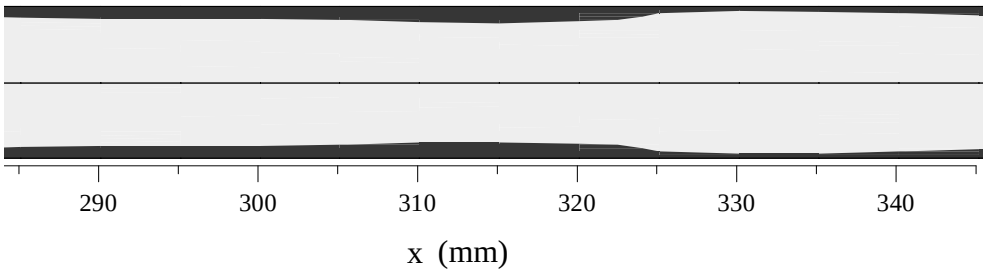

(b)
t = 3.02 s

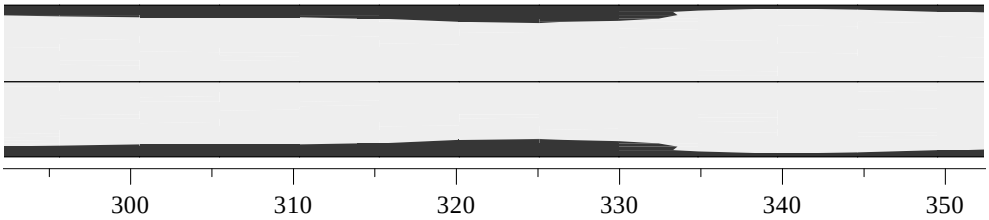

(c)
t = 3.03 s

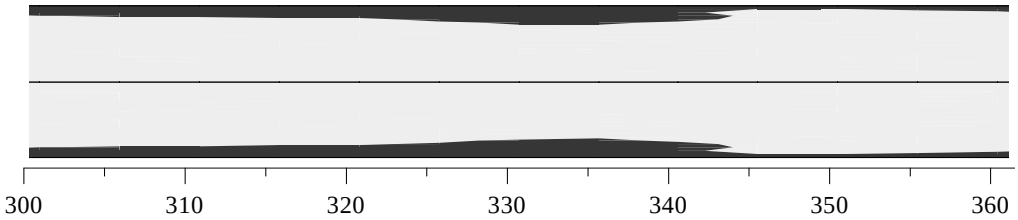

(d)
t = 3.04 s

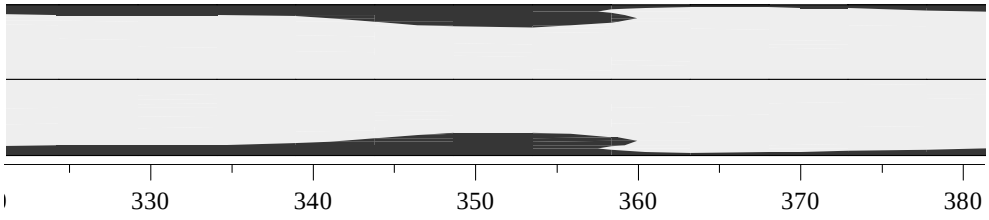

(e)
t = 3.06 s

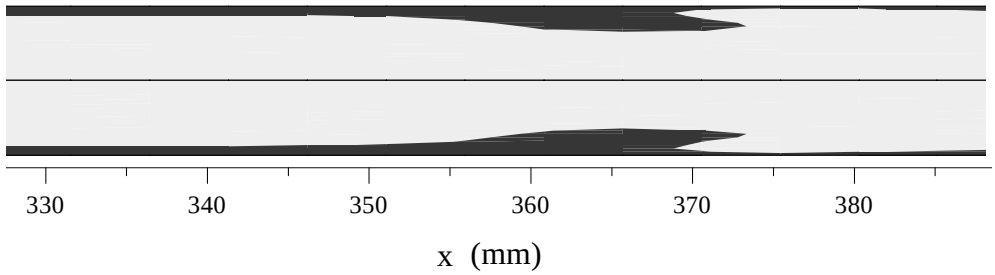

(f)
t = 3.07 s

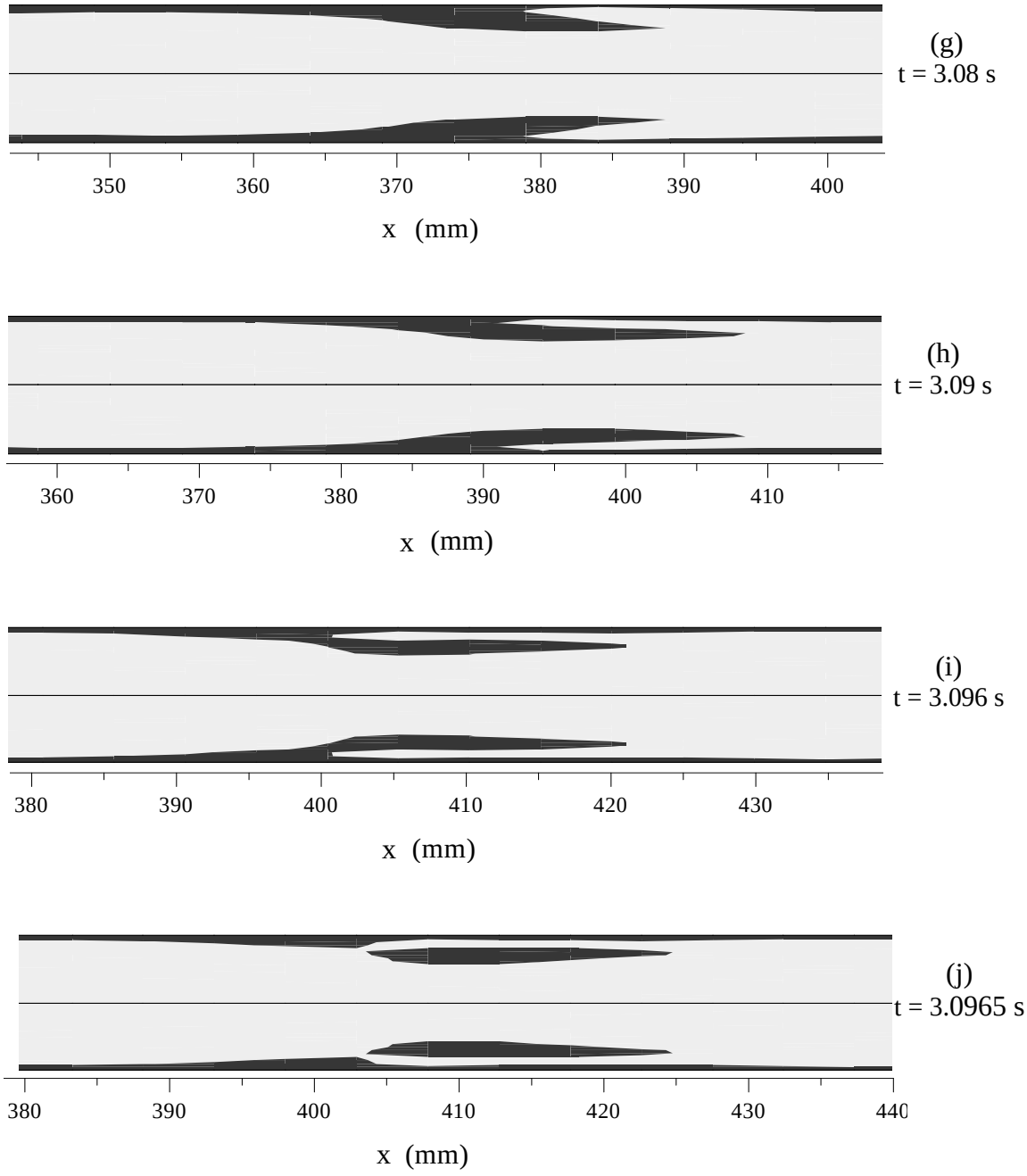

Figure 7.3 Details of wave evolution and liquid entrainment; Case II: V_g = 15 m/s; V_l = 1 m/s.

7.3.2 Entrainment Mechanism of Case I with Lower Gas Velocity

The second entrainment mechanism is identified based on the analysis of the simulation results of Case I with the gas velocity set to 6 m/s. It was found that during the evolution process, consecutive waves on the interface first coalesce before being entrained into the gas core. The entire entrainment process in this case is shown in Figures 7.4 (a) – (k).

Figure 7.4 (a) shows two adjacent waves at t = 2.0709 s. In both cases, the waves resemble the characteristics of a disturbance wave. It can be clearly seen that the downstream wave has already started to protrude into the gas core; while, the upstream wave's short and steep front indicates it is ready to grow a protruding part. The wave amplitudes in both cases are similar. After 0.01 s, the two waves move to new positions each with a slight change in the appearance of the protruding part at the leading edge, as shown in Figure 7.4 (b). With time, the two waves continue to develop. Figures 7.4 (c) – (e) show that the upstream wave is catching up with the downstream one. Because the downstream wave grows much faster compared to its preceding partner, it also faces higher resistance in the flow. This in effect slows the downstream wave. The upstream wave, on the other hand, faces less obstruction and thus moves faster. Finally, as shown in Figures 7.4 (f) – (h), the upstream wave coalesces with the downstream wave. Due to the relatively faster movement of wave crest of the upstream wave, the liquid from its wave crest continues catching up and merging into the downstream wave. The downstream wave continues being strengthened in its amplitude and its protruding part continues to grow larger. During this process, the liquid film near the front region of the

downstream wave becomes much thinner. This suggests that the downstream wave also absorbs liquid from the film to support its evolution. Figure 7.4 (i) shows that the upstream wave is totally absorbed by the downstream wave and the protruding part of the downstream wave continues being lifted towards the tube axis and being stretched in the flow direction. Such changes are due to actions exerted on the wave by the gas phase. Figures 7.4 (j) and 7.4 (k) clearly show that the protruding part is finally sheared off from its wave body and into the gas core.

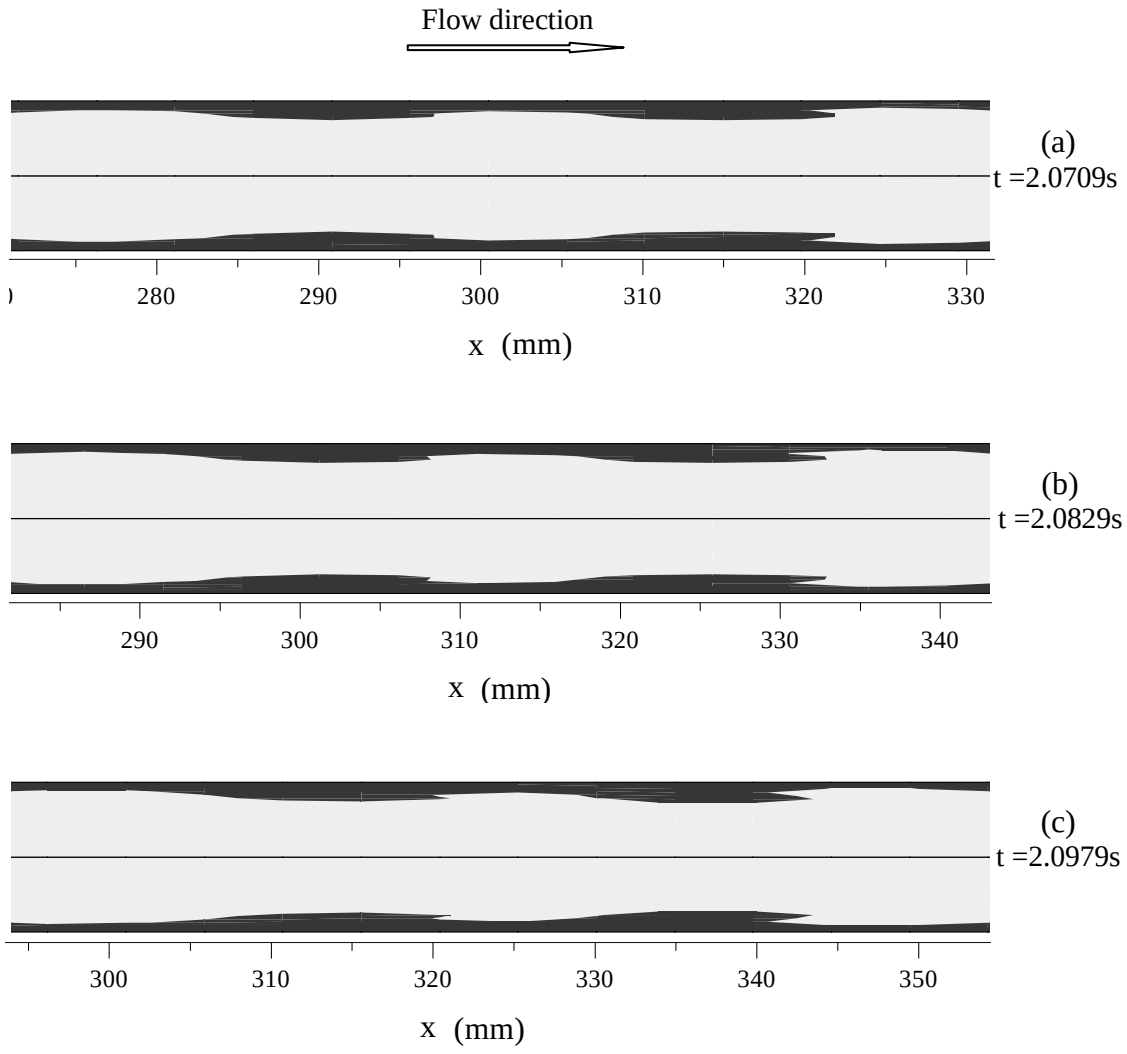

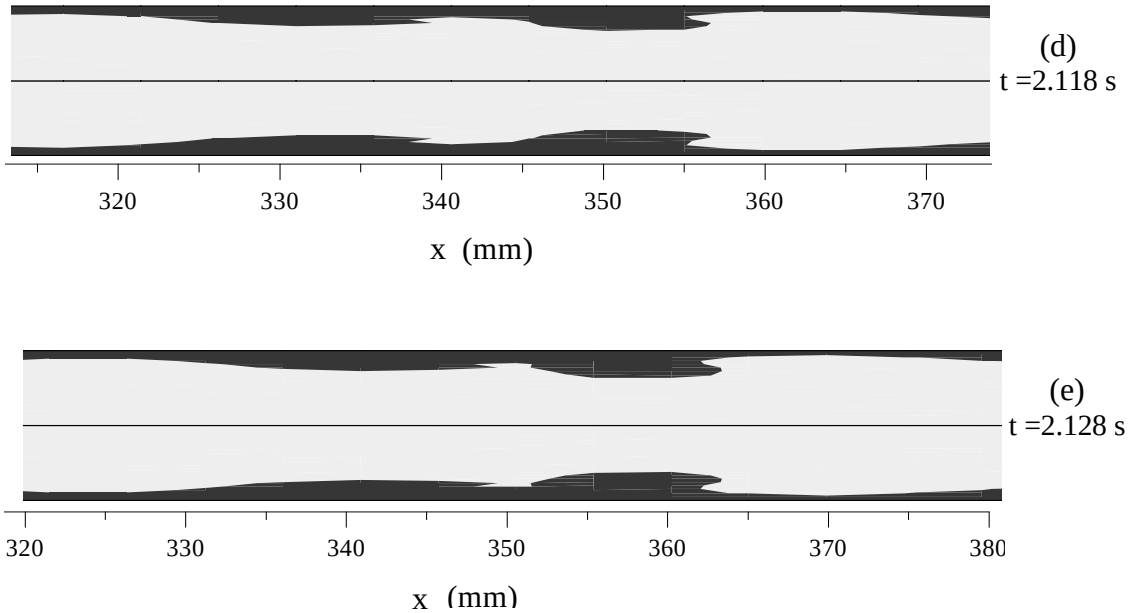
(d)
t =2.118 s
320
330
340
350
360
370
x (mm)
(e)
t =2.128 s
320
330
340
350
360
370
380
x (mm)
(f)
t =2.1355s
330
340
350
360
370
380
x (mm)
(g)
t =2.1455s
340
350
360
370
380
390
x (mm)
(h)
t =2.1555s
350
360
370
380
390
400
x (mm)

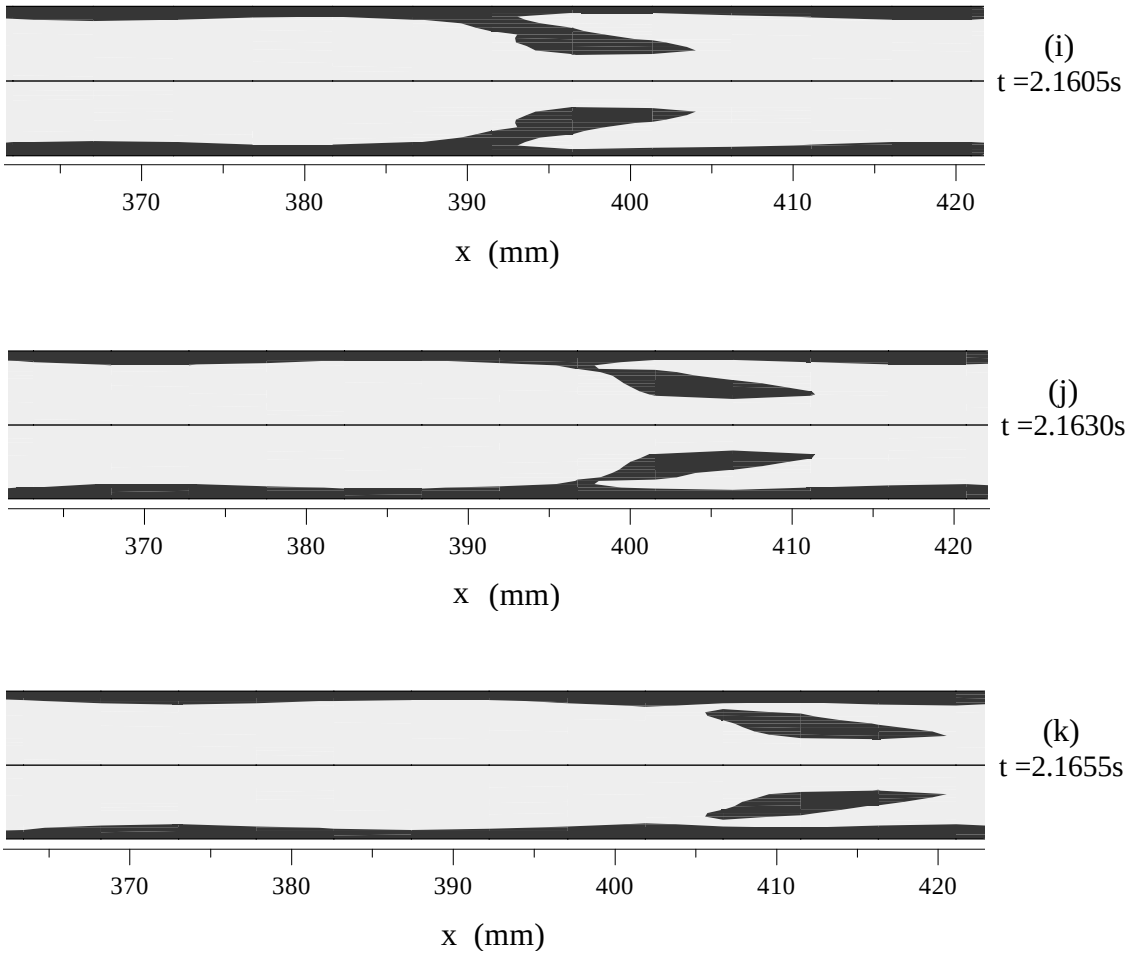

Figure 7.4 Details of wave development and liquid entrainment; Case I: V_g = 6 m/s; V_l = 1 m/s.

In summary, Figures 7.3 (a) – (j) and Figures 7.4 (a) – (k) clearly demonstrate the onset and evolution of the liquid entrainment mechanism in annular flow. The results from both cases show that in both mechanisms, it is the wave crests that are sheared off eventually by the gas flow triggering entrainment to occur. But there are some subtle differences between the two mechanisms. For the entrainment mechanism from Case II, it is the individual wave that develops and deforms under the action of the

faster-moving gas phase. In order to provide enough liquid phase to sustain the wave, the wave draws the liquid phase from the liquid film. For the entrainment mechanism from Case I, the upstream wave is involved in the evolution of the downstream wave. In this mechanism, the two adjacent waves coalesce first during their evolutionary development. The coalescence provides material preparations for further development of the combined wave. The wave crest of the coalesced wave is eventually sheared off by the gas core.

7.3.3 Comparisons with Other Mechanisms in the Literature

This section compares the entrainment mechanisms arising from the present simulations with those available in the open literature. In Chapter 1, four types of wave entrainment mechanisms were introduced to interpret the process of wave crest shearing-off; namely: (a) wave undercut, (b) wave rolling, (c) ripple wave shearing-off, and (d) wave coalescence. It is interesting to note that the two entrainment mechanisms arising from the present simulations are close to the wave undercut entrainment mechanism than any of the other mechanisms. However, there are distinct differences between these mechanisms. In the wave undercut mechanism, it is conjectured that the wave crest is removed from the wave base by the high-speed gas core (see Figure 1.5). In the present simulations, part of the liquid phase in the wave crests is stretched forward in the flow direction until it is broken off by the incoming gas phase.

The entrainment mechanism from Case II displays the wave coalescence process. But this coalescence process is different from other wave coalescence mechanisms found in the open literature in that the wave coalescence in this case does not directly cause the onset of the liquid entrainment process. It provides the liquid

material to trigger the occurrence of the entrainment phenomenon. According to the studies reported in the literature, the wave coalescence entrainment mechanism claims that the liquid droplets are generated when two disturbance waves collide and coalesce. That is, the direct interaction between the two waves causes the liquid phase to be entrained into the gas core.

7.4 Comparisons with Experimental Work

The purpose of this section is to compare the simulation results presented earlier in this chapter with those obtained from the experimental work. It includes a study of the flow patterns arising from the simulation and compares them with the experimental flow regimes.

7.4.1 Flow Patterns from Simulations

In the former sections, it was mentioned that two annular flows were simulated at V_g = 6 m/s and V_g = 15 m/s. In both cases, the liquid velocity, V_l, was kept constant at 1 m/s. In this study, a slug flow was obtained by decreasing the gas velocity from its initial value to 0.5 m/s, while keeping the liquid velocity at 1 m/s. Restricted by the simulation domain, only one whole slug is obtained, which is shown in Figure 7.5. The dark color represents water; and the grey color represents air. It can be seen from the figure that a second slug is forming downstream.

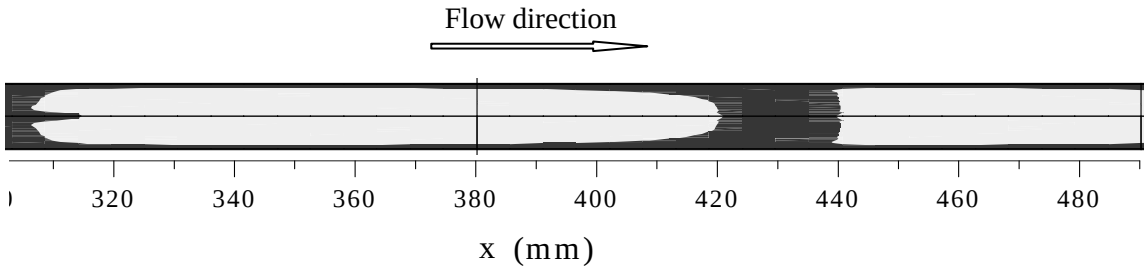

Figure 7.5 Slug flow at V_g = 0.5 m/s; V_l = 1 m/s; and t = 1.7268 s.

Thus, two types of flow patterns are obtained from the present simulations: two annular flows (Cases I & II), and one slug flow when the gas velocity is reduced.

7.4.2 Comparison of Flow Patterns

The results of the flow pattern simulation are similar to those of the experimental work. In the simulation, the two types of flow patterns are obtained in the absence of gravity. Zhao and Rezkallah (1993) achieved a microgravity flow map based on the experimental measurements and observations in a simulated zero-gravity conditions aboard NASA's Zerogravity KC-135 aircraft. They used a dimensionless number, Weber number (We), as the determinant of the different flow regimes in a similar tube size and shape. According to their study, when the gas-phase Weber number, $We_g > 20$, the flow at microgravity condition is annular flow. When $We_g < 1$, the flow is bubble or slug flow; and for values of We between 1 and 20, the flow is transitional. The Weber number is defined as

$$We_g = \frac{V^2 D\rho}{\sigma}, \tag{7.1}$$

where σ is the air-water surface tension and ρ is the density of the gas phase. The We_g for the three simulation cases are calculated and the results are listed in Table 7. 1.

Table 7.1 Weber number of the three simulation cases

Case	Flow pattern in simulation	V_g (m/s)	We_g
Case I	Annular flow	6	6
Case II	Annular flow	15	37
Case III	Slug flow	0.5	0.04

According to the criteria of Zhao and Rezkallah (1993), the simulation flow patterns from Cases II and III agree well with the microgravity flow map while the result from Case I should have been slug-annular flow instead of annular flow. The discrepancy of Case I can be explained in that, based on the sensitivity study, it is known that the presence of gravity greatly influences the flow patterns since gravitational force act as a destabilizing force. In the simulation, gravity is set to zero and its influence on the flow is therefore excluded. However, in the microgravity experiments, while it is significantly reduced, the influence of the gravitational force still exists due to residual gravity effects. Thus, a lower Weber number in the simulation could sustain an annular flow. This is not the case in actual microgravity conditions.

7.5 Summary

The waves on the interface from the simulations were presented. Studies indicate that the simulated waves are of the disturbance wave type. This type of waves is very dynamic in that they are continually changing from initial growth to further development and eventually their crests break off by the incoming gas phase resulting in entrained liquid into the gas core.

From the study, two types of liquid entrainment mechanisms were identified in annular flow and their onset and evolutions were presented. One mechanism shows that

an individual wave keeps on developing and deforming under the action of the faster-moving gas phase until its crest is finally sheared off into the gas core. In this process, the wave draws liquid from the film to sustain its evolution. The other mechanism shows that the coalescence of the two adjacent waves provides material for further development of the combined wave and eventually the shearing-off by the incoming gas phase.

The simulation results confirm the disturbance waves' role in the liquid entrainment process. It also supports a common recognition by other researchers that the liquid entrainment is due to the wave crest shearing-off. But, comparisons with other liquid entrainment mechanisms in the open literature indicate that the two wave entrainment mechanisms presented here are somewhat different.

Finally, the flow patterns arising from the simulations were compared with those from experiments. Comparisons indicate that the results of the flow pattern simulations are similar to those of the experimental work. The discrepancy emerging from the comparisons was justified in the analysis. Therefore, qualitatively speaking, the simulation results are reliable.

CHAPTER 8

CONCLUSIONS AND RECOMMENDATIONS

Liquid entrainment is a very important, but complicated, phenomenon in gas-liquid two-phase annular flow. It causes the liquid film to deteriorate and ultimately be dispersed in the gas core leading to dry-out conditions. Previous studies have shown that entrainment is caused by a fast moving gas phase which tends to shear-off the crests of disturbance waves. However, the exact mechanism by which the droplets are "torn away" from the disturbance waves in annular flow has not been clearly understood. There are several entrainment mechanisms reported in the open literature, yet there is no solid evidence to favor any of them over the others. Experimental evidence is lacking due to the great difficulty of in-situ measurements in the very thin liquid film, and the subjectivity of visual or photographic studies.

In this research, CFD techniques were employed to explore the liquid entrainment mechanisms in annular flows based on the conservation laws. The thesis topics were organized as follows:

- Annular flow features were first analyzed by drawing from the analytical work of Chapter 3 and the numerical studies of Chapter 4. The flow features in the liquid film and gas core were respectively discussed in the two chapters. This work provided the

physical and theoretical basis for the simulation work on the entrainment mechanisms;

- In Chapter 3, flow images of the liquid entrainment phenomena were presented and discussed, and Chapter 4 discussed the force mechanism that triggers the entrainment mechanism based on the simulation results from a turbulence model in the gas core;
- Chapters 6 and 7 established the CFD model and presented the two new entrainment mechanisms resulting from the present simulations.

In addition, entrainment fraction measurements in a small-diameter tube were made and the results were presented and discussed. The challenge of taking such measurements in a small-diameter tube was overcome by designing a new measurement instrument and combining it with a chemically-based titration method. The details were addressed in Chapter 5.

In this chapter, a summary of the conclusions and contributions of this research are summarized and areas of potential future work are also recommended.

8.1 Conclusions

8.1.1 Annular Flow Features

Flow features in the liquid film: Using the average pressure gradient data, the average wall shear stress was calculated. The wall shear stress was further used to calculate the friction velocity and the dimensionless average film thickness, H^+. It was determined that the flow in the liquid film at 1g belongs to the buffer region ($16 < y^+ < 50$). At μg, the dimensionless average film thickness of most annular flows is in a range

of the turbulent core region ($50 < y^+ < 90$). Therefore, it is concluded that the liquid film flow has strong features of near-wall turbulent flow.

Flow features in the gas core: The two-dimensional steady-state RNG k-ε model, in conjunction with the enhanced wall treatment method, was applied to the gas core. The model was validated for single-phase flow and the predictions of the model for annular flow compare well with the experimental and analytical ones.

The simulation results in the gas core, e.g., the velocity profiles at different positions, velocity contour at the wave peak region, pressure contour at the wave peak region, and interfacial shear stress distribution are presented. They showed the turbulent features of the gas core and were stamped with the strong wave effects such as the maximum velocity profile, the minimum pressure distribution, and the most acute change of interfacial shear stress at the wave peak region in the gas core.

8.1.2 Entrainment Phenomenon Images

Flow images of annular flow were analyzed to improve the understanding of the liquid entrainment phenomena. Because of the low frame rate, and the fact that images are presented in 2-D fashion, the results are more qualitative than quantitative. Below is a summary of those results:

(1) The LDCP occurrence frequency is not sensitive to the liquid velocity while the intensity is strengthened with the increase of the liquid velocity;

(2) The LDCP occurrence frequency and intensity increase with the increase of the gas velocity.

8.1.3 Entrainment Mechanism

A transient 2-D turbulence model in conjunction with a VOF scheme was established to investigate the liquid entrainment mechanism in annular flow. The RNG k-ε turbulence model in conjunction with the enhanced wall treatment method was used to model the turbulence of the flow, and the geometric reconstruction scheme of the VOF model was adopted to track the gas-liquid interface. Fluent® 6.18 was employed as the solution tool.

The waves on the interface from the simulations were presented. The shape and dimension characteristics indicate that the simulated waves are disturbance waves. Studies indicate that they are also dynamic waves: they are continually changing from initial growth to further development and eventually their crests break off by the incoming gas phase resulting in entrained liquid into the gas core.

The major accomplishments of this research are not only employing an effective way to explore the liquid entrainment mechanism, but also unveiling the entrainment processes in detail. From the simulations, two types of liquid entrainment mechanisms were identified in annular flow and their onset and evolutions were presented. One mechanism shows that an individual wave keeps on developing and deforming under the action of the faster-moving gas phase and its crest is finally sheared off into the gas core. In this process, the wave draws the liquid phase from the liquid film to sustain its evolution. The other mechanism shows the coalescence of two adjacent waves in their evolutionary developments provides material preparations for further development of the combined wave and the entrainment process.

The simulation results confirm the disturbance waves' role in the liquid entrainment process and support the common recognition by other researchers that the liquid entrainment is due to the wave crest shearing off. However, comparisons with other liquid entrainment mechanisms in the open literature indicate that the two wave entrainment mechanisms developed in this study provide further details on the mechanism.

The flow patterns arising from the simulations were compared with those from experiments. Comparisons indicate that the results of the flow pattern simulations are similar to those of the experimental work, i.e., the simulated slug and annular flows basically agree with the microgravity flow map developed by Zhao and Rezkallah (1993). The discrepancy emerging from the comparisons was justified in the analysis. Therefore, qualitatively speaking, the simulation results are reliable.

8.1.4 Entrainment Fraction Measurement

The newly-designed entrainment fraction measurement method and the experimental entrainment fraction data are also important contributions of this research. A newly-designed and constructed gas-liquid separator, in conjunction with the chemically-based titration method, was used to effectively measure the liquid entrainment fraction in annular flow. The entrainment fraction data showed consistent trends in that the fraction increases with the increase of both the liquid and gas flow rates. Also the injection method had little or no influence on the results for fully developed annular flow. Results also showed that the entrainment fraction was less than 7% over the range of liquid and gas mass fluxes with a maximum uncertainty of 0.26%.

Comparisons with other entrainment data using the liquid film removal method indicated that the new technique can perform as well as the film removal technique (which is currently believed to be the only accurate method for measurements in small-diameter tubes). The comparisons also indicated that the new technique is applicable to lower entrainment fraction data measurements. Repeatability test results verified that the new technique produced reliable, consistent, and repeatable data.

8.2 Recommendations

Based on the accomplishments and limitations of this research work, recommendations for potential future work are proposed in the following two directions: simulation work on entrainment mechanism and experimental work on entrainment fraction measurement.

Simulation work on entrainment mechanism: One limitation of Simulation II is that the gas velocity cannot be further increased to its normal test range as those attained in experiments. If the gas velocity is further increased in the simulation, most of the liquid film will be removed by the gas phase. One reason of this outcome is likely that, in the simulation, the liquid in the film continues to be entrained into the gas core while there is not sufficient liquid to replenish the liquid film. In reality, a good portion of that liquid is deposited back onto the interface. To account for the deposition, mass transfer between the two phases should be considered in future modeling.

In addition, the Simulation II work does not include the gravity term due to its strong destabilizing role in annular flows. This shortcoming is obvious. There is not sufficient experimental data for model validation work because most of the studies of

annular flows were performed at normal gravity, instead of microgravity conditions. This may be also rectified in vertical upward annular flow by using much higher gas velocity. In the simulation, this may balance the downward effect of gravity on the liquid film.

Experimental work on entrainment fraction measurement: In this research, entrainment fraction data were measured at low system pressure and low gas and liquid mass flow rates. The operating conditions were kept the same as those used by other researchers from the Microgravity Research Group. It is worth while to try different operating conditions at higher system pressure and higher gas and liquid mass flow rates. This usually enhances the entrainment process and would provide higher entrainment fraction values than the ones measured in this study.

REFERENCES

Andreussi, P., Asali, J.C., and Hanratty, T.J. (1985). Initiation of roll waves in gas-liquid flows. American Institute of Chemical Engineers Journal, Vol. 31, No. 1, pp. 119-126.

Andreussi, P., and Zanelli, S. (1978). Downward annular and annular-mist flow of air-water mixtures. International Seminar on Momentum Heat Mass Transfer in Two-Phase Energy and Chemical Systems, Dubrovnik, Yugoslavia.

Armbruster, M., Krebs, P., and Rodi, W. (2001). Numerical modelling of dynamic sludge blanket behaviour in secondary clarifiers. Water Science & Technology, Vol. 43, No. 11, pp. 173–180.

Arnold, C.R. and Hewitt, G.F. (1967). Further developments in the photography of two-phase gas-liquid flow. Journal of Photographic Science, Vol 15, pp. 97-114.

Asali, J.C. (1984). Entrainment in vertical gas-liquid annular flow. Ph.D. Thesis, University of Illinois, Urbana, U.S.A.

Asali, J.C. and Hanratty, T.J. (1993). Ripples generated on a liquid film at high gas velocities. International Journal of Multiphase Flow, Vol. 19, No. 2, pp. 229-243.

Asali, J.C., Hanratty, T.J. and Andreussi, P. (1985). Interfacial drag and film height for veritcal annular flow. American Institute of Chemical Engineers Journal, Vol. 31, No. 6, pp. 895-902.

Assad, A., Jan. C.S., Lopez de Bertodano, M.A., and Beus, S.G. (1998). Scaled entrainment measurements in ripple-annular flow in a small tube. Nuclear Engineering and Design, Vol. 184, pp. 437-447.

Azzopardi, B.J. (1983). Mechanism of entrainment in annular two phase flow. UKAEA Report, AERE-R11068.

Azzopardi, B.J. (1986). Disturbance wave frequencies, velocities and spacing in vertical annular two-phase flow. Nuclear Engineering and Design, Vol. 92, pp. 121-133.

Azzopardi, B.J. and Hutchinson, P. (1983). The disintegration of liquid droplets. UKAEA Report, AERE-R10929.

Barbosa, J.R., Jr., Hewitt, G.F., Konig, G., and Richardson, S.M. (2002). Liquid entrainment, droplet concentration and pressure gradient at the onset of annular flow in a vertical pipe. International Journal of Multiphase Flow, Vol. 28, pp. 943-961.

Behzadi, A., Issa, R.I., and Rusche, H. (2004). Modelling of dispersed bubble and droplet flow at high phase fractions. Chemical Engineering Science, Vol. 59, No. 4, pp. 759-770.

Benson, D.J. (2002). Volume of fluid interface reconstruction methods for multi-material problems. Applied Mechanics Reviews, Vol. 55, No. 2, pp. 151-165.

Bhaskaran, R. (2002). Fluent Tutorial: Turbulent Pipe Flow. Cornell University, Sibley School of Mechanical and Aerospace Engineering, U.S.A.

Brackbill, J.U., Kothe, D.B., and Zemach, C. (1992). A continuum method for modeling surface tension. Journal of Computational Physics, Vol. 100, pp. 335-354.

Choudhury, D. (1993). Introduction to the renormalization group method and turbulence modeling. Fluent Inc. Technical Memorandum TM-107, 1993

Clarke, A. and Issa, I. (1997). A numerical model of slug flow in vertical tubes. Computers & Fluids. Vol. 26, No. 4, pp. 395-415.

Coleman, H.W., and Steele, W.G. (1999). Experimentation and Uncertainty Analysis for Engineers (2nd edition). New York : Wiley, U.S.A.

Cook, M., and Behnia, M. (2001). Bubble motion during inclined intermittent flow. International Journal of Heat and Fluid Flow, Vol. 22, No. 5, pp. 543-551.

Cooper, K.D., Hewitt, G.F., and Pinchin, B. (1964). Photography of two-phase gas-liquid flow. Journal of Photographic Science, Vol. 12, pp. 269.

Cousins, L.B., and Hewitt, G.F. (1968). Liquid phase mass transfer in annular two phase flow: droplet deposition and liquid entrainment. UKAEA Report, AERE-R5657.

Cousins, L.B., Denton, W.H., and Hewitt, G.F. (1965). Liquid mass transfer in annular two-phase flow. Proceedings of Symposium on Two-Phase Flow, Exeter, U.K., Vol. 1, Paper C4.

Dallman, J.C., Laurinat, J.E., and Hanratty, T.J. (1984). Entrainment for horizontal annular gas-liquid flow. International Journal of Multiphase Flow, Vol. 10, No. 6, pp. 677-690.

DeBar, R. (1974). Fundamentals of the KRAKEN code. Technical Report UCIR-760, LLNL.

Dukler, A.E., Wicks, M., and Cleveland, R.G. (1964). Frictional pressure drops in two-phase flow. American Institute of Chemical Engineers Journal, Vol.10, pp. 44.

Dykhno, L.A. and Hanratty, T.J. (1996). Use of the interchange model to predict entrainment in vertical annular flow. Chemical Engineering Communications, Vols. 141 – 142, pp. 207-235.

Essemiani, K., Ducom, G., Cabassud, C., and Liné, A. (2001). Spherical cap bubbles in a flat sheet nanofiltration module: experiments and numerical simulation. Chemical Engineering Science, Vol. 56, No. 21-22, pp. 6321-6327.

Fore, L.B., and Dukler, A.E. (1995). Droplet deposition and momentum transfer in annular flow. American Institute of Chemical Engineers Journal, Vol. 41, No. 9, pp. 2040-2046.

Gao, H., Gu, H.Y., Guo, L.J. (2003a). Numerical study of stratified oil–water two-phase turbulent flow in a horizontal tube. International Journal of Heat and Mass Transfer, Vol. 46, No. 4, pp. 749-754.

Gao, D., Morely, N.B., and Dhir, V. (2003b). Numerical simulation of wavy falling film flow using VOF method. Journal of Computational Physics, Vol. 192, pp. 624-642.

Garner, F.H., Ellis, S.R.M., and Lacey, J.A. (1954). The size distribution and entrainment of droplets. Transactions of the Institution of Chemical Engineers, Vol. 32, pp. 222 .

Gill, L.E., Hewitt, G.F. Hitchon, J.W., Lacey, P.M.C. (1963). Sampling probe studies of the gas core in annular two-phase flow-I: the effect of length on phase and velocity distribution. Chemical Engineering Science. Vol. 18, No. 8, pp. 525-535.

Gill, L.E., Hewitt, G.F., Lacey, P.M.C. (1964). Sampling probe studies of the gas core in annular two-phase flow-II: studies of the effect of phase flow rates on phase and velocity distribution. Chemical Engineering Science. Vol. 19, No. 9, pp. 665-682.

Gosman, A.D., Lekakou, C., Politis, S., Issa, R.I., and Looney, M.K. (1992). Multidimensional modeling of turbulent two-phase flows in stirred vessels. American Institute of Chemical Engineers Journal, Vol. 38, pp. 1946-1956.

Hall-Taylor, N., Hewitt, G.F., and Lacey, P.M.C. (1963). The motion and frequency of large disturbance waves in annular two-phase flow of air-water mixtures. Chemical Engineering Science, Vol. 18, pp. 537-552.

Hanratty, T.J., and Hershman, A. (1961). Initiation of roll waves. American Institute of Chemical Engineers Journal, Vol. 7, No. 3, pp. 488-497.

Hewitt, G.F., and Govan, A.H. (1990). Phenomena and prediction in annular two-phase flow, advances in gas-liquid flows – 1990 : presented at the winter annual meeting. American Society of Mechanical Engineers, Winter Meeting (1990, Dallas, Tex.), pp. 41-56.

Hewitt, G.F., Hall-Taylor, N.S. (1970). Annular Two-Phase Flow. Pergamon Press, Oxford, pp. 136-139.

Hewitt, G.F., Jayanti, S., and Hope, C.B. (1990), Structure of thin liquid films in gas-liquid horizontal flow. International Journal of Multiphase Flow, Vol. 16, No. 6, pp. 951-957.

Hewitt, G.F. and Lovegrove, P.C. (1969). Frequency and velocity measurements of disturbance waves in annular two-phase flow. AKAEA Report, AERE-R4304.

Hieu, P.D., Katsutoshi, T., and Ca, V.T. (2004). Numerical simulation of breaking waves using a two-phase flow model. Applied Mathematical Modelling, Vol. 28, No. 11, pp. 983-1005.

Hinkle, W.D. (1967). A study of liquid mass transport in annular air-water flow. Ph.D. thesis, Department of Nuclear Engineering, Massachusetts Institute of Technology, U.S.A.

Hirt, C.W., and Nichols, B.D. (1981). Volume of fluid (VOF) method for the dynamics of free boundaries. Journal of Computational Physics, Vol. 39, pp. 201-225.

Holowach, M.J., Hochreiter, L.E., and Cheung, F.B. (2002). A model for droplet entrainment in heated annular flow. International Journal of Heat and Fluid Flow, Vol. 23, pp. 807-822.

Huang, A., Christodoulou, C., and Joseph., D.D., (1994). Friction fractor and holdup studies for lubricated pipelining—II laminar and k-ε models of eccentric core flow. International Journal of Multiphase Flow, Vol. 20, No. 3, pp. 481-491.

Hutchinson, P., Whalley, P.B., and Hewitt, G.F. (1974). Transient flow redistribution in annular two-phase flow. International Journal of Multiphase Flow, Vol. 1, No. 3, pp. 383-393.

Ishii, M., and Grolmes, M.A. (1975). Inception criteria for droplet entrainment in two-phase concurrent film flow. American Institute of Chemical Engineers Journal, Vol. 21, No. 2, pp. 308-318.

Issa, R.I. (1982). Solution of the implicit discretized fluid flow equations by operator splitting. Mechanical Engineering Department Rep. FS/82/15, Imperial College, London, UK.

Issa, R.I. (1986). Solution of implicitly discretized fluid flow equations by operator splitting. Journal of Computational Physics, Vol. 62, pp. 40-65.

Issa, R.I., and Oliveira, P.J. (1994). Numerical prediction of phase separation in two-phase flow through T-junctions. Computers & Fluids, Vol. 23, No.2, pp. 347-372.

Jacowitz, L.A. and Brodkey, R.S. (1964). An analysis of geometry and pressure drop for the horizontal annular two-phase flow of water and air in the entrance region of a pipe. Chemical Engineering Science, Vol. 19, No. 4, pp. 261-274.

Jayanti, S., and Hewitt, G.F. (1997). Hydrodynamics and heat transfer in wavy annular gas-liquid flow: a computational fluid dynamics study. International Journal of Heat and Mass Transfer. Vol. 40, No. 10, pp. 2445-2460.

Jepson, D.M., Azzopardi, B.J., and Whalley, P.B. (1989). The effect of gas properties on drops in annular flow. International Journal of Multiphase Flow, Vol. 15, No. 3, pp. 327-339.

Kang, D.H., Ahn, Y., Oh, B.D., Kim, M.H. (2004). Advanced electromagnetic flowmetry for slug flow: numerical signal prediction and calibration. International Journal of Multiphase Flow, Vol. 30, No. 6, pp. 585-614.

Keeys, R.K.F., Ralph, J.C., and Roberts, D.N. (1970). Liquid entrainment in adiabatic stream water flow at 500 and 1000 Psia. UKAEA Report, AERE-R6293.

Kim, S.-E., Choudhury, D., and Patel, B. (1997). Computations of complex turbulent flows using the commercial code FLUENT. In Proceedings of the ICASE/LaRC/AFOSR Symposium on Modeling Complex Turbulent Flows, Hampton, Virginia, U.S.A.

Kishore, B.N. and Jayanti, S., (2004). A multidimensional model for annular gas-liquid flow. Chemical Engineering Science, Vol. 59, No. 17, pp. 3577-3589.

Krzeczkowski, S.A. (1980). Measurement of liquid droplet disintegration mechanisms. International Journal of Multiphase Flow, Vol. 6, No. 3, pp. 227-239.

Lane, W.R. (1951). Shatter of drops in streams of air. Industrial and Engineering Chemistry, Vol. 43, No. 6, pp. 1312-1317.

Launder, B.E. and Spalding, D.B., (1972). Lectures in Mathematical Models of Turbulence. London, Academic Press.

Li, J. and Renardy, Y., (1999). Direct simulation of unsteady axisymmetric core-annular flow with high viscosity ratio. Journal of Fluid Mechnics, Vol. 391, pp. 123-149

Lopez de Bertodano, M.A., Jan, CS., and Beus, S.G. (1997). Annular flow entrainment rate experiment in a small vertical pipe. Nuclear Engineering and Design, Vol. 178, pp. 61-70.

Lörstad, D. and Fuchs, L. (2004). High-order surface tension VOF-model for 3D bubble flows with high density ratio. Journal of Computational Physics, Volume 200, No. 1, pp. 153-176.

Lyn, D.A., Stamou, A.I. and Rodi, W. (1992). Density currents and shear-induced flocculation in sedimentation tanks. Journal of Hydraulic Engineering, Vol. 118, No. 6, pp. 849–867.

MacGillivray, R. (2004). Gravity and Gas Density Effects on Annular Flow Average Film Thickness and Frictional Pressure Drop. M.Sc. thesis, University of Saskatchewan, Saskatoon, Canada.

Martin, C.J. (1983). Annular Two Phase Flow. Ph.D. thesis, Oxford University, U.K.

Martin, C.J. and Azzopardi, B.J. (1985) Waves in vertical annular flow. Physicochemical Hydrodynamics, Vol. 6, No.12, pp. 257-265

Meknassi, F., Benkirane, R., Liné, A., and Masbernat, L. (2000). Numerical modeling of wavy stratified two-phase flow in pipes. Chemical Engineering Science, Vol. 55, No. 20, pp. 4681-4697.

Moalem Maron, D., Yacoub, N., Brauner, N., and Naot, N. (1991). Hydrodynamic mechanisms in the horizontal slug pattern. International Journal of Multiphase Flow, Vol. 17, No. 2, pp. 227-245.

Moukalled, F., and Darwish M. (2002). Acomparative assessment of the performance of mass conservation-based algorithms for incompressible multiphase flows. Numerical Heat Transfer, Part B. Vol. 42, pp. 259-283.

Newitt, D.M., Dombrowski, N., Knelman, F.H. (1954). Liquid entrainment: I, the mechanism of drop formation from gas or vapor bubbles. Transactions of the Institution of Chemical Engineers, Vol.32, pp. 244.

Newton, C.H., and Behnia, M. (2001). A numerical model of stratified wavy gas–liquid pipe flow. Chemical Engineering Science, Vol. 56, No. 24, pp. 6851-6861.

Noh, W.F., and Woodward, P.R. (1976). SLIC (simple line interface method), in Lecture Notes in Phys., Vol. 59, edited by Van de Vooren, A.I. and Zandbergen, P.J. (Springer-Verlag, Berlin/New York), pp. 330.

Nordsveen, M. (2001). Wave- and turbulence-induced secondary currents in the liquid phase in stratified duct flow. International Journal of Multiphase Flow, Vol. 27, No. 9, pp. 1555-1577.

Ohba, K., and Nagae, K. (1993) Characteristics and behavior of the interfacial wave on the liquid film in a vertically upward air-water two-phase annular flow. Nuclear Engineering and Design, Vol. 141, No. 1-2, pp. 17-25.

Pan, L. and Hanratty, T.J. (2002). Correlation of entrainment for annular flow in vertical pipes. International Journal of Multiphase Flow, Vol. 28, pp. 363-384.

Paras, S.V. and Karabelas, A.J. (1991). Droplet entrainment and deposition in horizontal annular flow. International Journal of Multiphase Flow, Vol. 17, No. 4, pp. 455-468.

Patankar, S.V. (1980). Numerical Heat Transfer and Fluid Flow. Hemisphere Publishing Corporation, Toronto : McGraw-Hill, Canada

Patankar, S.V., Liu, C.H. and Sparrow, E.M. (1977). Fully developed flow and heat transfer in ducts having streamwise-periodic variations of cross-sectional area. Journal of Heat Transfer, Transactions of the ASME, Vol. 99, pp. 180-186.

Patankar, S.V., and Spalding, D.B. (1972). A calculation procedure for heat, mass and momentum transfer in three dimensional parabolic flows. International Journal of Heat and Mass Transfer, Vol. 15, pp. 1787-1806.

Pols, R.M., Hibberd, S., and Azzopardi, B.J. (1998). Discontinuous wave solutions in stratified and annular two-phase flows. Third International Conference on Multiphase Flow. Lyon, France, June 8-12

Pope, S.B. (2000). Turbulent Flows. Cambridge University Press, New York, U.S.A.

Quandt, E.R. (1965). Measurement of some basic parameters in two-phase annular flow. American Institute of Chemical Engineers Journal, Vol. 11, No. 2, pp. 311-318.

Schadel, S.A. (1988). Atomization and deposition rates in vertical annular two-phase flow. Ph.D. thesis, University of Illinois, Urbana-Champaign, Urbana, Illinois, U.S.A.

Schadel, S.A., and Hanratty, T.J. (1989). Interpretation of atomization rates of the liquid film in gas-liquid annular flow. International Journal of Multiphase Flow, Vol. 15, No. 6, pp. 893-900.

Schadel, S.A., Lemana, J.L., and Hanratty, T.J. (1990). Rates of atomization and deposition in vertical annular flow. International Journal of Multiphase Flow, Vol. 16, No. 3, pp. 363-374.

Sekoguchi, K., Takeishi, M., and Ishimatsu, T. (1985). Interfacial structure in vertical upward annular flow. PhysicoChemical Hydrodynamics, Vol. 6, pp. 239-255.

Shen, Y.M., Ng, C.O., and Chwang. A.T. (2003). A two-fluid model of turbulent two-phase flow for simulating turbulent stratified flows. Ocean Engineering, Vol. 30, No. 2, pp. 153-161.

Shih, T.-H., Liou, W.W., Shabbir, A., Yang, Z., and Zhu, J. (1995). A new k-ε eddy-viscosity model for high Reynolds number turbulent flows - model development and validation. Computers & Fluids, Vol. 24, No. 3, pp. 227-238.

Taha, T., and Cui, Z. (2002). Hydrodynamic analysis of upward slug flow in tubular membranes. Desalination, Vol. 145, No. 1-3, pp. 179-182.

Troshko, A.A., and Hassan, Y.A. (2001). Two-equation turbulence model of turbulent bubbly flows. International Journal of Multiphase Flow, Vol. 27, No. 11, pp. 1965-2000.

Van Doormaal, J.P., and Raithby, G.D. (1984). Enhancement of the SIMPLE method for predicting incompressible fluid flows. Numerical Heat Transfer, Vol. 7, pp. 147-163.

Van Rossum, J.J. (1959). Experimental investigation of horizontal liquid films – wave formation, atomization, film thickness. Chemical Engineering Science, Vol. 11, pp. 35-52.

Vitasovic, Z., Zhou, S., McCorquodale, J.A., and Lingren, K., (1997). Secondary clarifier analysis using data from the Clarifier Research Technical Committee Protocol. Water Environment Research, Vol. 69, No. 5, pp. 999–1007.

Wallis, G.B., (1962). The onset of droplet entrainment in annular gas-liquid flow. General Electric Report, No.62, GL127.

Wallis, G.B. (1969a). One-Dimensional Two-Phase Flow. New York: McGraw-Hill, Inc, U.S.A.

Wallis, G.B. (1969b), ibid, pp. 386.

Webb, D.R. (1970). Studies of the characteristics of downward annular two-phase flow. Part 3. UKAEA Report, AERE-R6426.

Whalley, P.B. (1987a). Boiling, Condensation, and Gas-Liquid Flow. Oxford University Press, New York, United States

Whalley, P.B. (1987b). ibid. pp. 36-37.

Whalley, P.B., Hewitt, G.F., and Hutchinson, P. (1973). Experimental wave and entrainment measurements in vertical annular two-phase flow. UKAEA Report, AERE-R7521.

White, F.M. (1999). Fluid Mechanics (4^{th} edition). Boston: McGraw-Hill, U.S.A.

Wilkes, N.S., Azzopardi, B.J., and Thompson, C.P. (1983). Wave coalescence and entrainment in vertical annular two-phase flow. International Journal of Multiphase Flow, Vol. 9, No. 4, pp. 383-398.

Willetts, I. (1987). Non-Aqueous Annular Two-Phase Flow. Ph.D. thesis, University of Oxford, U.K.

Wongwises, S. and Naphon, P. (1998) Heat - mass transfer and flow characteristics of two-phase countercurrent annular flow in a vertical pipe. International Communications in Heat and Mass Transfer, Vol. 25, No. 6, pp. 819-829.

Woodmansee, D.E., and Hanratty, T.J. (1969). Mechanism for the removal of droplets from a liquid surface by a parallel air flow. Chemical Engineering Science, Vol. 24, pp. 299-307.

Wu, J.C. and Minemura, K. (1999). Numerical prediction of turbulent bubbly two-phase flow in a rotating complicated duct. International Journal for Numerical Methods in Fluids, Vol. 29, No. 7, pp. 811-826.

Yakhot, V., and Orszag, S.A. (1986). Renormalization group analysis of turbulence: I. basic theory. Journal of Scientific Computing, Vol. 1, No. 1, pp. 1-51.

Youngs, D.L. (1982). Time dependent multi-material flow with large fluid distortion. Numerical Methods for Fluid Dynamics, Morton, K.W. and Baines, M.J. (editors), New York: Academic Press, U.S.A., pp. 273-285.

Youngs, D.L. (1987). An interface tracking method for a 3D Eulerian hydrodynamics code. Tech Report AWRE/44/92/35, AWRE Design Math Division

Zhao, L., and Rezkallah, K.S. (1993). Gas-liquid flow patterns at microgravity conditions. International Journal of Multiphase Flow, Vol. 19, No. 5, pp. 751-763.

Zhou, S., McCorquodale, J.A., and Vitasovic, Z. (1992). Influences of density on circular clarifiers with baffles. ASCE, Journal of Environmental Engineering, Vol. 118, No. 6, pp. 829–847.

Zhu, Z.F. (2004) A Study of the Interfacial Features of Gas-Liquid Annular Two-Phase Flow, M.Sc. thesis, University of Saskatchewan, Saskatoon, Canada.

APPENDIX A: DERIVATION OF MIXTURE DENSITY IN GAS CORE

A new method, based on momentum conservation law, was used to calculate the mixture density (ρ). It is assumed that all of the liquid droplets are entrained into the gas core at some instance. At the instant when the liquid droplets have just been entrained into the gas core, assume the droplet mass flow rate to be $\dot{m}_{TD}$; and the droplets velocity, V_{TD}. Thus,

$$V_{TD} = \frac{\dot{m}_{TD}}{\rho_l A}, \tag{A.1}$$

where A is the cross section of the gas core.

Let $\dot{m}_g$ be the gas mass flow rate in the gas core, and V_g, its velocity, from which it can be deduced

$$V_g = \frac{\dot{m}_g}{\rho_g A}. \tag{A.2}$$

Now assume the entrained droplets are evenly mixed with the gas phase in the gas core without momentum loss, and that the mixture flows at a velocity of V after mixing. According to the momentum conservation law,

$$\dot{m}_g V_g + \dot{m}_{TD} V_{TD} = (\dot{m}_g + \dot{m}_{TD})V. \tag{A.3}$$

Substitute (A.1) and (A.2) into (A.3) to obtain

$$V = \frac{1}{(\dot{m}_g + \dot{m}_{TD})A}\left[\frac{(\dot{m}_g)^2}{\rho_g} + \frac{(\dot{m}_{TD})^2}{\rho_l}\right]. \tag{A.4}$$

Since,

$$\rho VA = \dot{m}_g + \dot{m}_{TD}\,, \tag{A.5}$$

then, substitute (A.4) into (A.5); the mixture density is finally obtained

$$\rho = \frac{(\dot{m}_g + \dot{m}_{TD})^2}{\dfrac{(\dot{m}_g)^2}{\rho_g} + \dfrac{(\dot{m}_{TD})^2}{\rho_l}}\,. \tag{A.6}$$

APPENDIX B: INTERFACIAL SHEAR STRESS IN GAS CORE

According to the homogeneous flow model, the total pressure gradient is expressed by

$$(-\frac{dp}{dz})_{total} = (-\frac{dp}{dz})_F + (-\frac{dp}{dz})_g + (-\frac{dp}{dz})_{accel}, \quad \text{(B.1)}$$

where the frictional pressure gradient is calculated from

$$(-\frac{dp}{dz})_F = \frac{4\tau}{d}, \quad \text{(B.2)}$$

the gravitational pressure gradient is obtained from

$$(-\frac{dp}{dz})_g = \rho g \sin\theta \quad (\text{here} \quad \theta = 90°), \quad \text{(B.3)}$$

and the accelerational pressure gradient is zero for steady state flow; thus

$$(-\frac{dp}{dz})_{accel} = 0. \quad \text{(B.4)}$$

Here, τ is the interfacial shear stress, i.e. 'wall shear' in the simulation, 'd' is the actual average diameter of the gas core (tube diameter minus 2 times the liquid film thickness), and ρ is the mixture density.

Substituting (B.2), (B.3), (B.4), and other known variables in Chapter 4 into (B.1), the following result is obtained

$$\tau = 5.07 \ \text{(Pa)}. \quad \text{(B.5)}$$

APPENDIX C: DRAWINGS OF SEPARATOR

Parts view: Unit: mm; Material**:** Plexiglas or other transparent material.

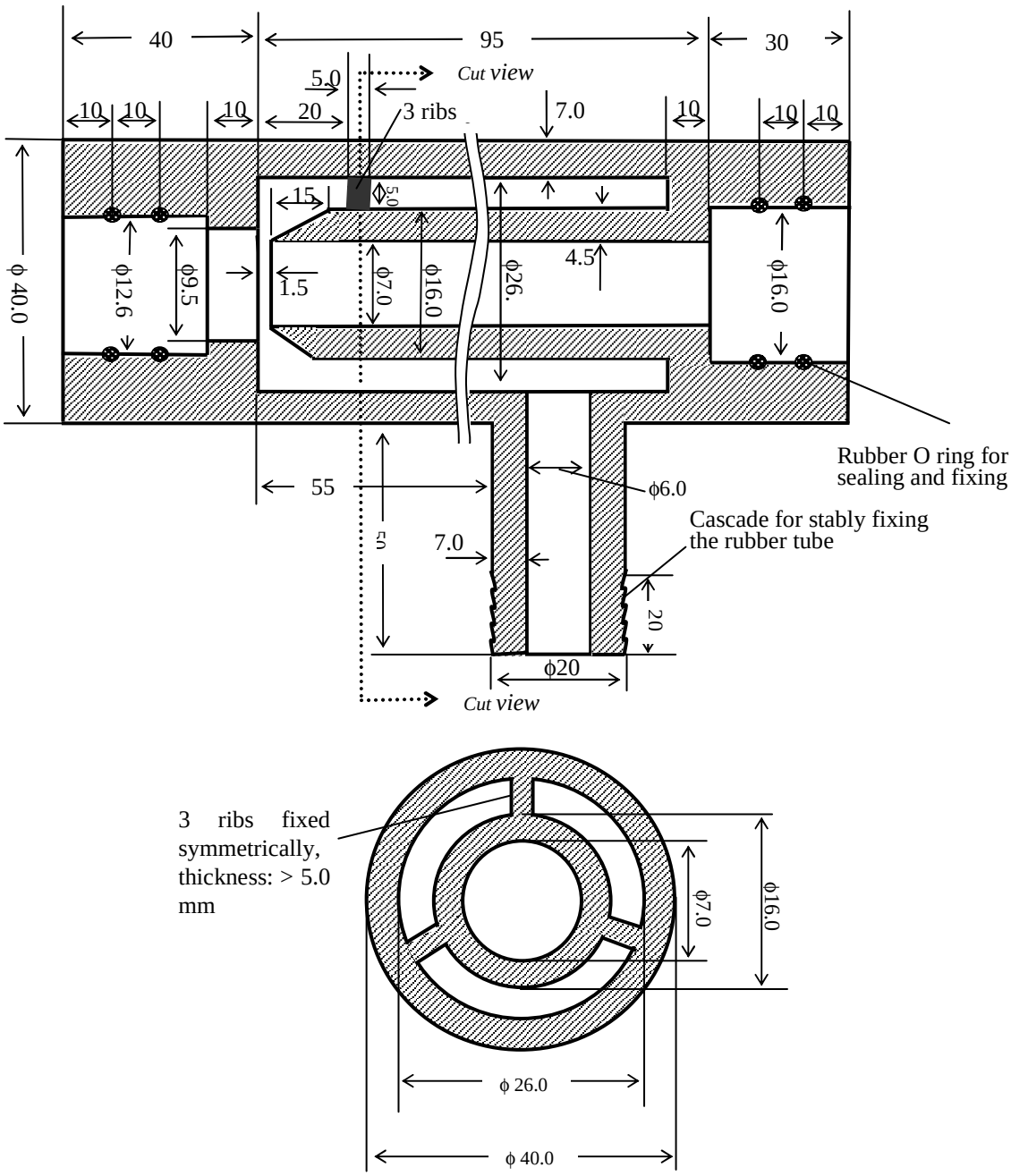

Cut view

Figure C.1 Detailed schematic of the separator.

APPENDIX D: TITRATION METHOD

Titration is a traditional method that is used to determine the concentration of a certain ion in a solution. In order to examine the concentration of Ca^{2+}, a reagent, EDTA, is applied to titrate $CaCl_2$ solutions.

1. Apparatus and reagent

The following components are needed: white paper, a 500-ml Flask, a 500-ml beaker, a 5-ml pipette, a 10-ml pipette, a 25-ml pipette, and an air pump.

The following reagents are needed: ~ 0.005 M EDTA (*Ethylenediaminetetraacetic* acid) solution, ~ 2.33 M $CaCl_2$ solution, PH = 10 ammonia buffer solution, and a visual indicator such as Calmagite solution.

2. Titration Principle

Calmagite is one of the best indicators for calcium/magnesium. It forms a complex with calcium/magnesium in a solution at PH = 10. This complex has a distinct red color at calcium/magnesium concentrations as low as 1×10^{-6} M. When EDTA titrant is added, free calcium/magnesium ions will react with it. After all the free calcium/magnesium ions are consumed, the next portion of EDTA will react with the calcium/magnesium of the indicator complexes, and at the same time convert the indicator to a blue color complex. By observing the color change of solution and recording the amount of EDTA titrant added, the concentration of calcium and magnesium can be determined.

Because water for the test loop inherently contains a little calcium/magnesium, each time before an experiment the concentration of this portion of calcium/magnesium is first determined with EDTA. The droplet and liquid film solutions are then titrated to determine their total calcium/magnesium concentrations. The difference between the total calcium/magnesium concentration in solution and the inherent calcium/magnesium concentration in water is the added calcium concentration.

3. Titration Procedure

a) Transfer 25 ml water first to a beaker, using the 25-ml pipette.

b) Add ~ 5 ml PH = 10 ammonia buffer solution into the beaker, using the 10-ml pipette.

c) Add 12 drops of Calmagite indicator.

d) Titrate with the EDTA solution, using the 5.00-ml pipette. Observe the color change of solution, as the solution changes from a wine-red to a pure blue, at which time the end point has been reached. Add EDTA slowly drop by drop at the end point until the blue color does not change anymore. A piece of white paper is to be placed under the beaker for convenient observations.

e) Keep the beaker and titrated water as standard of color comparison for later titrations.

The concentration of calcium/magnesium in water will be therefore determined. Repeat the above procedures to obtain a reliable result.

As to the titration of droplets and liquid film solutions, transfer the same amount of sample solution as that of water into the flask, and repeat the above procedures. The total concentration of calcium/magnesium in the solution can then be solved. The

difference between the total concentration of calcium/magnesium in solution and their concentration in water is the concentration of injected calcium in droplets or film solution, i.e.,

$$C_{CD} = C_{CDS} - C_{CW}, \text{ and } C_{CL} = C_{CLS} - C_{CW}, \tag{D.1}$$

where, C_{CD} and C_{CL} are concentrations of added $CaCl_2$ in the collected droplet sample solution and liquid film sample solution, respectively; C_{CDS} and C_{CLS} are total concentrations of calcium/magnesium in the two solutions; C_{CW} is concentration of original calcium/magnesium in water.

Then, E_{CaCl2} can be determined by the titration method. The values of m_{CD} and m_{CL} are: $m_{CD} = m_{TD} C_{CD}$, $m_{CL} = m_{L} C_{CL}$. Substituting them into equation (5.6) in Chapter 5, the following result is obtained

$$E_{CaCl_2} = \frac{m_{TD} C_{CD}}{m_{TD} C_{CD} + m_L C_{CL}} \times 100\%. \tag{D.2}$$

The equation (D.2) is used in Chapter 5 as equation (5.11).

APPENDIX E: ISOKINETIC CONDITION ANALYSIS

This work is to analyze if the flow in the experiments meets the requirement of an isokinetic condition. If not, then the analysis will determine which type of non-isokinetic condition was reached during the experiments.

Figure E.1 is a sketch of the separator that was installed in the experimental loop. In this sketch (not to scale), some parts of the loop are neglected for conciseness, and some parts of the separator are enlarged for clarity. C is a point between the blade tip of the inner cylinder and the tube wall, and it is assumed to be outside of the liquid film region. D is a point close to the blade tip inside the inner cylinder.

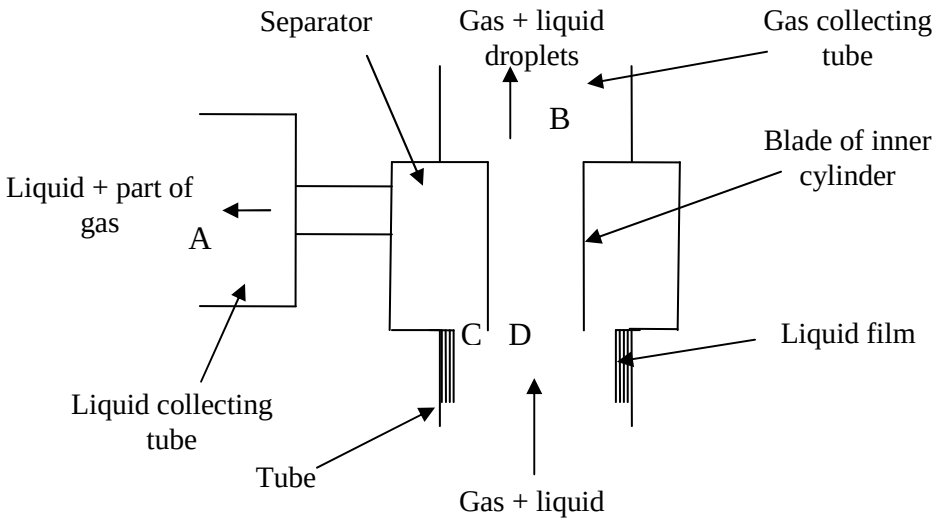

Figure E.1 Schematic of the separator in test loop (truncated).

There are two possible non-isokinetic conditions in the experimental loop. One is the pressure at point C, P_C, being larger than the pressure at point D, P_D, i.e. $P_C > P_D$. The other is if $P_C < P_D$. If $P_C = P_D$, this is the isokinetic condition which is ideal for the experiments. In the first condition, more liquid film will be sheared-off and directed to the inner cylinder of the separator. This would lead to large entrainment fraction measurement if this part of film is not counted in the results. In the second condition ($P_C < P_D$), more of the gas phase containing the liquid droplets would be pushed into the liquid collecting tube. This would cause small entrainment fraction measurement if the droplets in this part of gas phase were not considered.

The design of the separator was done in such a way that the gap between the blade of the inner cylinder and the tube wall was sufficiently large to allow part of the gas phase to be collected with the liquid film. The following analysis will demonstrate if the isokinetic condition was met in the experiments.

Take an annular flow case for example. The data used for this calculation are collected from the experiments and are listed in Tables E.1 and E.2.

Table E.1 Annular flow data

Gas mass flow rate, Q (kg/s)	0.00228
Liquid mass flow rate (kg/s)	0.02045
Average liquid film thickness, H (mm)	0.251
Gas mass flow rate at the end of liquid collecting tube , Q_1 (kg/s)	1/6 Q
Gas mass flow rate at end of gas collecting tube , Q_2 (kg/s)	5/6 Q
Pressure at the end of liquid collecting tube, P_A (Pa)	P_0, standard pressure
Pressure at the end of gas collecting tube, P_B (Pa)	P_0, standard pressure

Table E.2 Test section and sensor dimensions

Diameter of liquid collecting tube, D_A	9.53 mm
Length of liquid collecting tube, L_A	1.2 m
Diameter of gas collecting tube, D_B	9.53 mm
Length of gas collecting tube, L_B	1.2 m
Diameter of tube, D	9.53 mm
Diameter of inner cylinder, D_D	7.0 mm

In the experiments, one sixth of the gas phase was measured in the liquid collecting tube and the remainder was discharged into the gas collecting tube. Bernoulli's equation was applied to the two flow streams of the gas phase using the points shown in Figure E.1 above,

$$P_C + \frac{\rho V_C^2}{2} = P_A + \frac{\rho V_A^2}{2} + f_A \frac{L_A}{D_A} \rho \frac{V_A^2}{2} \text{ and} \tag{E.1}$$

$$P_D + \frac{\rho V_D^2}{2} = P_B + \frac{\rho V_B^2}{2} + f_B \frac{L_B}{D_B} \rho \frac{V_B^2}{2}, \tag{E.2}$$

where V_A, V_B, V_C, and V_D are the gas velocities at the liquid collecting tube end and the gas collecting tube end, respectively (points C, and D in Figure E.1); ρ is the gas density; and f_A and f_B are flow friction factors which are functions of flow Reynolds No. and relative roughness. The friction factor f in this study is determined from the Moody diagram (White, 1999).

It should be noted that the gas mentioned here is actually a mixture of air and entrained liquid droplets. As noted in the body of the thesis, the liquid droplet cross-sectional distribution was assumed uniform in the small-diameter tube. In addition, even if the entrained liquid droplets are considered in this study, the mixture physical

properties do not change much in comparison with those of the pure gas phase according to the correlations of mixture density and viscosity available in literature. Thus in equations (E.1) and (E.2), only the gas density ρ is used in the calculation. V_A, V_B, V_C, and V_D are determined from the following equations

$$V_A = Q_1 / (\frac{\pi}{4} D_A^2 \rho), \tag{E.3}$$

$$V_B = Q_2 / (\frac{\pi}{4} D_B^2 \rho), \tag{E.4}$$

$$V_C = Q_1 / \{\frac{\pi}{4} [(D - 2H)^2 - D_D^2] \rho\}, \text{ and} \tag{E.5}$$

$$V_D = Q_2 / (\frac{\pi}{4} D_D^2 \rho). \tag{E.6}$$

Based on equations (E.3) and (E.4) and air physical properties in Table 4.2, the flow Reynolds numbers of collecting tube A and B are 2.8×10^4 and 1.4×10^5, respectively. According to the Moody diagram (White, 1999), if the two collecting tubes are assumed smooth, the ratio of f_A / f_B could reach its maximum value, 1.5.

Substituting (E.3), (E.4), (E.5), (E.6), and the data into (E.1) and (E.2),

$$P_C \approx P_0 + \frac{8Q^2}{\pi^2 \rho} \times 10^{-12} \times 200 + 2 f_A (\frac{Q^2}{9\pi^2 \rho} \frac{L_A}{D_A^5}) \text{ and} \tag{E.7}$$

$$P_D \approx P_0 + \frac{8Q^2}{\pi^2 \rho} \times 10^{-12} \times 4058 + 50 f_B (\frac{Q^2}{9\pi^2 \rho} \frac{L_B}{D_B^5}). \tag{E.8}$$

Comparing equations (E.7) and (E.8), it is obvious that $P_C < P_D$, which means that the isokinetic condition has not been met in the experiments. It is the second non-isokinetic condition that was met in the experiments, which means more parts of gas phase would be pushed into the liquid film side.

APPENDIX F: EXPERIMENTAL UNCERTAINTY ANALYSIS

The results from the experiments were shown in Figure 5.4 to fit into a series of linear curves according to the different gas superficial velocities. These linear curves reflect the relationship between the liquid entrainment fraction data and the liquid velocities at different gas velocities. They can be presented by the same form as follows

$$E_i = mV_i + b, \tag{F.1}$$

where E_i is the liquid entrainment fraction data, V_i is the liquid flow rate; and m and b are coefficients. The coefficients m and b are determined by

$$m = \frac{N\sum_{i=1}^{N}(V_i E_i) - \sum_{i=1}^{N} V_i \sum_{i=1}^{N} E_i}{N\sum_{i=1}^{N} V_i^2 - (\sum_{i=1}^{N} V_i)^2} \quad \text{and} \tag{F.2}$$

$$b = \frac{\sum_{i=1}^{N} V_i^2 \sum_{i=1}^{N} E_i - \sum_{i=1}^{N} V_i \sum_{i=1}^{N} (V_i E_i)}{N\sum_{i=1}^{N} V_i^2 - (\sum_{i=1}^{N} V_i)^2}. \tag{F.3}$$

For the linear regression equation, the precision uncertainty is given by

$$SEE = \left[\frac{\sum_{i=1}^{N} (E_i - E_{LS,i})^2}{N - C} \right]^{1/2}, \tag{F.4}$$

where C is the coefficient number of the linear regression equation (i.e. C = 2 for m and b two constants); N = 6 for each group data in these experiments. Therefore, the

uncertainty for the data represented by the linear curve can be calculated according to the following expression:

$$U(E) = \left[(t * SEE)^2 + B_{Ei}{}^2\right]^{1/2}, \tag{F.5}$$

where the student t number is the function of the number of degrees of freedom, and B_{Ei} is systematic uncertainty.

The calculations of precision uncertainty according to equation (F.4) are done using an Excel sheet. But, the calculations of systematic uncertainty are more complex in that the contribution to the systematic uncertainty of each factor that influences the entrainment fraction should be considered. The following are the details.

The ratio of the liquid phase physically sheared into the gas core by the separator to the liquid phase directed to the film collecting tube equals the ratio of the mass of $CaCl_2$ in droplets solution to that in the film solution, i.e.,

$$\frac{m_s}{m_L} = \frac{m_{TD} C_D}{m_L C_L}, \tag{F.6}$$

where C_D, C_L are $CaCl_2$ concentrations in the droplets solution and film solution, respectively. Introducing (F.6) into (5.3), the following result is obtained

$$\begin{aligned} E_L &= \frac{m_D}{m_{TD} + m_L} \times 100\% + \frac{m_{TD}}{m_{TD} + m_L} \frac{C_D}{C_L} \times 100\% \\ &= E_D + E_L \frac{C_D}{C_L}. \end{aligned} \tag{F.7}$$

Organizing equation (F.7), the following result is obtained

$$E_D = (1 - \frac{C_D}{C_L}) E_L . \tag{F.8}$$

According to the experimental and calculation principles to measure the liquid entrainment fraction, the following result is obtained

$$\frac{C_D}{C_L} = \frac{N_1 - N_w}{N_2 - N_w}, \tag{F.9}$$

where N_1 , N_2 , and N_w are the EDTA titrant volumes that are titrated into droplets solution, film solution, and water, respectively. In addition, the following result is obtained

$$\frac{m_{TD}}{m_{TD} + m_L} = \frac{m_1 - m_{1s}}{m_1 - m_{1s} + m_2 - m_{2s}}, \tag{F.10}$$

where m_1, m_2, m_{1s}, and m_{2s} are the masses of droplets solution with container 1, the film solution with container 2, container 1, and container 2, respectively. Introduce equations (F.9) and (F.10) into equation (F.8), the following result is obtained

$$E_D = (1 - \frac{N_1 - N_w}{N_2 - N_w}) \frac{m_1 - m_{1s}}{m_1 - m_{1s} + m_2 - m_{2s}}. \tag{F.11}$$

The uncertainty analysis is based on equation (F.11). The following analysis will use “i” as the subscript of E, instead of “D”.

Because m_1, m_2, m_{1s}, and m_{2s} are measured using the same digital balance apparatus, they all have correlated contributions to the uncertainty. N_1, N_2, and N_w are measured using the same titration instruments, they also have the correlated contributions to the uncertainty. B_{Ei} is calculated according to the following formula:

$$
\begin{aligned}
B_{Ei}^2 = &(\frac{\partial E}{\partial m_1})^2 B_{m_1}^2 + (\frac{\partial E}{\partial m_2})^2 B_{m_2}^2 + (\frac{\partial E}{\partial m_{1s}})^2 B_{m_{1s}}^2 + (\frac{\partial E}{\partial m_{2s}})^2 B_{m_{2s}}^2 + 2\frac{\partial E}{\partial m_1}\frac{\partial E}{\partial m_2} B_{m_1} B_{m_2} \\
&+ 2\frac{\partial E}{\partial m_1}\frac{\partial E}{\partial m_{1s}} B_{m_1} B_{m_{1s}} + 2\frac{\partial E}{\partial m_1}\frac{\partial E}{\partial m_{2s}} B_{m_1} B_{m_{2s}} + 2\frac{\partial E}{\partial m_2}\frac{\partial E}{\partial m_{1s}} B_{m_2} B_{m_{1s}} \\
&+ 2\frac{\partial E}{\partial m_2}\frac{\partial E}{\partial m_{2s}} B_{m_2} B_{m_{2s}} + 2\frac{\partial E}{\partial m_{1s}}\frac{\partial E}{\partial m_{2s}} B_{m_{1s}} B_{m_{2s}} \\
&+ (\frac{\partial E}{\partial N_1})^2 B_{N_1}^2 + (\frac{\partial E}{\partial N_2})^2 B_{N_2}^2 + (\frac{\partial E}{\partial N_w})^2 B_{N_w}^2 + \\
&+ 2\frac{\partial E}{\partial N_1}\frac{\partial E}{\partial N_2} B_{N_1} B_{N_2} + 2\frac{\partial E}{\partial N_1}\frac{\partial E}{\partial N_w} B_{N_1} B_{N_w} + 2\frac{\partial E}{\partial N_2}\frac{\partial E}{\partial N_w} B_{N_2} B_{N_w}
\end{aligned}
\qquad \text{(F.12)}
$$

Let $A = (1 - \frac{N_1 - N_w}{N_2 - N_w})$, and $H = \frac{m_1 - m_{1s}}{m_1 - m_{1s} + m_2 - m_{2s}}$.

Based on equation (F.11),

$$\frac{\partial E_i}{\partial m_1} = A\left[\frac{1}{m_1 - m_{1s} + m_2 - m_{2s}} - \frac{m_1 - m_{1s}}{(m_1 - m_{1s} + m_2 - m_{2s})^2}\right], \qquad \text{(F.13a)}$$

$$\frac{\partial E_i}{\partial m_{1s}} = A\left[-\frac{1}{m_1 - m_{1s} + m_2 - m_{2s}} + \frac{m_1 - m_{1s}}{(m_1 - m_{1s} + m_2 - m_{2s})^2}\right], \qquad \text{(F.13b)}$$

$$\frac{\partial E_i}{\partial m_2} = A\left[-\frac{m_1 - m_{1s}}{(m_1 - m_{1s} + m_2 - m_{2s})^2}\right], \qquad \text{(F.13c)}$$

$$\frac{\partial E_i}{\partial m_{2s}} = A\left[\frac{m_1 - m_{1s}}{(m_1 - m_{1s} + m_2 - m_{2s})^2}\right], \qquad \text{(F.13d)}$$

$$\frac{\partial E_i}{\partial N_1} = H\left[-\frac{1}{N_2 - N_w}\right], \qquad \text{(F.13e)}$$

$$\frac{\partial E_i}{\partial N_2} = H\left[\frac{N_1 - N_w}{(N_2 - N_w)^2}\right], \text{ and} \qquad \text{(F.13f)}$$

$$\frac{\partial E_i}{\partial N_w} = H\left[\frac{N_2 - N_1}{(N_2 - N_w)^2}\right]. \qquad \text{(F.13g)}$$

Therefore, $\frac{\partial E_i}{\partial m_1} = -\frac{\partial E_i}{\partial m_{1s}}$, and $\frac{\partial E_i}{\partial m_2} = -\frac{\partial E_i}{\partial m_{2s}}$.

In equation (F.12), obviously, $B_{m_1} = B_{m_2} = B_{m_{1s}} = B_{m_{2s}} = B_m$ and $B_{N_1} = B_{N_2} = B_{N_w} = B_N$. B_m comes from two sources: uncertainties from the digital balance apparatus itself, and from the collection process. B_N is composed of two parts: uncertainties of sample solution taking with 25-ml pipette and EDTA titrating with 5 ml pipette. For the B_m, the quality of the digital balance is shown in Table F.1.

Table F.1 Quality of digital balance

Reproducibility	0.01 g
Linearity	± 0.02 g

Thus, the uncertainty caused by the digital balance apparatus could be taken as B_{1m} = ± 0.03 g. There are two sources for the process uncertainty during the sample collection. One arises from the difference in the collecting time. However, the droplets solution and film solution are collected at the same time, and hence there are no errors, i.e. B_{tm} = 0. The other source comes from the fluctuating readings of the rotameter. According to the calibrations of rotameter, its accuracy is ± 0.8 G/H, and its random uncertainty is taken as ¼ of the least division, i.e. ± 0.5 G/H. Therefore the contribution of the rotameter to B_m is

$$B_{2m} = B_r \frac{\Delta t}{3600} = \pm \frac{\Delta t}{3600} \sqrt{(0.8)^2 + (0.5)^2} = \pm 0.94 \frac{\Delta t}{3600} \Delta t(G) = 0.99 \Delta t \ \ (g), \qquad (F.14)$$

where Δt is collecting time, s. Above all,

$$B_m = \pm \sqrt{(B_{1m})^2 + (B_{tm})^2 + (B_{2m})^2} = \pm \sqrt{(0.03)^2 + (0)^2 + (0.99\Delta t)^2} \ \ (g). \qquad (F.15)$$

As to B_N, there are two sources for this uncertainty: uncertainty from the solution sample taking and from EDTA titration. For sample taking, assume the accuracy is 2 % of full scale of pipette (25 ml), and the readings error is 1% of the full scale. Therefore,

$$U_{1N} = \pm\sqrt{(25\times 2\%)^2 + (25\times 1\%)^2} = \pm 0.56(\text{ml}) = \pm 0.56 \ \ (\text{g}). \qquad \text{(F.16)}$$

This error is then fossilized into the systematic uncertainty of B_N, i.e.

$$B_{1N} = U_{1N}. \qquad \text{(F.17)}$$

As to EDTA titration, two drops are about 0.1ml. Thus the accuracy is 0.1/2 = 0.05 ml, and the random uncertainty is taken as one-half of the least scale division 0.1/2 = 0.05 ml, therefore the uncertainty caused by EDTA titrating is

$$U_{2N} = \pm\sqrt{(0.05)^2 + (0.05)^2} = \pm 0.071 \ \ (\text{ml}) = \pm 0.071 \ \ (\text{g}). \qquad \text{(F.18)}$$

This error is fossilized into the systematic uncertainty of B_N, i.e.,

$$B_{2N} = U_{2N}. \qquad \text{(F.19)}$$

Therefore,

$$B_N = \pm\sqrt{(B_{1N})^2 + (B_{2N})^2} = \pm\sqrt{(0.56)^2 + (0.071)^2} \ \ (\text{ml}) = \pm 0.56 \ \ (\text{g}). \qquad \text{(F.20)}$$

Introduce (F.13a)-(F.13g), (F.15) and (F.20) into equation (F.12), the following result is obtained

$$B_{Ei}^2 = \left[\begin{array}{l} (\frac{\partial E}{\partial m_1})^2 + (\frac{\partial E}{\partial m_2})^2 + (\frac{\partial E}{\partial m_{1s}})^2 + (\frac{\partial E}{\partial m_{2s}})^2 + 2\frac{\partial E}{\partial m_1}\frac{\partial E}{\partial m_2} + 2\frac{\partial E}{\partial m_1}\frac{\partial E}{\partial m_{1s}} + \\ 2\frac{\partial E}{\partial m_1}\frac{\partial E}{\partial m_{2s}} + 2\frac{\partial E}{\partial m_2}\frac{\partial E}{\partial m_{1s}} + 2\frac{\partial E}{\partial m_2}\frac{\partial E}{\partial m_{2s}} + 2\frac{\partial E}{\partial m_{1s}}\frac{\partial E}{\partial m_{2s}} \end{array} \right] B_m^2 +$$

$$\left[(\frac{\partial E}{\partial N_1})^2 + (\frac{\partial E}{\partial N_2})^2 + (\frac{\partial E}{\partial N_w})^2 + 2\frac{\partial E}{\partial N_1}\frac{\partial E}{\partial N_2} + 2\frac{\partial E}{\partial N_1}\frac{\partial E}{\partial N_w} + 2\frac{\partial E}{\partial N_2}\frac{\partial E}{\partial N_w} \right] B_N^2$$

$$= 0 \quad \text{(g)}.$$

(F.21)

The systematic uncertainty in the measurement has no effect on the overall errors. This occurs because the partial derivatives with respect to variables are equal in magnitude but opposite in sign. In addition, the correlations among variables are perfect to ease the errors.

Finally, the precision uncertainty and systematic uncertainty are calculated. Therefore, the uncertainty to the experimental data could be solved according to equation (F.5). All the calculations are performed using Excel. In the calculations, t = 2.571 corresponding to 5 degrees of freedom and 95% confidence. The results are shown in Figure (5.9) and Table F.2.

Table F.2 Uncertainty to the experimental data

V_{sl} (m/s)	V_{sg}(m/s)				
	25.8	30.9	35.8	40.6	45.5
0.15	± 0.18	± 0.26	± 0.07	± 0.24	± 0.25
0.18	± 0.18	± 0.26	± 0.07	± 0.24	± 0.25
0.21	± 0.18	± 0.26	± 0.07	± 0.24	± 0.25
0.24	± 0.18	± 0.26	± 0.07	± 0.24	± 0.25
0.27	± 0.18	± 0.26	± 0.07	± 0.24	± 0.25
0.29	± 0.18	± 0.26	± 0.07	± 0.24	± 0.25

In Table F.2, the first column is the liquid superficial velocities; the second row is the gas superficial velocity. Other data are the uncertainties corresponding to the different gas and liquid superficial velocities.

Table F.3 shows the entrainment fraction data corresponding to the different gas and liquid superficial velocities.

Table F.3 Entrainment fraction data

V_{sl} (m/s)	V_{sg}(m/s)				
	25.8	30.9	35.8	40.6	45.5
0.15	1.73	2.50	3.25	3.69	5.29
0.18	1.77	3.15	2.79	3.79	5.58
0.21	1.97	2.88	3.35	4.45	6.26
0.24	2.76	3.81	3.39	4.63	5.98
0.27	1.99	2.96	3.58	4.40	6.58
0.29	2.11	3.02	3.42	3.81	5.71